

MECHANICS OF MACHINING METAL MATRIX  
COMPOSITES: ANALYTICAL MODELING AND FINITE  
ELEMENT SIMULATION

by

Amirmohammad Ghandehariun

A Thesis Submitted in Partial Fulfillment of

the Requirements for the Degree of

DOCTOR OF PHILOSOPHY

in

The Faculty of Engineering and Applied Science

Mechanical Engineering Program

University of Ontario Institute of Technology

January 2015

© Amirmohammad Ghandehariun, 2015

# Abstract

Metal matrix composites (MMCs) are commonly utilized materials in various industries, including applications in aerospace and automotive industries, due to their outstanding strength-to-weight ratio and wear resistance. The superior mechanical properties of MMCs are achieved through addition of hard ceramics as reinforcements to a metal matrix. However, these reinforcements also have a detrimental effect on the machinability of MMCs. The existence of ceramic reinforcements results in excessive tool wear. Moreover, the complications related to the mechanics of chip formation during MMC cutting further increase the complexity of the cutting process. Thus, in order to overcome the obstacles faced during machining, a comprehensive understanding of MMC cutting process is required.

In this thesis, a detailed understanding of MMC machining is accomplished through numerical and analytical modeling of the process. A finite element model of MMC cutting is developed for analysis of various unique aspects of the process, including the interactions between the cutting tool, the matrix, and the particles. The validity of the proposed model is confirmed by comparison between predicted and measured data. In the FE analysis, all major phases of MMC workpiece, namely the particle phase, the matrix phase, and the matrix-particle interface, are modeled. The developed finite element model provides insight into various

scenarios of interactions between the cutting tool and particles as well as the effect of cutting process parameters on MMC behavior during machining.

Analytical models of MMC machining process are developed for prediction of cutting forces. These models rely on constitutive equations for capturing MMC behavior. Conventional constitutive equations, i.e. constitutive equations developed for modeling traditional monolithic materials, are lacking an explicit description of the effect of MMC's unique features, namely particle size and volume fraction, on MMC behavior. Therefore, a novel constitutive equation is developed for depicting the MMC behavior during machining. This equation considers the fracture and debonding of MMC reinforcements during cutting and clarifies the relation between MMC behavior and particle size and volume fraction. Comparison of analytical model predictions with experimentally measured data verifies that the developed model is capable of providing an accurate depiction of MMC behavior during machining.

# Acknowledgements

The author would like to express his sincere gratitude and appreciation to his research supervisor, Prof. Hossam A. Kishawy, for the continuous support and guidance received throughout this research. The author also expresses his sincere appreciation to the members of the supervisory committee, Dr. Atef Mohany, Prof. Dan Zhang, Dr. Lixuan Lu, and Prof. Marwan Hassan, for their helpful comments and discussions. The author would like to thank his colleagues at the Machining Research Laboratory (MRL).

Last, but not least, I would like to express my heartfelt appreciation to my family. Words cannot express how grateful I am to my parents and my sisters for their love and strong support.

# Table of Contents

<b>ABSTRACT .....</b>	<b>II</b>
<b>ACKNOWLEDGEMENTS.....</b>	<b>IV</b>
<b>TABLE OF CONTENTS .....</b>	<b>V</b>
<b>LIST OF TABLES .....</b>	<b>XI</b>
<b>LIST OF FIGURES .....</b>	<b>XII</b>
<b>NOMENCLATURE .....</b>	<b>XVII</b>
<b>CHAPTER 1 INTRODUCTION .....</b>	<b>1</b>
<b>1.1 PREAMBLE .....</b>	<b>1</b>
<b>1.2 OBJECTIVES .....</b>	<b>6</b>
<b>1.3 SCOPE OF THESIS.....</b>	<b>7</b>
<b>CHAPTER 2 BACKGROUND .....</b>	<b>8</b>
<b>2.1 INTRODUCTION .....</b>	<b>8</b>
<b>2.2 METAL MATRIX COMPOSITES .....</b>	<b>8</b>

<b>2.3</b>	<b>MACHINING OF METAL MATRIX COMPOSITES .....</b>	<b>10</b>
2.3.1	Preamble.....	10
2.3.2	Fiber-reinforced MMCs .....	10
2.3.3	Particle-reinforced MMCs .....	11
<b>2.4</b>	<b>FINITE ELEMENT MODELING OF MACHINING METAL MATRIX COMPOSITES .....</b>	<b>16</b>
2.4.1	Preamble.....	16
2.4.2	FEM for simulation of the machining process.....	16
	<i>a. FEM with Lagrangian formulation.....</i>	<i>17</i>
	<i>b. FEM with Eulerian formulation.....</i>	<i>18</i>
	<i>c. FEM with the Arbitrary Lagrangian Eulerian (ALE) formulation .....</i>	<i>19</i>
2.4.3	FEM in machining fiber-reinforced composites .....	19
2.4.4	FEM in machining particulate reinforced MMCs.....	21
<b>2.5</b>	<b>ANALYTICAL MODELING OF MACHINING METAL MATRIX COMPOSITES .....</b>	<b>23</b>
2.5.1	Preamble.....	23
2.5.2	Machining models .....	24
	<i>a. Merchant's theory of metal cutting.....</i>	<i>24</i>
	<i>b. Oxley's theory of metal cutting.....</i>	<i>26</i>
	<i>c. Energy-based model of metal cutting .....</i>	<i>27</i>
2.5.3	Machining models for MMCs .....	28
	<i>a. Mechanistic modeling.....</i>	<i>28</i>
	<i>b. Energy-based modeling .....</i>	<i>29</i>
2.5.4	Constitutive equations for modeling MMC cutting.....	30
	<i>a. Constitutive models for monolithic material behavior .....</i>	<i>30</i>

<i>b.</i>	<i>Fracture models for reinforcements in MMCs</i> .....	33
<i>c.</i>	<i>Debonding models for reinforcements in MMCs</i> .....	34
<b>2.6</b>	<b>CLOSING REMARKS</b> .....	<b>35</b>
<b>CHAPTER 3</b>	<b>APPROACH AND METHODOLOGY</b> .....	<b>37</b>
<b>3.1</b>	<b>APPROACH</b> .....	<b>37</b>
<b>3.2</b>	<b>METHODOLOGY</b> .....	<b>38</b>
<b>CHAPTER 4</b>	<b>FINITE ELEMENT MODELING OF MACHINING METAL MATRIX COMPOSITES</b> .....	<b>41</b>
<b>4.1</b>	<b>INTRODUCTION</b> .....	<b>41</b>
<b>4.2</b>	<b>PROBLEM DESCRIPTION AND MODELING STEPS</b> .....	<b>42</b>
<b>4.3</b>	<b>MATERIAL MODELING</b> .....	<b>47</b>
4.3.1	Matrix material .....	47
4.3.2	Particle material .....	47
4.3.3	Particle-matrix interface.....	48
<b>4.4</b>	<b>MESHING</b> .....	<b>49</b>
<b>4.5</b>	<b>RESULTS AND DISCUSSION</b> .....	<b>52</b>
4.5.1	Model I, analysis of various scenarios of tool-particle interactions.....	52
<i>a.</i>	<i>Model verification</i> .....	53
<i>b.</i>	<i>Analysis of cutting force during machining</i> .....	54
<i>c.</i>	<i>Tool-particle interaction scenarios</i> .....	55
4.5.2	Model II, analysis of the effect of cutting speed .....	62
<i>a.</i>	<i>Model verification</i> .....	62
<i>b.</i>	<i>Analysis of tool-workpiece interactions</i> .....	63

c.	<i>Analysis of the effect of cutting speed on temperature</i> .....	75
d.	<i>Analysis of the effect of cutting speed on stress</i> .....	77
4.5.3	Model III, analysis of plastic deformation .....	81
<b>4.6</b>	<b>CLOSING REMARKS</b> .....	<b>88</b>
<b>CHAPTER 5</b>	<b>ANALYTICAL MODEL FOR CUTTING FORCE</b> .....	<b>89</b>
<b>5.1</b>	<b>INTRODUCTION</b> .....	<b>89</b>
<b>5.2</b>	<b>MODELING CUTTING FORCE BASED ON PARTITION OF ENERGY</b> .....	<b>90</b>
5.2.1	Energy partition of cutting system .....	90
5.2.2	Power for plastic deformation.....	91
5.2.3	Power for friction at tool-chip interface.....	92
a.	<i>Tool-chip friction force</i> .....	92
b.	<i>Tool-matrix interface</i> .....	92
c.	<i>Tool-particle interface</i> .....	93
5.2.4	Power for friction at tool-workpiece interface.....	96
5.2.5	Power due to effect of minor cutting edge .....	97
5.2.6	Power for debonding of reinforcements .....	97
<b>5.3</b>	<b>EXPERIMENTAL VERIFICATION OF MODEL RESULTS</b> .....	<b>99</b>
<b>5.4</b>	<b>RESULTS AND DISCUSSION</b> .....	<b>100</b>
<b>5.5</b>	<b>CLOSING REMARKS</b> .....	<b>107</b>
<b>CHAPTER 6</b>	<b>NOVEL CONSTITUTIVE MODEL FOR MMC BEHAVIOR DURING MACHINING</b> .....	<b>109</b>
<b>6.1</b>	<b>INTRODUCTION</b> .....	<b>109</b>
<b>6.2</b>	<b>MODELS USED FOR SIMULATION OF MMC BEHAVIOR</b> .....	<b>110</b>

6.2.1	Johnson-Cook equation .....	110
6.2.2	Li and Ramesh equation .....	111
6.2.3	Particle-matrix interface model.....	111
<b>6.3</b>	<b>DEVELOPMENT OF A NOVEL CONSTITUTIVE MODEL .....</b>	<b>113</b>
6.3.1	Flow stress in primary shear zone .....	113
6.3.2	Stress in undamaged part of primary shear zone .....	114
6.3.3	Stress in debonded part of primary shear zone .....	115
6.3.4	Stress in cracked part of primary shear zone .....	116
<b>6.4</b>	<b>CLOSING REMARKS .....</b>	<b>117</b>
<b>CHAPTER 7</b>	<b>CALCULATION OF CUTTING FORCE USING THE DEVELOPED CONSTITUTIVE</b>	
	<b>MODEL .....</b>	<b>118</b>
<b>7.1</b>	<b>INTRODUCTION .....</b>	<b>118</b>
<b>7.2</b>	<b>MODELING CUTTING FORCE BASED ON ENERGY PARTITION .....</b>	<b>119</b>
<b>7.3</b>	<b>IMPLEMENTATION OF THE DEVELOPED CONSTITUTIVE EQUATION .....</b>	<b>120</b>
7.3.1	Power for plastic deformation.....	120
7.3.2	Equivalent plastic strain.....	121
7.3.3	Cutting zone temperature .....	122
7.3.4	Strain rate .....	124
<b>7.4</b>	<b>EXPERIMENTAL VERIFICATION OF MODEL RESULTS .....</b>	<b>124</b>
<b>7.5</b>	<b>RESULTS AND DISCUSSION .....</b>	<b>126</b>
7.5.1	Model verification .....	126
7.5.2	Parametric study.....	133
<b>7.6</b>	<b>CLOSING REMARKS .....</b>	<b>136</b>

<b>CHAPTER 8 CONCLUSIONS AND FUTURE WORK.....</b>	<b>138</b>
<b>8.1 CONCLUSIONS.....</b>	<b>138</b>
<b>8.2 FUTURE WORK .....</b>	<b>143</b>
<b>REFERENCES .....</b>	<b>144</b>

# List of Tables

<b>Table</b>	<b>Page</b>
Table 4.1 Workpiece material parameters.....	42
Table 4.2 Cutting parameters for the analysis .....	43
Table 4.3 Johnson-Cook material properties for Al6061 aluminum matrix [117] .....	47
Table 4.4 Material properties for alumina particles [118] .....	48
Table 4.5 Average node distance in the optimum mesh .....	50
Table 5.1 Increase in power consumption due to the effect of minor cutting edge .....	97
Table 5.2 Properties of the workpiece and tool materials.....	100
Table 5.3 Parameters of the cutting tests.....	100
Table 7.1 Material parameters used in the cutting force model .....	125
Table 7.2 Parameters of the machining experiments .....	125
Table 7.3 Parameters of cutting tests used for obtaining the model constants.....	126
Table 7.4 Constitutive model constants tuned using experimental data .....	126

# List of Figures

<b>Figure</b>	<b>Page</b>
Figure 2.1 Schematic diagram of forces in single shear plane model: (a) Free body diagram of chip; (b) Merchant's cutting force circle [61] .....	25
Figure 4.1 Meshed parts for the finite element analysis of model I (Al 6061/10% 15 $\mu\text{m}$ $\text{Al}_2\text{O}_3$ , rake angle=30°) .....	51
Figure 4.2 Meshed parts for the finite element analysis of model II (Al 6061/20% 23 $\mu\text{m}$ $\text{Al}_2\text{O}_3$ , rake angle=0°).....	51
Figure 4.3 Meshed parts for the finite element analysis of model III (Al 6061/10% 17 $\mu\text{m}$ $\text{Al}_2\text{O}_3$ , rake angle=6°).....	52
Figure 4.4 Comparison of cutting forces obtained using FEM and experimental data [53] (Al 6061/10% 15 $\mu\text{m}$ $\text{Al}_2\text{O}_3$ , $v=85$ m/min, rake angle=30°, width of cut=3 mm) .....	53
Figure 4.5 Cutting forces obtained using finite element analysis (Al 6061/10% 15 $\mu\text{m}$ $\text{Al}_2\text{O}_3$ , $v=85$ m/min, rake angle=30°, width of cut=3 mm) .....	55
Figure 4.6 Different scenarios of tool-particle interactions at three different time steps: (a) particle on the cutting line: fractured and debonded; (b) particle above the cutting line: pushed in the chip; (c) particle below cutting line: fractured and attached .....	56
Figure 4.7 Stress (MPa) distribution during cutting tool engagement which results in particle debonding (Al 6061/10% 15 $\mu\text{m}$ $\text{Al}_2\text{O}_3$ , $v=85$ m/min, rake angle=30°, width of cut=3 mm).....	57
Figure 4.8 Distribution of equivalent plastic strain around the debonded particle (Al 6061/10% 15 $\mu\text{m}$ $\text{Al}_2\text{O}_3$ , $v=85$ m/min, rake angle=30°, width of cut=3 mm).....	57

Figure 4.9 Stress (MPa) distribution during initiation and growth of crack in the particle (Al 6061/10% 15 $\mu\text{m}$ $\text{Al}_2\text{O}_3$ , $v=85$ m/min, rake angle= $30^\circ$ , width of cut=3 mm) .....	58
Figure 4.10 Stress (MPa) distribution during debonding of the particle while being pushed into the chip (Al 6061/10% 15 $\mu\text{m}$ $\text{Al}_2\text{O}_3$ , $v=85$ m/min, rake angle= $30^\circ$ , width of cut=3 mm).....	59
Figure 4.11 Pressure stress (MPa) distribution during debonding of the particle (Al 6061/10% 15 $\mu\text{m}$ $\text{Al}_2\text{O}_3$ , $v=85$ m/min, rake angle= $30^\circ$ , width of cut=3 mm).....	59
Figure 4.12 Stress (MPa) distribution during crack propagation in a particle below the cutting line (Al 6061/10% 15 $\mu\text{m}$ $\text{Al}_2\text{O}_3$ , $v=85$ m/min, rake angle= $30^\circ$ , width of cut=3 mm).....	60
Figure 4.13 Equivalent plastic strain in the matrix material versus distance along the perimeter around the particle for various tool-particle interaction scenarios (Al 6061/10% 15 $\mu\text{m}$ $\text{Al}_2\text{O}_3$ , $v=85$ m/min, rake angle= $30^\circ$ , width of cut=3 mm) .....	61
Figure 4.14 Comparison of cutting forces obtained using FE simulations and experiments (Al 6061/20% 23 $\mu\text{m}$ $\text{Al}_2\text{O}_3$ , rake angle= $0^\circ$ , width of cut=1 mm).....	63
Figure 4.15 Interaction between cutting insert and particle located along the cutting line (Unit: MPa) (Al 6061/20% 23 $\mu\text{m}$ $\text{Al}_2\text{O}_3$ , $v=60$ m/min, rake angle= $0^\circ$ , width of cut=1 mm).....	65
Figure 4.16 Stress (MPa) distribution during interaction in particles located along the cutting line (Al 6061/20% 23 $\mu\text{m}$ $\text{Al}_2\text{O}_3$ , rake angle= $0^\circ$ , width of cut=1 mm).....	66
Figure 4.17 Interaction between cutting insert and particle located below the cutting line (Unit: MPa) (Al 6061/20% 23 $\mu\text{m}$ $\text{Al}_2\text{O}_3$ , $v=60$ m/min, rake angle= $0^\circ$ , width of cut=1 mm).....	68
Figure 4.18 Evolution of crack due to interaction between cutting tool and particle located below the cutting line: initiation of interaction (Unit: MPa) (Al 6061/20% 23 $\mu\text{m}$ $\text{Al}_2\text{O}_3$ , $v=60$ m/min, rake angle= $0^\circ$ , width of cut=1 mm).....	68
Figure 4.19 Evolution of crack due to interaction between cutting tool and particle located below the cutting line: evolution of crack in the particle (Unit: MPa) (Al 6061/20% 23 $\mu\text{m}$ $\text{Al}_2\text{O}_3$ , $v=60$ m/min, rake angle= $0^\circ$ , width of cut=1 mm) .....	69
Figure 4.20 Evolution of crack due to interaction between cutting tool and particle located below the cutting line: complete fracture of particle (Unit: MPa) (Al 6061/20% 23 $\mu\text{m}$ $\text{Al}_2\text{O}_3$ , $v=60$ m/min, rake angle= $0^\circ$ , width of cut=1 mm).....	69

Figure 4.21 Stress (MPa) distribution during interaction in particles located below the cutting line (Al 6061/20% 23 $\mu\text{m}$ $\text{Al}_2\text{O}_3$ , rake angle=0°, width of cut=1 mm) .....	70
Figure 4.22 Interaction between cutting insert and particle located above the cutting line; initiation of crack (Unit: MPa) (Al 6061/20% 23 $\mu\text{m}$ $\text{Al}_2\text{O}_3$ , v=60 m/min, rake angle=0°, width of cut=1 mm) .....	71
Figure 4.23 Interaction between cutting insert and particle located above the cutting line; evolution of crack (Unit: MPa) (Al 6061/20% 23 $\mu\text{m}$ $\text{Al}_2\text{O}_3$ , v=60 m/min, rake angle=0°, width of cut=1 mm) .....	72
Figure 4.24 Interaction between cutting insert and particle located above the cutting line; complete cracking (Unit: MPa) (Al 6061/20% 23 $\mu\text{m}$ $\text{Al}_2\text{O}_3$ , v=60 m/min, rake angle=0°, width of cut=1 mm) .....	72
Figure 4.25 Interaction between cutting insert and particle located above the cutting line; particle pushed into chip (Unit: MPa) (Al 6061/20% 23 $\mu\text{m}$ $\text{Al}_2\text{O}_3$ , v=60 m/min, rake angle=0°, width of cut=1 mm).....	73
Figure 4.26 Stress (MPa) distribution during interaction in particles located above the cutting line (Al 6061/20% 23 $\mu\text{m}$ $\text{Al}_2\text{O}_3$ , rake angle=0°, width of cut=1 mm) .....	74
Figure 4.27 Temperature (°C) distribution during cutting MMC with different cutting speeds (Al 6061/20% 23 $\mu\text{m}$ $\text{Al}_2\text{O}_3$ , rake angle=0°, width of cut=1 mm).....	76
Figure 4.28 Distribution of stress (MPa) in the matrix during cutting MMC with different cutting speeds (Al 6061/20% 23 $\mu\text{m}$ $\text{Al}_2\text{O}_3$ , rake angle=0°, width of cut=1 mm) .....	78
Figure 4.29 Distribution of stress (MPa) in particles during cutting MMC with different cutting speeds (Al 6061/20% 23 $\mu\text{m}$ $\text{Al}_2\text{O}_3$ , rake angle=0°, width of cut=1 mm) .....	80
Figure 4.30 Damage beneath the machined surface along the cutting line for various cutting speeds (Al 6061/20% 23 $\mu\text{m}$ $\text{Al}_2\text{O}_3$ , rake angle=0°, width of cut=1 mm) .....	81
Figure 4.31 Analysis of the effect of using ALE adaptive meshing on mesh quality (Al 6061/10% 17 $\mu\text{m}$ $\text{Al}_2\text{O}_3$ , v=60 m/min, rake angle=6°, width of cut=1 mm).....	82
Figure 4.32 Equivalent plastic strain during MMC cutting (Al 6061/10% 17 $\mu\text{m}$ $\text{Al}_2\text{O}_3$ , v=60 m/min, rake angle=6°, width of cut=1 mm).....	84

Figure 4.33 Equivalent plastic strain during interaction between cutting tool and a particle located on the cutting line (Al 6061/10% 17 $\mu\text{m}$ $\text{Al}_2\text{O}_3$ , $v=60$ m/min, rake angle= $6^\circ$ , width of cut=1 mm) .....	85
Figure 4.34 Equivalent plastic strain during interaction between cutting tool and a particle located above the cutting line (Al 6061/10% 17 $\mu\text{m}$ $\text{Al}_2\text{O}_3$ , $v=60$ m/min, rake angle= $6^\circ$ , width of cut=1 mm).....	86
Figure 4.35 Equivalent plastic strain during interaction between cutting tool and a particle located below the cutting line (Al 6061/10% 17 $\mu\text{m}$ $\text{Al}_2\text{O}_3$ , $v=60$ m/min, rake angle= $6^\circ$ , width of cut=1 mm).....	87
Figure 5.1 Parameters of two-body abrasive contact between the particle and cutting tool.....	95
Figure 5.2 Flowchart for calculation of cutting force .....	99
Figure 5.3 Comparison of cutting force from experiments and developed model at various feed rates for machining MMCs ( $v=60$ m/min, rake angle= $6^\circ$ ).....	102
Figure 5.4 Comparison of cutting force from experiments and developed model at various feed rates for machining MMCs ( $v=60$ m/min, rake angle= $6^\circ$ ).....	103
Figure 5.5 Partition of power consumption in the MMC machining system for various feed rates (Al 6061/10% 17 $\mu\text{m}$ $\text{Al}_2\text{O}_3$ , $v=60$ m/min, rake angle= $6^\circ$ ).....	104
Figure 5.6 Comparison of cutting force from experiments and predictions by proposed model at various cutting speeds for machining Al 6061/20% 23 $\mu\text{m}$ $\text{Al}_2\text{O}_3$ (feed rate=0.1 mm/rev, rake angle= $0^\circ$ ).....	105
Figure 5.7 Partition of power consumption in the MMC machining system for various cutting speeds (Al 6061/20% 23 $\mu\text{m}$ $\text{Al}_2\text{O}_3$ , feed rate=0.1 mm/rev) .....	106
Figure 5.8 Comparison of cutting force from experiments and predictions by proposed model for machining Al 6061/20% $\text{Al}_2\text{O}_3$ with various particle diameters ( $v=30$ m/min, feed rate=0.1 mm/rev) .....	107
Figure 6.1 Schematic describing different deformation patterns in the primary shear zone during MMC cutting .....	114
Figure 7.1 Comparison of cutting force from experiments and developed model at various feed rates for machining MMCs ( $v=60$ m/min, rake angle= $6^\circ$ ).....	127
Figure 7.2 Comparison of cutting force from experiments and developed model at various feed rates for machining MMCs ( $v=60$ m/min, rake angle= $6^\circ$ ).....	128

Figure 7.3 Different terms of power for plastic deformation for various feed rates (Al 6061/10% 17 $\mu\text{m}$ $\text{Al}_2\text{O}_3$ , $v=60$ m/min, rake angle= $6^\circ$ ) .....	130
Figure 7.4 Power required for deformation during cutting with various feed rates (Al 6061/10% 17 $\mu\text{m}$ $\text{Al}_2\text{O}_3$ , $v=60$ m/min, rake angle= $6^\circ$ ) .....	131
Figure 7.5 Comparison of cutting force from experiments and proposed model at various cutting speeds for machining Al 6061/20% 23 $\mu\text{m}$ $\text{Al}_2\text{O}_3$ (feed=0.1 mm/rev, rake angle= $0^\circ$ ) .....	132
Figure 7.6 Comparison of cutting force from experiments and proposed model for machining Al 6061/20% $\text{Al}_2\text{O}_3$ with various particle diameters ( $v=30$ m/min, feed=0.1 mm/rev, rake angle= $0^\circ$ ) .....	133
Figure 7.7 Variation of cutting force versus particle diameter during MMC machining (Al 6061/10% $\text{Al}_2\text{O}_3$ MMC, $v=30$ m/min, feed=0.1 mm/rev, rake angle= $0^\circ$ ) .....	134
Figure 7.8 Variation of cutting force versus cutting speed during MMC machining (Al 6061/10% 20 $\mu\text{m}$ $\text{Al}_2\text{O}_3$ MMC, feed=0.1 mm/rev, rake angle= $0^\circ$ ) .....	135
Figure 7.9 Variation of cutting force versus reinforcement volume fraction during MMC machining (Al 6061/20 $\mu\text{m}$ $\text{Al}_2\text{O}_3$ MMC, $v=30$ m/min, feed=0.1 mm/rev, rake angle= $0^\circ$ ) .....	136

# Nomenclature

$A$	Johnson-Cook plasticity constant [MPa]
$A_c$	Uncut chip cross-sectional area [m <sup>2</sup> ]
$A_i$	Contact area at the particle-tool interface [m <sup>2</sup> ]
$b$	Width of cut [m]
$b_{1T}$	True chip width [m]
$B$	Johnson-Cook plasticity constant [MPa]
$Br$	Briks similarity criterion
$c$	Workpiece material specific heat [J.kg <sup>-1</sup> .°C <sup>-1</sup> ]
$C$	Johnson-Cook plasticity constant
$d$	Particle diameter [m]
$d_N$	Weibull probability normalizing constant [m]
$D$	Damage parameter
$D_1 \dots D_5$	Johnson-Cook damage constant
$e$	Specific cutting energy [J/m <sup>3</sup> ]

$E$	Modulus of elasticity [Pa]
$E_D$	Specific energy for particle debonding [ $\text{J}/\text{m}^3$ ]
$E_p$	Specific energy for plastic deformation in primary shear zone [ $\text{J}/\text{m}^3$ ]
$E_s$	Specific energy for plastic deformation in secondary shear zone [ $\text{J}/\text{m}^3$ ]
$f$	Feed rate [m/rev]
$F$	Friction force [N]
$F_C$	Cutting force [N]
$F_f$	MMC cutting friction force [N]
$F_{f-2\text{body}}$	Two-body abrasion friction [N]
$F_{f-3\text{body}}$	Three-body rolling friction [N]
$F_{fM}$	Friction at the tool-matrix interface [N]
$F_{fP}$	Friction at the tool-particle interface [N]
$F_s$	Shear force [N]
$F_T$	Thrust force [N]
$h$	Uncut chip thickness [m]
$H_1, H_2, H_3$	Constitutive equation empirical constants
$H_{\text{tool}}$	Tool material Vickers hardness
$k$	Workpiece material thermal conductivity [ $\text{W}\cdot\text{m}^{-1}\cdot\text{C}^{-1}$ ]
$l$	Shear length [m]
$l_c$	Tool-chip contact length [m]
$m$	Johnson-Cook plasticity constant
$n$	Johnson-Cook plasticity constant

$N$	Normal force [N]
$N_p$	Number of particles at the tool-chip interface
$P_c$	Total cutting power consumption [W]
$P_{deb}$	Power required for debonding of particles [W]
$P_{fns}$	Power required for formation of new surfaces [W]
$P_{fr}$	Probability of fracture of reinforcement
$P_{mnc}$	Power consumption due to effect of minor cutting edge [W]
$P_{pd}$	Power for plastic deformation [W]
$P_{tc}$	Power spent at tool-chip interface [W]
$P_{tw}$	Power spent at tool-workpiece interface [W]
$q$	Weibull inhomogeneity factor
$R$	MMC particle radius [m]
$R_T$	Dimensionless thermal number
$t_{1T}$	True uncut chip thickness [m]
$t_{2body}$	Fraction of particles involved in two-body abrasion
$t_n$	Normal traction [Pa]
$t_n^o$	Maximum normal traction [Pa]
$t_s$	First direction shear traction [Pa]
$t_s^o$	Maximum first direction shear traction [Pa]
$t_t$	Second direction shear traction [Pa]
$t_t^o$	Maximum second direction shear traction [Pa]
$T$	Material temperature [°C]

$T_{\text{melt}}$	Material melting temperature [°C]
$T_n$	Normal traction at matrix-particle interface [Pa]
$T_s$	Temperature in the primary shear zone [°C]
$T_{\text{transition}}$	Transition temperature [°C]
$T_w$	Initial workpiece temperature [°C]
$v$	Cutting speed [m/s]
$v_s$	Shear velocity [m/s]
$V_f$	MMC volume fraction

## Greek letters

$\alpha$	Flank angle [deg]
$\gamma$	Rake angle [deg]
$\Gamma$	Energy required for debonding of one particle [J]
$\delta_n$	Separation at matrix-particle interface [m]
$\delta_n^c$	Characteristic length of matrix-particle interface [m]
$\delta_{p0}$	Tool-particle groove depth [m]
$\epsilon$	Equivalent plastic strain
$\epsilon^f$	Equivalent strain to fracture
$\dot{\epsilon}$	Plastic strain rate [1/s]
$\dot{\epsilon}_0$	Reference strain rate [1/s]
$\zeta$	Chip compression ratio

$\eta$	Factor of plastic work occurring in primary shear zone
$\theta_p$	Tool-particle angle of contact [deg]
$\kappa_{r1}$	Minor cutting edge angle [deg]
$\lambda$	Matrix-particle interface equation non-dimensional parameter
$\mu$	Friction angle [deg]
$\mu_{3body}$	Three-body friction coefficient
$\nu$	Poisson's ratio
$\nu'$	Effective Poisson's ratio
$\rho$	Workpiece material density [kg/m <sup>3</sup> ]
$\rho_{ce}$	Cutting edge radius [m]
$\sigma$	Flow stress [Pa]
$\sigma_0$	Weibull probability normalizing constant [Pa]
$\sigma_{cracked}$	Stress in cracked part of primary shear zone [Pa]
$\sigma_{debonded}$	Stress in debonded part of primary shear zone [Pa]
$\sigma_{max,int}$	Matrix-particle interface strength [Pa]
$\sigma_P$	Particle stress [Pa]
$\sigma_R$	Ultimate tensile strength of matrix material [Pa]
$\sigma_{undamaged}$	Stress in undamaged part of primary shear zone [Pa]
$\sigma^*$	Stress triaxiality
$\tau_c$	Average shear stress at the tool-chip contact [Pa]
$\tau_f$	Shear flow stress [Pa]
$\tau_{fric}$	Frictional shear stress [Pa]

$\tau_y$	Shear strength of the matrix material [Pa]
$\phi$	Shear angle [deg]
$\phi_{sep}$	Work of separation at matrix-particle interface [J]
$\Phi$	Interface failure energy [J/m <sup>2</sup> ]

# Chapter 1 Introduction

## 1.1 Preamble

A composite material is defined as a combination of two or more materials with different chemical and mechanical properties that are not soluble in one another. The matrix phase transfers load and supports the integrity of the structure while the particle phase provides the enhanced mechanical properties of the composite. Excellent mechanical and thermal properties enable composites to be utilized in a wide range of applications, such as automotive, aerospace, oil and gas, etc. Characteristics such as a high strength-to-weight ratio, high modulus-to-weight ratio, good damage tolerance, acceptable fatigue life, and corrosion resistance are highly anticipated in these applications and many of them can be uniquely achieved through utilization of composites.

Among composites, metal matrix composites are the widely used material in many industrial applications for their outstanding strength and wear resistance. Some examples of MMC applications are in cylinder liners for internal combustion engines, ventral fins

and lower drag brace landing gears in fighter planes, and helicopter blades [1]. The excellent wear resistance in MMC materials is mainly achieved through addition of the reinforcements in the form of abrasive ceramics to a metal matrix. Although composite materials are usually manufactured to near net shape, machining processes are commonly employed to achieve the desired dimensional accuracy of the final product.

As the most popular material removal process, machining is believed to be one of the main sources of industrial revolution and growth of manufacturing-based economies [2]. It is a process that involves cutting metals using various cutting tools. It is used in various industrial applications due to its accuracy, flexibility, and cost efficiency for production of limited quantities of products. Popularity of the machining process highlights the importance of understanding the mechanics of metal cutting. Development of modern machine tools and optimization of machining techniques requires systematic knowledge of mechanics of chip formation. This knowledge is also necessary for manufacture of products from new generation of engineering materials, which are commonly more difficult to cut due to their enhanced mechanical properties.

Machining metal matrix composites is a challenging task in comparison to machining the traditionally used metals in industry. This is mainly due to the existence of hard ceramic reinforcements in MMCs which have similar hardness characteristics as the cutting tools. During machining, these hard ceramic particles are rubbed against the cutting tool and severely damage the tool surface, leading to excessive tool wear. Excessive tool wear, in turn, causes various types of damage, such as particle fracture and

debonding at the interface between particle and matrix. Moreover, the complications related to the mechanics of chip formation during MMC cutting further increase the complexity of the cutting process. These obstacles arise from the interactions between cutting tool, matrix, and reinforcements. Thus, machining MMCs is considered to be a challenging process. The main difficulties are seen in obtaining an optimal combination of process parameters in order to achieve the desired tool life, surface finish, and metal removal rate. It is clear that a comprehensive and general understanding of the MMC behavior during the machining operation is considered an asset in achieving these optimal parameters.

Various methods are available for studying the machining process of metal matrix composites. The diverse investigation methodologies can be divided into three main categories: experimental analysis, mechanistic modeling, and numerical modeling and simulation. Experimental or empirical modeling generally focuses on understanding the macro/microscopic machinability of MMCs and the surface integrity of the machined product. Mechanistic modeling tries to describe the composite material behavior using basic cutting mechanics. Numerical simulations approach the problem at two levels: The macroscopic models simulate the cutting process while treating the material as a macroscopically anisotropic material; the microscopic models focus on the interaction between particles and matrix. Macroscopic models often disregard many fundamental characteristics of the composite material and cannot determine the details of material behavior. Microscopic models usually provide more details of the actual behavior of the matrix and particle during the cutting process and offer a better simulation of the

interaction between tool and composite material. However, simulation of a microscopic model during machining is generally very time-consuming.

Many challenges still exist in understanding the mechanics of machining. The new improvements in computer technologies have empowered researchers to gain a better understanding of the cutting process through complex numerical simulations. Finite element modeling is a major numerical technique utilized by many researchers in this field. This modeling technique is currently being used to achieve broader knowledge regarding various aspects of the cutting process, such as chip formation and separation, subsurface damage, and tool-chip interactions [3].

An essential part of any finite element model is a description of material's constitutive behavior. During machining, workpiece material usually undergoes extreme deformations which are associated with high strain, strain rate, and temperature. Material constitutive equations provide a stress-strain relation that depends on strain-hardening, strain rate, and temperature. Moreover, chip separation criteria, required by Lagrangian or Arbitrary Lagrangian-Eulerian (ALE) analysis, commonly involve prediction of material damage evolution and fracture. A correct fracture prediction is possible only if material damage behavior is well understood. Therefore, damage equations for the workpiece material are required in order to describe the initiation and evolution of damage during machining.

Knowledge regarding the constitutive behavior of the material during cutting is required for understanding any type of machining process. Constitutive equations are

excellent tools for studying the relations between various aspects of the cutting process, such as cutting force and microstructure damage, and workpiece material characteristics. These equations are particularly important for modeling MMC cutting, where alterations in features such as reinforcement size and volume fraction can immensely affect the MMC behavior during machining process.

Although machining MMCs has been extensively studied through experimental research [1, 4-9], very few analytical models for analysis of the process exist. Among these analytical models, the energy-based model [10] and the mechanistic models [11, 12] are more commonly employed by researchers. Although these models have been relatively successful in defining the effects of some unique features of MMCs, such as volume fraction and size of reinforcements, on different process outputs, they all rely on constitutive equations that are usually utilized for modeling traditional materials. Thus, these constitutive equations are lacking an explicit relationship between the process parameters and the unique MMC features. Instead, the effect of MMC features is implicitly embedded in the model constants. A comprehensive understanding of MMC cutting behavior can only be achieved using constitutive models that are able to explicitly describe the relationship between the MMC behavior and its unique features, namely particle size and volume fraction.

## 1.2 Objectives

This research aims at providing a comprehensive understanding of machining metal matrix composites. This understanding will be achieved by means of numerical and analytical modeling of the process.

The numerical model will be in the form of finite element analysis of cutting. This model simulates the behavior of the matrix, the particles, and the matrix-particle interface during machining. In order to obtain the finest results from the finite element analysis, an attempt will be made to use constitutive models that would best describe the metal matrix composite material response during the cutting process. The results of the finite element simulations will be validated through comparison with experimental data. The finite element model will provide invaluable information regarding the interactions between the cutting tool and different phases of the MMC. It will also help understand the effects of machining on the MMC microstructure.

The analytical model will be based on a semi-empirical equation for predicting the constitutive behavior of MMC during machining. This equation will describe the relationship between flow stress, strain, strain rate, and temperature in the MMC. It will also incorporate the unique composite characteristics, namely volume fraction and size of reinforcements. This model will consider scenarios of fracture and debonding of MMC reinforcements as a result of cutting.

### **1.3 Scope of thesis**

Chapter 2 presents a discussion of the background topics and a review of literature relevant to this thesis. In chapter 3, the approach towards achieving the objectives of this research along with the employed methodologies are provided. Details of the finite element modeling of MMC machining process are explained in chapter 4. The proposed finite element model is utilized for analysis of various unique aspects of MMC cutting, including interactions between cutting tool and reinforcements, the effect of cutting speed on MMC cutting process, and plastic deformations during MMC machining. Finite element model results are presented and validated against experimental data. An analytical model for prediction of cutting forces during MMC machining, which relies on conventional constitutive equations, is presented in chapter 5. In chapter 6, a novel constitutive equation for modeling MMC behavior during the cutting process is developed. This constitutive equation is then used in development of a new analytical cutting force model, as explained in chapter 7. Model predictions for machining different MMCs under various cutting conditions are presented and compared with experimental values. In chapter 8, the findings of this thesis are concluded and areas of future work in this field are described.

# Chapter 2 Background

## 2.1 Introduction

This chapter provides a brief description of the published literature related to modeling machining metal matrix composites, which will help establish the proper context in relation to the previous research works. The most significant publications in the field of numerical and analytical modeling of cutting process of MMCs will be presented and the achievements of researchers in the relevant topics will be reviewed.

## 2.2 Metal Matrix Composites

Similar to all composites, metal matrix composites (MMCs) are a combination of at least two physically and chemically distinct phases; these phases are randomly distributed in order to achieve properties that are not achievable by either of the phases individually. Commonly, an MMC consists of two phases i.e. a reinforcement phase in metal matrix. The reinforcement phase is in the form of one of the following categories:

1. Particulates,
2. Short fibers (whiskers), and

### 3. Long fibers.

Examples of these reinforcing phases include alumina fibers as reinforcements in aluminum matrix composites used in power transmission lines; niobium-titanium filaments in a copper matrix for superconductors; tungsten carbide particles as reinforcements in composites used as cutting tools; and silicon carbide particles in aluminum matrix composites used in aerospace and automotive applications [13]. Applications in the automotive industry include cylinder liners for internal combustion engines and discs, drums, and calipers for the brake system. In the aerospace industry, these composites are used for manufacture of ventral fins and lower drag brace landing gears for fighter planes and helicopter blades [1].

Metal matrix composites offer several advantages over monolithic metals and other composites. Compared to metals, MMCs are advantageous in the following fields [13]:

- Weight saving due to their higher strength-to-weight ratio
- Dimensional stability, as compared to, for example, monolithic aluminum
- Better behavior at high temperature, i.e. creep resistance
- Major improvement in fatigue behavior

With respect to polymer matrix composites (PMCs), MMCs offer the following advantages [13]:

- Higher strength and stiffness
- Broader working temperature range

- Higher thermal and electrical conductivity
- Better options for joining
- Improved behavior under radiation exposure

## 2.3 Machining of metal matrix composites

**2.3.1 Preamble:** MMCs are usually categorized into two groups according to the type of reinforcements: Fiber-reinforced MMCs and particle-reinforced MMCs. Due to the very different nature of the behavior of these composite groups during machining, this background review will be provided in separate sections.

**2.3.2 Fiber-reinforced MMCs:** Fiber-reinforced metal matrix composites are not perfect candidates for machining using conventional machining methods. This is because of the hardness of ceramic reinforcement fibers. Furthermore, fiber breakage or pullout as a result of machining can result in deterioration of material properties. Oxidation of some fiber materials is also a problem that should be addressed during machining [3].

Varadarajan et al. [14] performed conventional machining tests on an aluminum fiber-reinforced MMC with 25% volume fraction of aluminosilicate fibers. They compared the performance of multicoated carbide tools with polycrystalline cubic boron nitride (PCBN) tools in machining MMCs. They found that, although carbide tools are reasonable options in machining these composites, PCBN tools outperform carbide tools in terms of

tool life. This is mainly a result of extreme tool wear caused by abrasion in multicoated carbide tools.

Weinert and Lange [15] carried out various conventional machining tests on magnesium alloy MMC with 20% volume fraction of short alumina and carbon fibers. As a result of their milling, drilling, reaming, and threading tests, they found that the excessive tool wear during machining, and consequently machining with worn cutting tool can cause subsurface damage and fractured reinforcements, which can lead to weakening of material properties. Hence, they suggested using moderate cutting speeds and high feed to make up for the high tool wear.

Dandekar and Shin [16] conducted laser-assisted machining experiments on Al-2% Cu aluminum matrix composite reinforced with 62% by volume fraction alumina fibers. Their experimental results showed that the main type of machining-induced damage in the composite is fiber breakage below the cutting plane. Hence, by using laser-assisted machining and increasing the metal removal temperature, they managed to reduce cutting energy, surface roughness, tool wear, and fiber pullout.

**2.3.3 Particle-reinforced MMCs:** Many researchers have performed experimental studies of machining particulate reinforced metal matrix composites. These studies were aimed at achieving a broader understanding of tool wear, surface roughness, and subsurface damage during the machining process. These parameters were found to be dependent on different composite characteristics, such as the reinforcement material,

volume fraction and size of the reinforcement, matrix properties, and the distribution of reinforcement particles in the matrix.

One of the early investigations of machinability of particulate metal matrix composites was performed by Tomac et al. [4]. They did machining tests on an aluminum matrix composite reinforced with 14 vol.% SiC particles. Their experimental results proved that due to existence of hard particles in the MMC, extreme flank wear of the cutting tool occurs during machining. Hence, they recommended using polycrystalline diamond (PCD) tools in order to reduce wear and improve the surface finish. They also suggest employing high feed rates and low cutting speeds in order to improve material removal rate and surface finish.

Quigley et al. [5] analyzed the influence of cutting tool coatings on cutting tool wear and surface finish when machining metal matrix composites. They found that triple-coated carbide tools with a top layer of TiN are the best option among carbide tools for machining of MMC, even though flank wear is excessive in these tools, regardless of the coatings. It was also concluded in their research that the cutting mechanism in MMC tends to be in the form of crumbling, similar to concrete/aggregate mixture, rather than shearing, as can be seen in ductile materials.

Lin et al. [6] examined the machinability of A359 aluminum matrix composite with 20 vol.% SiC reinforcement. They studied the performance of PCD cutting tools in terms of wear and tried to obtain a modified form of the Taylor equation for predicting the tool

life. They found abrasion occurring between reinforcement particles and cutting tool material to be the main form of tool wear mechanism.

A comprehensive research regarding machining of particulate metal matrix composites was performed by El-Gallab and Sklad and their findings were published in a series of four papers [7, 8, 17, 18]. They performed high-speed turning tests on 20% SiC/Aluminum MMCs. They analyzed the performance of different cutting tool materials. Their results indicated abrasion and micro-cutting of tool material grains as the main wear mechanism in cutting MMC materials. Moreover, they studied the integrity of the workpiece surface in machining the above-mentioned MMCs. Their experimental results demonstrated that plastic deformation can be seen up to as far as 60 – 100  $\mu\text{m}$  beneath the machined surface. Measurements also showed higher microhardness in this sub-surface layer which is considered to be a result of dislocation pile-up and formation of finer grains.

Studies on tool wear mechanisms in machining particle-reinforced metal matrix composites are presented by Yanming and Zehua [19] and Andrewes et al. [20]. They found the major factors affecting the life of the cutting tools in machining MMCs to be the volume fraction and size of the reinforcement particles. The more volume fraction or coarser size of SiC particles is found to result in more severe wear of the tool and shorter tool life. Built-up edge is also seen in machining MMCs at low speeds which can protect the rake face of the tool; however this built-up edge cannot protect the flank face against abrasion.

Another analysis of the performance of PCD tools in cutting metal matrix composites was performed by Davim [21]. His analysis confirmed the earlier understanding that PCD cutting inserts are the perfect choice for machining MMCs. In this work, an equation is also presented to predict the life of the PCD cutting tool according to parameters such as cutting speed and feed.

In his other work, Davim [22] presented an investigation of the effective cutting characteristics in machining MMC including parameters such as tool wear, machining power, and surface roughness. In this study, orthogonal arrays and the analysis of variance (ANOVA) were employed in order to understand the significance of variations in each of the cutting characteristics such as cutting velocity, feed rate, and the cutting time on the final results.

Ding et al. [23] compared the performance of PCBN tools and PCD tools in machining Al-SiC metal matrix composites. They found that PCD cutting inserts provide better performance during the machining process which is a result of their higher resistance against abrasion and fracture and lower tendency to adhere to the working material.

Machinability of particle-reinforced metal matrix composites was studied by Muthukrishnan et al. [24]. They analyzed the specific power consumption as an indicator of machinability and they found it to be lower when machining MMCs at higher cutting speeds. Furthermore, higher cutting speeds result in easier particle debonding and consequently, improved quality of the machined surface.

An early model for predicting cutting forces during machining metal matrix composites was presented by Kishawy et al. [10]. In this research, an analytical force model for orthogonal cutting was provided based on the total energy required for the cutting process. The calculated energy included the energy required for deformation as well as the energy consumed in debonding of the matrix-reinforcement interface.

Kannan et al. [25] developed a model for prediction of wear on the tool flank surface during orthogonal machining of MMCs. This analytical model succeeded in predicting the progress of flank wear during orthogonal cutting as a function of cutting parameters and tool and workpiece properties.

Kishawy et al. [26] presented a model for predicting tool wear during bar turning of MMC materials. Their model considered the effects of two-body abrasion and three-body abrasion on the cutting tool in order to calculate the flank wear during oblique cutting. Their model along with their experimental results agreed well with previous understandings regarding the mechanisms of wear during machining metal matrix composites [27].

An analysis of the characteristics of machined surface of MMCs was performed by Kannan and Kishawy [9]. Their research investigated the variations of microhardness beneath the machined surface and provided an understanding of the effects of machining parameters and MMC properties on the quality of the surface. They found that parameters such as particle volume fraction, particle average size, and initial hardness of the matrix material greatly affect the extent of plastic deformations and damage beneath

the surface. They also showed that application of coolant during machining metal matrix composites affects surface characteristics such as subsurface microhardness and surface roughness. These conclusions together with other tribological aspects of machining MMC materials were later detailed in [1].

## **2.4 Finite element modeling of machining metal matrix composites**

**2.4.1 Preamble:** Two main approaches towards understanding the machining process are popular among researchers [28]; the direct experimental approach and the numerical simulation approach. The experimental approach is usually very time consuming and expensive, particularly in cases where many parameters, such as tool geometry, material properties, and cutting conditions, can affect the process. The numerical approach is usually preferred for its ability to provide a more comprehensive knowledge regarding the machining process.

**2.4.2 FEM for simulation of the machining process:** Finite element methods are among the most common methods of analysis in numerical simulation. These methods facilitate investigation of the machining process with all its complexities in terms of material metallurgy, material elastic and plastic behavior, heat transfer, fracture mechanics, and the effect of using coolants. Finite element analysis is able to provide a prediction of deformations, stress, strain, temperature, and cutting forces during a specific cutting process. A bibliography of the literature related to simulation of the

machining process using finite element methods from 1976 to 2002 is compiled by Mackerle [28, 29].

An early model for finite element simulation of orthogonal cutting process was developed by Iwata et al. [30]. This model used rigid-plastic material models without considering temperature effects. Temperature dependence was first incorporated in machining FEM by Tay et al. [31] and Stevenson et al. [32]. Lajczok [33] proposed utilization of plane strain analysis for FE simulation of cutting. More recent research regarding FEM for machining has focused on various specific situations occurred during cutting. For instance, Ceretti et al. [34] studied segmental chip formation using FEM while Marusich and Ortiz [35] used adaptive remeshing techniques for simulation of transition from continuous to segmented chip during high speed machining.

Finite element models, which are basically discretized models of a continuum, can be based on various descriptions of material kinematic behavior. These descriptions define the relationship between the finite element mesh and the underlying deformed continuum. Therefore, similar to continuum mechanics, finite element simulations can be based on Lagrangian or Eulerian formulations of material behavior. These formulations will be described in this section.

a. *FEM with Lagrangian formulation*: In FE simulations with Lagrangian formulation, the mesh is attached to the underlying material. Nodes on the finite element mesh follow the underlying material points and the geometry of elements is updated with deformations in the material during the simulation. The ability of models with this formulation to follow

the workpiece material enables them to simulate the separation and formation of chip during the initial stages of cutting. However, following the continuum material points can also result in severe mesh distortion. Early research on employing FE models with Lagrangian formulation for simulation of cutting is performed by Carroll and Strenkowski [36] and Strenkowski and Moon [37]. An important aspect of using these models for simulation of machining is the need for material fracture models; separation and formation of chip during cutting requires models for prediction of fracture in the material during simulation using Lagrangian formulation. This aspect results in a more realistic chip formation; however modeling fracture in Lagrangian formulation requires removal of elements from the model, which can decrease the accuracy of results due to reduction in the material mass.

b. *FEM with Eulerian formulation*: In FE simulations with Eulerian formulation, the finite element mesh is fixed in space while the underlying material flows inside the mesh. In this formulation, the variables of the conservation equations are significant for an instant in a specific position in space. Thus, each variable is expressed for a position on the fixed mesh, which is unrelated to the material's previous configuration or coordinates.

Employing Eulerian formulation in metal cutting has the advantage of avoiding mesh distortion as the mesh is fixed in space. Chip separation criteria are also not needed in FE models with this formulation. However, these models usually cannot simulate initiation of chip formation and require prior determination of chip shape. An early FE

model using Eulerian formulation for metal cutting is developed by Strenkowski and Carroll [38].

c. *FEM with the Arbitrary Lagrangian Eulerian (ALE) formulation*: Lagrangian and Eulerian formulations both offer advantages in simulation of cutting using FEM. The ALE technique was developed in order to benefit from these advantages while overcoming the shortcomings of each of the formulations [39-43]. In this technique, some finite element mesh nodes are attached to the underlying material and follow the continuum while others are fixed in space. As a results, this method reduces the distortion in the mesh as compared to Lagrangian FEM while providing a simulation of chip formation that is more realistic than that of Eulerian technique.

**2.4.3 FEM in machining fiber-reinforced composites**: An early finite element analysis of machining fiber-reinforced composites was performed by Arola et al. [44]. Their model simulated the chip formation during edge trimming of unidirectional fiber-reinforced plastics (FRPs). They simulated the process for composites with a fiber orientation range of  $0^\circ - 90^\circ$ . In order to validate their model, they provided a comparison between the cutting forces during machining tests and the forces obtained using the finite element model. They also analyzed the effect of tool geometry on the cutting forces, sub-surface damage, and stress on the tool tip.

Nayak et al. [45] investigated the composite damage associated with machining FRPs through micromechanical finite element analysis. Their work provided a prediction

of the sub-surface damage and fiber-matrix debonding. Their analysis of debonding involved cohesive zone modeling (CZM) of the interface between the fibers and the matrix. Using the Abaqus commercial FEM software and energy-based traction-separation law in cohesive elements, they managed to properly simulate the interfacial debonding and fiber failure during machining FRPs.

Nayak and Bhatnagar [46] and Nayak et al. [47] later published their research on machining unidirectional glass fiber-reinforced plastics (UD-GFRP). In these papers, they provided an experimental analysis of the effect of various geometrical and process parameters on machining characteristics such as the shape of the chip, fiber failure and debonding, cutting forces, and sub-surface damage. Later in the second part of their publication, they presented a finite element analysis to simulate the process in agreement with the experimental data. Their FEM initially involved an equivalent homogenous material (EHM) modeling of the workpiece; however, this model could not predict the cutting forces in good agreement with experimental data. Hence, a micro-mechanical model consisting of separate phases of matrix and fiber was proposed. This model managed to provide an understanding of the chip formation process and sub-surface damage during machining UD-GFRPs.

A more recent finite element analysis of machining UD-GFRP composites was performed by Rao et al. [48]. This research work involved a dynamic explicit FEM of the process, considering separate phases for the elastic-plastic matrix, elastic fibers, and the cohesive zone interface between the matrix and the fibers. Using this model, they

provided an understanding of possible forms of failure in the fibers and the matrix and debonding in the fiber-matrix interface. They also presented predictions for chip size during machining these composites.

Lately, more comprehensive FE investigations of machining fiber-reinforced plastics are provided by Dandekar and Shin [49] and Mkaddem et al. [50]; the former employs a micro-mechanical approach by considering three separate phases for the matrix, fibers, and in the matrix-fiber interface, while the latter uses a single phase Equivalent Orthotropic Homogenous Modeling (EOHM) to simulate the behaviour of the workpiece material. Validation of these models with experimental data shows good agreement in terms of the cutting forces. Therefore, these models are able to provide an acceptable prediction of the machining process characteristics for fiber-reinforced composite materials.

**2.4.4 FEM in machining particulate reinforced MMCs:** An early attempt at finite element modeling of machining particle-reinforced metal matrix composites was made by Monaghan and Brazil [51, 52]. In their work, they provided a two-stage simulation for the process; in the first stage, the single-phase global machining model is employed to simulate the cutting process in steady state conditions, while in the second stage, the loading history recorded in the previous stage is applied to a micro-mechanical model of a square section of the MMC material. Using this modeling technique, they managed to

simulate particle debonding associated with machining MMCs along with the contact stresses on the tool surface during the cutting process.

Zhu and Kishawy [53] provided a thermo-mechanical finite element model for the MMC cutting process. Their simulation involved a thermo-elastic-plastic plain strain model for the workpiece along with elastic particles and a particle-matrix interface with the same hardness as the particles. The incorporation of temperature in the simulation facilitates a more comprehensive modeling of the plastic behavior of the material. Their finite element model managed to predict the cutting forces as well as the stress and temperature distribution in the workpiece material.

One of the most effective concepts in machining performance of MMC is the interaction between tool and particles. Pramanik et al. [54] provided a comprehensive investigation of the tool-particle interactions during MMC orthogonal cutting. In this research work, they employed finite element analysis to gain an understanding of the behavior of the workpiece material during the cutting process in three scenarios: reinforcement particles above the cutting path, reinforcement particles along the cutting path, and reinforcement particles below the cutting path. They concluded that the main reasons for particle fracture and interfacial debonding during machining MMC are the tool-particle interactions and the distribution of stress in the material.

A more recent finite element investigation of the MMC cutting process was conducted by Zhou et al. [55]. This research work provided a two-dimensional thermo-mechanical model of orthogonal cutting which is used to analyze the removal mechanism

of the particle from the matrix. This analysis provided an understanding of the relation between von Mises equivalent stress distribution in the particle and matrix, and the removal mechanism of the particle. Hence, the removal mechanism of the particle based on the location of the cutting tool with respect to the particle can be investigated.

Lately, with the improvements in computation technologies and FEM software, researchers have been able to conduct more comprehensive finite element analyses of machining of metal matrix composites. One of these investigations is performed by Dandekar and Shin [56]. In their work, they provided a multi-step 3D model for prediction of sub-surface damage during the MMC machining process. They initially simulated the process using a single-phase Equivalent Homogenous Material (EHM) model to obtain the stress and temperature distribution in the workpiece material. Then in the next step, they applied the obtained data to a local multi-phase model consisting of a thermo-elastic-plastic matrix, linearly-elastic particles, and particle-matrix interface modeled using cohesive zone elements. This model managed to provide a better prediction of debonding and particle fracture as well as the depth of damage in the MMC material during the cutting process.

## **2.5 Analytical modeling of machining metal matrix composites**

**2.5.1 *Preamble*:** Understanding any type of machining process requires knowledge regarding the relations between process parameters, such as cutting speed and feed rate, workpiece material properties, such as material's elastic and plastic parameters, and

characteristics of the cutting process, such as cutting force and microstructure damage. Analytical machining models are primary candidates for obtaining this information. In the case of machining MMCs, a more comprehensive understanding can be achieved by means of analytical models that describe the relationship between the composite's unique features, namely volume fraction and size of reinforcements, and the outcome of cutting process. In this section, some of the models for describing the cutting process, in general, and MMC cutting, in particular, will be reviewed.

**2.5.2 Machining models:** Various models for analytical investigation of machining process have been proposed by researchers. A classification of these models categorizes them into mechanistic models and energy-based models.

a. *Merchant's theory of metal cutting*: An early model for prediction of forces during orthogonal cutting was developed by Ernst and Merchant [57-60]. This mechanistic model is based on the idealized assumption of existence of a single shear plane that separates the chip from the workpiece and on which the maximum shear stress is observed. This model also assumes plane strain conditions for orthogonal cutting. Using the schematic diagram of forces shown in Figure 2.1, the following relations between the shear force,  $F_s$ , friction and normal forces at the tool-chip interface,  $F$  and  $N$ , and the cutting and thrust force,  $F_C$  and  $F_T$ , can be established.

$$F_s = F_C \cos \phi - F_T \sin \phi \quad (2-1)$$

$$F = F_C \sin \gamma + F_T \cos \gamma \quad (2-2)$$

$$N = F_C \cos \gamma - F_T \sin \gamma \quad (2-3)$$

where  $\phi$  and  $\gamma$  are the shear and rake angles, respectively. Having obtained the shear force and by using shear flow stress,  $\tau_f$ , as a material property, the cutting and thrust forces can be predicted for the orthogonal cutting process:

$$F_C = \tau_f b h \left[ \frac{\cos(\mu - \gamma)}{\cos(\phi + \mu - \gamma) \sin \phi} \right] \quad (2-4)$$

$$F_T = \tau_f b h \left[ \frac{\sin(\mu - \gamma)}{\cos(\phi + \mu - \gamma) \sin \phi} \right] \quad (2-5)$$

where  $b$  and  $h$  are the width of cut and uncut chip thickness, respectively.  $\mu$  represents the friction angle.

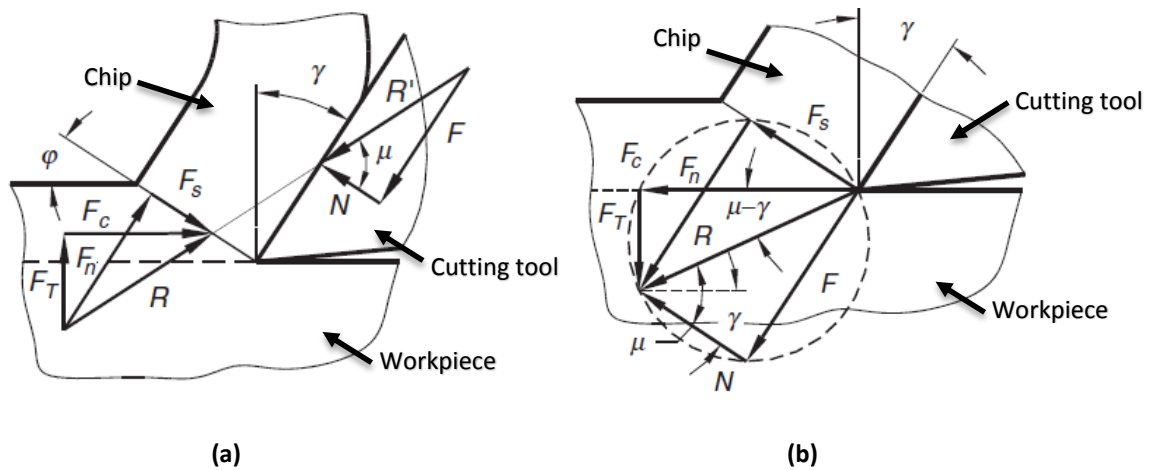


**Figure 2.1** Schematic diagram of forces in single shear plane model: (a) Free body diagram of chip; (b) Merchant's cutting force circle [61]

An important aspect of using Merchant's model for prediction of cutting force is prediction of shear angle. Analytical models for prediction of shear angle are usually developed based on the assumption of a rigid-perfectly plastic workpiece material [62].

An equation for calculation of shear angle was proposed by Lee and Shaffer [63] using the slip-line field theory:

$$\phi = \frac{\pi}{4} - \mu + \gamma \quad (2-6)$$

The same equation can be obtained using the maximum shear stress principle [62]. Using the minimum energy principle, Merchant [59] proposed the following equation for obtaining the shear angle.

$$\phi = \frac{\pi}{4} - \frac{\mu}{2} + \frac{\gamma}{2} \quad (2-7)$$

It should be noted that the above-mentioned models cannot always provide an accurate prediction of shear angle; these models are based on over-simplifying assumptions and their results in some cases can be far from experimental measurements. For instance, Kobayashi and Thomsen [64] showed that Merchant's model for shear angle provides a limiting value which may be different from the actual value in many cutting conditions.

b. *Oxley's theory of metal cutting*: The theory of metal cutting proposed by Oxley [65-68] is aimed at calculating the shear angle through analysis of the stress distribution on the shear plane and at the tool-chip interface. In this theory, empirical relations are used for calculation of stress, strain rate, and temperature at the shear plane. Having obtained these values, the shear angle will be calculated in a way that the resultant forces at the shear plane and the tool-chip interface are in equilibrium. Oxley's theory can be extended

for application to oblique cutting conditions using the method proposed by Arsecularatne et al. [69-71].

c. *Energy-based model of metal cutting*: Analysis of metal cutting using the single shear plane model, as presented in the Merchant's theory of metal cutting, has been criticized by researchers for its oversimplification of the metal cutting problem [61, 72]. As a result, this theory cannot provide accurate predictions of cutting forces. In order to overcome the obstacles of Merchant's theory, calculation of cutting force based on consumption of power in the machining system has been proposed [61, 73, 74]. This methodology uses the partition of power in metal cutting to calculate the total power and cutting force. This technique has been employed for prediction of cutting force during broaching operation [75].

According to Astakhov and Xiao [74], the total power consumption in the cutting system,  $P_c$ , is the sum of power consumption for plastic deformation,  $P_{pd}$ , power spent at the tool-chip interface,  $P_{tc}$ , power spent at the tool-workpiece interface,  $P_{tw}$ , power required for formation of new surfaces,  $P_{fns}$ , and the power spent due to the effect of the minor cutting edge,  $P_{mnc}$ :

$$P_c = P_{pd} + P_{tc} + P_{tw} + P_{fns} + P_{mnc} \quad (2-8)$$

Using this model, the cutting force,  $F_c$ , can be calculated as:

$$F_c = \frac{P_c}{v} \quad (2-9)$$

where  $v$  is the cutting velocity. The equations for calculation of each of power components have been provided by Astakhov and Xiao [74].

**2.5.3 Machining models for MMCs:** The two main approaches towards studying machining in general, namely the mechanistic approach and the energy-based approach, have been employed for investigating the particular case of MMC machining process. The models presented by researchers in this field will be reviewed in this section.

a. *Mechanistic modeling:* A mechanistic model for prediction of cutting force during machining MMCs is proposed by Pramanik et al. [11]. In this research, Merchant's single shear plane model is used for obtaining the force required for chip formation. The effect of nose radius is incorporated in the model using the equivalent cutting edge technique suggested by Colwell [73]. The ploughing force is assumed to be caused by the metal matrix and is calculated using the slip line field model presented by Waldorf [76-79]. The model presented by Pramanik et al. also included a new empirical equation for predicting the shear angle as shown in the following equation [11].

$$\phi = \frac{\pi}{5} - \frac{1}{2}(\mu - \gamma) \quad (2-10)$$

Another model for cutting force prediction during MMC machining is developed by Sikder and Kishawy [12]. This model is also based on Merchant's single shear plane model. However, in this model the Johnson-Cook constitutive equation [80] is used to calculate the matrix material shear flow stress. The friction at the tool-chip interface is obtained using the model proposed by Dabade et al. [81]. Particle fracture and debonding is also

incorporated in the model through utilization of equations developed by Pramanik et al [82] and Kishawy et al. [10].

b. *Energy-based modeling*: As previously mentioned, the fundamental assumptions included in single shear plane models make them inherently inaccurate. On the other hand, energy based models can provide more accurate predictions of the machining process.

An energy-based model for prediction of cutting force during machining MMCs is developed by Kishawy et al. [10]. In this force model, the total energy required for removal of unit volume of material,  $e$ , is calculated as the sum of specific energy for plastic deformation in the primary shear zone,  $E_p$ , specific energy for plastic deformation in the secondary shear zone,  $E_s$ , and the energy per unit volume required for debonding of particles,  $E_D$ :

$$e = E_p + E_s + E_D \quad (2-11)$$

Equations for calculation of the energy components are detailed by Kishawy et al. [10]. Although adopting the energy-based approach in this model eliminates the inaccuracies related to mechanistic models, it fails to account for interactions at the tool-chip and tool-workpiece interfaces. Moreover, the main characteristics of MMCs, namely the volume fraction and size of reinforcements, are not explicitly incorporated in the cutting force prediction process.

**2.5.4 Constitutive equations for modeling MMC cutting:** Mechanics of chip formation and cutting process are mainly affected by the behavior of workpiece material during machining. Constitutive models are used for simulation of this behavior. These models are developed in the form of relations between flow stress, strain, strain rate, and temperature.

Another area of significant use for constitutive equations is in finite element simulation. During the machining process, workpiece material undergoes high deformations which can cause extreme strain and strain rate and rapid rise in the temperature. Therefore, the constitutive equation employed in the FEM should provide a relation between stress and strain along with its dependence on strain rate, temperature, and work hardening.

Another important issue in Lagrangian or Arbitrary Lagrangian-Eulerian (ALE) methods of finite element analysis is the chip separation criterion. Fracture models can be used to model the initiation and evolution of damage in material and formation of chip during machining. The effects of strain rate and temperature should also be incorporated in the fracture models that are to be used for the cutting process.

a. *Constitutive models for monolithic material behavior:* Various constitutive models have been proposed for simulation of material behavior. Among these models, the Johnson-

Cook model [80], the Maekawa model [83, 84], the Bammann-Chiesa-Johnson model [85], and the micromechanical models [86, 87] are more frequently employed by researchers.

One of the most commonly used constitutive models for simulating the behavior of materials subjected to large strain, high strain rate, and high temperature is presented by Johnson and Cook [80]. They analyzed the results of torsion tests, static tensile tests, and dynamic Hopkinson bar tensile tests for various materials to obtain the data required for the model. The basic form of their model for the von Mises flow stress,  $\sigma$ , is expressed in the following equation:

$$\sigma = (A + B\epsilon^n) \left[ 1 + C \ln\left(\frac{\dot{\epsilon}}{\dot{\epsilon}_0}\right) \right] \left[ 1 - \left( \frac{T - T_{\text{transition}}}{T_{\text{melt}} - T_{\text{transition}}} \right)^m \right] \quad (2-12)$$

In this equation,  $\epsilon$  is the equivalent plastic strain,  $\dot{\epsilon}$  is the plastic strain rate, and  $\dot{\epsilon}_0$  is the reference strain rate.  $T$  and  $T_{\text{melt}}$  are the current temperature and the material melting temperature, respectively.  $T_{\text{transition}}$  is the transition temperature defined as the temperature below which material behavior has no temperature dependence. The five material constants,  $A, B, C, n$ , and  $m$  are obtained using the aforementioned material tests.

Johnson and Cook [88, 89] also developed a model for predicting damage and fracture during dynamic loading. This model accounts for damage accumulation in the material as a function of strain rate, temperature, and pressure.

Based on the Johnson-Cook fracture model, damage in an element is defined as:

$$D = \sum \frac{\Delta\epsilon}{\epsilon^f} \quad (2-13)$$

where  $\Delta\epsilon$  is the change in the equivalent plastic strain during each integration cycle and  $\epsilon^f$  is the equivalent strain to fracture as a function of temperature, strain rate, equivalent stress, and pressure.  $D$  is a parameter for quantifying damage in the element and fracture will occur when  $D = 1.0$ .

The strain to fracture can be calculated using the following expression:

$$\epsilon^f = (D_1 + D_2 e^{D_3 \sigma^*}) \left[ 1 + D_4 \ln \left( \frac{\dot{\epsilon}}{\dot{\epsilon}_0} \right) \right] \left[ 1 + D_5 \left( \frac{T - T_{\text{transition}}}{T_{\text{melt}} - T_{\text{transition}}} \right) \right] \quad (2-14)$$

In this equation,  $\sigma^*$  is the dimensionless pressure-stress ratio (stress triaxiality) defined as  $\sigma^* = \sigma_m / \bar{\sigma}$  where  $\sigma_m$  is the average of three normal stresses and  $\bar{\sigma}$  is the von Mises equivalent stress.  $D_1 \dots D_5$  are material constants which can be obtained using torsion tests, Hopkinson bar tests, and quasi-static tensile tests. Equivalent stress and strain relationships are expressed as:

$$\bar{\sigma} = \sqrt{\frac{1}{2} [(\sigma_1 - \sigma_2)^2 + (\sigma_2 - \sigma_3)^2 + (\sigma_3 - \sigma_1)^2]} \quad (2-15)$$

$$\dot{\epsilon} = \left( \frac{1}{1 + \nu'} \right) \left\{ \sqrt{\frac{1}{2} [(\dot{\epsilon}_1 - \dot{\epsilon}_2)^2 + (\dot{\epsilon}_2 - \dot{\epsilon}_3)^2 + (\dot{\epsilon}_3 - \dot{\epsilon}_1)^2]} \right\} \quad (2-16)$$

$$= \sqrt{\frac{2}{9} [(\dot{\epsilon}_1 - \dot{\epsilon}_2)^2 + (\dot{\epsilon}_2 - \dot{\epsilon}_3)^2 + (\dot{\epsilon}_3 - \dot{\epsilon}_1)^2]}$$

$$\epsilon = \sum \dot{\epsilon} \Delta t \quad (2-17)$$

where  $\nu'$  is the effective Poisson's ratio ( $\nu' = 0.5$  for plastic strains).  $\sigma_1, \sigma_2$ , and  $\sigma_3$  are the principal stresses while  $\dot{\epsilon}_1, \dot{\epsilon}_2$ , and  $\dot{\epsilon}_3$  are the principal strain rates. It should be noted that equation (2-14) is only valid as long as  $\sigma^* \leq 1.5$ ; for higher values of hydrostatic stress, this equation will not provide acceptable results.

Johnson-Cook model is widely used in many applications for simulation of material behavior. However, because of some shortcomings that exist in this model, such as its failure to account for the coupling effects of strain, strain rate, and temperature, modifications have been proposed to this constitutive model [90-92].

It should be noted that the material models reviewed in this section are proposed for simulation of monolithic materials' behavior. Thus, for the case of MMC machining simulation, these models suffer from lack of an explicit relationship between the process parameters and the unique MMC features and, consequently, their application to MMCs can lead to inaccurate predictions.

b. *Fracture models for reinforcements in MMCs*: Fracture of reinforcements in composite materials has been studied by researchers in the past two decades as a means of understanding failure and fracture in composites. An early analysis, performed by Finot et al. [93, 94], focused on static response of MMCs under tensile load. In this work the parameters affecting the onset of crack within the particles and evolution of cracks through the MMC were studied using a micromechanical finite element analysis. An important outcome of this analysis is understanding the effect of particle fracture on the increase in stress triaxiality, which can affect the MMC flow stress.

Finite element analysis has proven itself as reliable tool for investigation of fracture characteristics in MMCs. FE analysis, combined with experimental studies, has been used by Kiser et al. [95] to understand the fracture behavior and develop a damage law for MMCs. A similar analysis has been performed by Ghosh and Moorthy [96] for MMCs with

a non-uniform microstructure. FEM cell models for brittle fracture in MMC particles has been developed by Eckschlager et al. [97-99]. A more recent investigation of MMC behavior during static and dynamic loading using a similar approach is performed by Bruzzi et al. [100-102]. Their simulation utilized more realistic models for prediction of particle fracture and, thus, provided more accurate results.

Analytical and empirical models have also been developed by researchers for understanding the fracture behavior of MMCs. Babout et al. [103] proposed a model for analysis of the competition between particle fracture and particle debonding and identifying the dominant damage mechanism in MMCs. Another analytical model is developed by Hauert et al. [104] to study particle fracture in MMCs with high volume fraction of reinforcements. An important finding of this research work is that when an MMC undergoes high strain, the damage in the particles can be linked to the strain in the composite rather than the average stress in the particles.

*c. Debonding models for reinforcements in MMCs:* Debonding models are used for prediction of initiation and progress of damage at the interface between the matrix and reinforcements. Early studies in this field employed the Griffith's approach [105] toward understanding the growth of cracks around inclusions in a matrix [106-108]. One of these studies is performed by Nicholson [109], which provides a critical radius for inclusions that would be detached under a specific stress. The Griffith's approach has also been in used in more recent research works for analysis of particle debonding in MMCs [10].

Simulation of debonding in finite element models is usually performed by the means of cohesive zone formulations. Needleman [110] presented a comprehensive framework for utilization of cohesive zone model in finite element analysis. This model can be used for description of the growth of crack at the interface from initial debonding through complete separation.

Tvergaard [111] developed a formulation similar to Needleman's model for prediction of separation in cohesive zone models. However, unlike Needleman's model, this model considered both normal and tangential displacements. This model was employed to simulate debonding of SiC whiskers in an aluminum matrix. Later, Tvergaard [112] used this coupled normal-tangential separation model to predict interfacial debonding of short fibers in mostly-particulate-reinforced metal matrix composites.

A general formulation for cohesive zone models is provided by Foulk et al. [113, 114]. This formulation facilitates prediction of crack growth and debonding through implementation of three-dimensional cohesive zone elements in the finite element model.

## **2.6 Closing remarks**

This chapter provided a review of the literature related to several aspects of metal removal process and the modeling of the machining process of MMCs. MMC cutting can be studied using both numerical and analytical approaches. These approaches have been used by researchers to provide a more comprehensive understanding of the mechanics

of chip formation for MMCs along with the unique characteristics of cutting these composites, such as fracture and debonding of reinforcements. In the next chapters, a novel approach toward finite element simulation and analytical modeling of MMC cutting will be presented.

# Chapter 3 Approach and Methodology

## 3.1 Approach

The background and review of previously published work on analysis of machining operations of metal matrix composites was presented in the previous chapter. Finite element analysis is the most common tool for simulation of the cutting process. This type of analysis can be classified into two categories: the macroscopic analysis which treats the composite as a macroscopically anisotropic material, and the microscopic analysis which considers the matrix-reinforcement interactions. In order to capture the detailed mechanics of the process, the microscopic finite element analysis of MMC machining process will provide a better prediction of the actual behavior of the composite material.

In this thesis, a microscopic finite element analysis of the machining process of a particulate-reinforced MMC will be performed. The results of this analysis will be validated through comparison with experimental data. This model will provide an improved understanding of the actual behavior of the composite material during the cutting process along with the interactions between the tool and particles, the tool and

the matrix, and particles and the matrix. The FE analysis can also be employed in investigation of various characteristics of the machined MMC, such as plastic deformations, and initiation and evolution of damage.

Although the chip removal process during the machining operation is unique in terms of temperature, stress, strain, and strain rate, it has been modeled by previous researchers using constitutive equations that provide a general form of knowledge regarding material behavior and are not specific to machining. Hence, their utilization in simulation of the process may result in inaccurate predictions.

Moreover, material models that have been used in the previous research works for studying MMC cutting are models that were originally developed for simulation of monolithic materials' behavior. Thus, these models lack an explicit relationship between the process parameters and the unique MMC features. In order to address this issue, in the next step, a novel constitutive model for simulation of the behavior of MMCs during machining will be developed. This model establishes a meaningful relationship between the MMC behavior and its unique features, namely reinforcement size and volume fraction.

## **3.2 Methodology**

The two-dimensional microscopic finite element model for MMC machining will be created and solved using Abaqus commercial FEM software. The workpiece material will consist of three phases: matrix, particle, and the particle-matrix interface. Matrix and

particle materials will be modeled using coupled temperature-displacement elements while the cohesive zone elements will be used for the interface. The cutting process will be simulated using dynamic temperature-displacement analysis to account for the effect of temperature on material behavior. The effects of mesh size on the numerical results will be investigated and an optimum mesh size will be employed. The results of the finite element analysis will be validated against experimental data.

In the next step, a model for prediction of cutting force during machining MMCs will be developed. A force model is an excellent tool for studying the relations between various aspects of the process, such as tool wear and damage in the workpiece material, and process parameters, namely cutting speed, feed rate, tool geometry, etc. The energy-based force model will rely on a constitutive equation for prediction of material behavior during the cutting process.

In order to develop a constitutive model for better description of MMC behavior during machining, the different parts of material behavior in the primary shear zone during chip formation will be investigated. For each part, the main three MMC phases, namely the ductile matrix, the brittle particle, and the cohesive particle-matrix interface, will be modeled. These models will then be incorporated in MMC constitutive equation. The resulting constitutive model will be in the form of a relation between flow stress and process and material characteristics, namely strain, strain rate, temperature, particle size, and volume fraction.

In the final step, the developed constitutive equation will be incorporated in the energy-based force model. This will enable making comparison between model predictions and experiments. Predicted results from the developed force model will be compared with experimental data in order to confirm the ability of the developed constitutive model in capturing MMC behavior during machining.

# Chapter 4 Finite Element Modeling of Machining Metal Matrix Composites

## 4.1 Introduction

In this chapter, the finite element modeling procedure for simulation of MMC cutting will be detailed. The investigation is performed using Abaqus/Explicit environment for an aluminum MMC reinforced with alumina particles. The simulation will focus only on orthogonal cutting using an ideally sharp cutting tool.

The presented FE analysis in this research is unique in terms of simulating the cutting process of the real composite material with all its phases; this is in contrast to the models available in the literature where either a simplified composite model (i.e. without modeling the interface) [54] or an equivalent homogeneous material (EHM) model (i.e. a model that considers MMC as a macroscopically homogenous material) [56] is used for simulation of MMC machining. Utilization of a comprehensive model of MMC behavior during cutting enables the FE analysis to predict the fracture and debonding of the reinforcements.

In this thesis, three finite element models will be developed and utilized for analysis of different aspects of machining MMCs. These models will be employed for studying various scenarios of tool-particle interactions, the effect of cutting speed on MMC machining, and the plastic deformations during MMC machining.

## 4.2 Problem description and modeling steps

Three finite element models for analysis of MMC machining process are developed: model I will be used for studying various scenarios of tool-particle interactions; model II will be used for analysis of the effect of cutting speed on MMC machining; and model III will be used for studying the plastic deformations during MMC machining.

Workpiece material parameters are provided in Table 4.1. Lagrangian modeling is employed as, unlike other types of analysis, it permits modeling of the behavior of non-plastic reinforcements as well as their interactions with the plastic matrix.

**Table 4.1 Workpiece material parameters**

Matrix material	Aluminum Al6061
Particle material	Alumina ( $\text{Al}_2\text{O}_3$ )
Particle volume fraction	10%, 20%
Average particle diameter	15 $\mu\text{m}$ , 17 $\mu\text{m}$ , 23 $\mu\text{m}$

The cutting process is performed using a tungsten carbide cutting tool. Tool geometry and cutting parameters used in analysis of the process are listed in Table 4.2.

**Table 4.2 Cutting parameters for the analysis**

Rake angle	0°, 6°, 30°
Clearance angle	3°, 11°
Cutting speed	30 m/min, 60 m/min, 85 m/min , 100 m/min
Depth of cut	0.1 mm
Width of cut	1 mm, 3 mm

The analysis utilizes an elastic material model for the tool. The behavior of the three phases of the composite material is simulated. Matrix and particles are modeled as thermal-elastic-plastic materials using quad thermal-displacement plain strain elements. The particle-matrix interface is modeled using cohesive zone elements which are appropriate options for modeling the interface with very small thickness.

The interface elements are tied to both matrix and particle surfaces. A sacrificial layer of elements is defined along the cutting path in order to simulate chip separation using progressive damage model. This layer consists of elements which will be deleted as soon as damage accumulation in the material reaches the maximum value and material fracture occurs.

The contact is defined between rake and flank surfaces of the tool and workpiece surfaces as well as the tool surfaces and the particle nodes. This will enable the model to simulate tool-particle interactions. The normal behavior at the contact area is defined using the “Hard” contact algorithm. This algorithm eliminates any penetration of one surface into another. The extended Coulomb friction model [115] is used for tangential behavior of contact definitions. This model represents the frictional stress in two distinct regions of sticking and sliding:

$$\begin{cases} \tau_{fric} = \beta \sigma_n & \text{when } \beta \sigma_n < \tau_{max} \\ \tau_{fric} = \tau_{max} & \text{when } \beta \sigma_n \geq \tau_{max} \end{cases} \quad (4-1)$$

where  $\tau_{fric}$  is the frictional shear stress on the surface,  $\sigma_n$  is the normal stress,  $\beta$  is the coefficient of friction, and  $\tau_{max}$  is the maximum possible shear stress on the contact surface. In this research,  $\tau_{max}$  is assumed to be equal to  $\sigma_y/\sqrt{3}$  where  $\sigma_y$  is the yield stress of the matrix material. This value is considered as a reasonable upper bound estimate for the maximum shear stress on the contact surface [3]. All the energy dissipated as a result of friction is transformed into heat and is distributed into the surfaces in contact.

In the finite element model, contacts are defined using the surface-to-surface contact model. In the tool-matrix contact, element-based surfaces are defined along the areas where the chip will be formed. For the tool-particle contacts, the exact fracture lines on the particles are not known. Thus, element-based surfaces along the fracture lines cannot be defined. In order to overcome this obstacle, node-based surfaces are defined on the whole particle region and are used in the tool-particle contact definition. As a result, any surface that is created due to fracture in the particles will participate in the contact with the tool and therefore, a more realistic simulation of tool-particle interactions will be achieved. A disadvantage of using node-based surface in contact definition is inaccuracy in solving contact equations, which may result in unwanted penetration between surfaces. This can be prevented by using a finer mesh on the node-based surface (particles) as compared to the cutting tool.

It should be noted that in the element-based surfaces for the tool-matrix contact, severe contact noise and unwanted penetrations can occur if there is a significant difference between the nodal masses of the master and slave surfaces. Thus, the element size on the rake and flank surfaces of the cutting tool are chosen in a way that, by considering the densities of the matrix and cutting tool, the nodal mass on the two contact surfaces are close to each other.

The bottom surface of the workpiece model has fixed boundary conditions in all directions. The right side of the cutting insert is limited to move in only one direction with a velocity input boundary condition.

Because of the very large deformations in the workpiece material during metal cutting, finite element modeling using the Lagrangian approach usually results in excessive mesh distortion and decline of the mesh quality. In order to circumvent this problem, in model III, which is used for analysis of plastic deformation in the matrix material, the Arbitrary Lagrangian-Eulerian (ALE) adaptive meshing technique is used. In this technique, the mesh in a region is allowed to move independently of the underlying material. Thus, as the material undergoes large deformations, the mesh is modified to avoid extreme distortion of elements and preserve the mesh quality. It should be noted that the ALE adaptive meshing technique does not alter the elements and connectivity between them (i.e. mesh topology).

In Abaqus, three algorithms are available for improving mesh quality during finite element simulation, namely volume smoothing, Laplacian smoothing, and equipotential smoothing [116].

In volume smoothing, for each node, the new location is calculated by obtaining the volume-weighted average of the centers of the elements surrounding the node. For example, if a node is shared by four elements, the volume-weighted average of the four element centers is calculated and used as the new location for the node. In Laplacian smoothing, the new position for each node is calculated as the average of the positions of all adjacent nodes which are connected by an element edge. The equipotential smoothing uses a higher-order average of surrounding nodes to calculate the new position for each node. For instance, in a 2D model, the average of the positions of eight nearest nodes is calculated and used as the new position for the node. Volume smoothing algorithm is the most robust algorithm for ALE adaptive meshing and is used for FE analysis in this thesis.

All finite element simulations are run on a DELL™ PRECISION T7500 workstation with two Intel® Xeon® quad-core 1.6 GHz processors and 12.0 GB of RAM. Since the solver runs on 8 processor cores, parallel solving method is used with domain parallelization [116]. In this method, the model will be decomposed into eight smaller domains and each domain will be solved using one core of the processor. In order for parallelization to run efficiently, domain decomposition should be performed in a way that computation load for the solver for all domains is approximately equal.

### 4.3 Material modeling

In order to capture the distinctive features of machining of MMCs, the unique material models of the matrix, particles, and the particle-matrix interface are included in the model as described below.

**4.3.1 Matrix material:** Matrix material is modeled using a thermal-elastic-plastic constitutive equation until fracture. Johnson-Cook plasticity model [80] is employed for simulation of matrix material behavior. Chip formation is simulated using element deletion in the sacrificial layer of elements. Element deletion is modeled using Johnson-Cook's model for progressive damage and fracture [89]. Johnson-Cook material constants for the Aluminum Al6061 matrix are provided in Table 4.3.

**Table 4.3 Johnson-Cook material properties for Al6061 aluminum matrix [117]**

$A$ (MPa)	$B$ (MPa)	$n$	$C$	$m$	$D_1$	$D_2$	$D_3$	$D_4$	$D_5$
324	114	0.42	0.002	1.34	-0.77	1.45	-0.47	0.0	1.60

**4.3.2 Particle material:** The alumina particles are modeled as perfectly elastic materials until failure. Particle fracture simulation is performed using the brittle cracking and brittle failure models. Particle material properties are given in Table 4.4.

**Table 4.4 Material properties for alumina particles [118]**

Flexural strength (MPa)	380
Conductivity (W.m <sup>-1</sup> .K <sup>-1</sup> )	33
Elastic modulus (GPa)	416
Poisson's ratio	0.231
Coefficient of thermal expansion (K <sup>-1</sup> )	4.6 × 10 <sup>-6</sup>
Specific heat (J.kg <sup>-1</sup> .K <sup>-1</sup> )	755

**4.3.3 Particle-matrix interface:** The interface between the particles and matrix is modeled using cohesive zone elements using a traction-separation law. Damage initiation in the interface is predicted using quadratic nominal stress criterion. According to this criterion, damage in the cohesive elements is initiated when the following quadratic interaction condition is satisfied [116]:

$$\left\{ \frac{\langle t_n \rangle}{t_n^o} \right\}^2 + \left\{ \frac{t_s}{t_s^o} \right\}^2 + \left\{ \frac{t_t}{t_t^o} \right\}^2 = 1 \quad (4-2)$$

Here,  $t_n$ ,  $t_s$ , and  $t_t$  are the normal, first direction shear, and second direction shear (in a three-dimensional problem) of the traction stress vector, respectively.  $t_n^o$ ,  $t_s^o$ , and  $t_t^o$  represent the maximum nominal normal, first direction shear, and second direction shear stress. The brackets  $\langle \rangle$  demonstrate that a pure compressive stress cannot initiate damage.

The progressive evolution of damage, which will result in failure of the cohesive element and its deletion, is modeled using the energy approach. In this approach, the energy dissipated as a result of damage in the element until failure is a prescribed value. This value is entered into the model as a material property. This property is equal to the

area under the traction-separation curve. Element will be deleted after the dissipated energy reaches the failure energy property. The interfacial failure energy ( $\Phi$ ) for the Al/Al<sub>2</sub>O<sub>3</sub> interface is selected as  $\Phi = 50 \text{ J/m}^2$ . This value is similar to the value used for simulation of damage in interface elements by Dandekar and Shin [56].

#### 4.4 Meshing

The matrix and the particle phases of the workpiece are meshed using quad thermal-displacement plane strain elements. For these phases, free meshing technique is used. In this meshing technique, mesh generation can be performed using two algorithms, namely the advancing front algorithm and the medial axis algorithm. In the advancing front algorithm, elements are first generated at the region boundary and then mesh generation continues towards the interior of region using a systematic approach. In the medial axis algorithm, the region is first divided into a group of smaller simple regions. Then each of the simple regions will be meshed using structured meshing technique. In regions with a large number of elements and a relatively simple geometry, the medial axis algorithm can generate a mesh with higher quality as opposed to the advancing front algorithm.

In model I, matrix is meshed using the advancing front algorithm while in model II and model III, the medial axis meshing algorithm is used. The cutting tool is meshed using quad thermal-displacement plane strain elements with structured meshing technique.

Meshing of the particle-matrix interface is performed using cohesive zone elements. In order to create zero-thickness elements, nodes on 1D line elements are copied onto themselves and then, 2D zero-thickness structured elements are formed using the nodes.

Dependence of the model results on the element size is investigated by comparing the cutting forces obtained from models with different mesh seeds. The average node distances in different parts of the optimum mesh for each of the models are detailed in Table 4.5. The meshed parts for the three models are shown in Figure 4.1, Figure 4.2, and Figure 4.3.

**Table 4.5 Average node distance in the optimum mesh**

	Model I	Model II	Model III
Edge of particles along the cutting line	2.00 $\mu\text{m}$	1.45 $\mu\text{m}$	1.30 $\mu\text{m}$
Edge of particles above the cutting line	2.36 $\mu\text{m}$	2.41 $\mu\text{m}$	1.36 $\mu\text{m}$
Edge of particles below the cutting line	2.36 $\mu\text{m}$	4.82 $\mu\text{m}$	4.71 $\mu\text{m}$
Matrix along the cutting line	4.00 $\mu\text{m}$	3.00 $\mu\text{m}$	5.00 $\mu\text{m}$
Matrix above the cutting line	4.43 $\mu\text{m}$	4.16 $\mu\text{m}$	2.70 $\mu\text{m}$
Matrix at the bottom	10.00 $\mu\text{m}$	25.00 $\mu\text{m}$	40.00 $\mu\text{m}$
Cohesive particle-matrix interface	0.48 $\mu\text{m}$	0.60 $\mu\text{m}$	0.50 $\mu\text{m}$

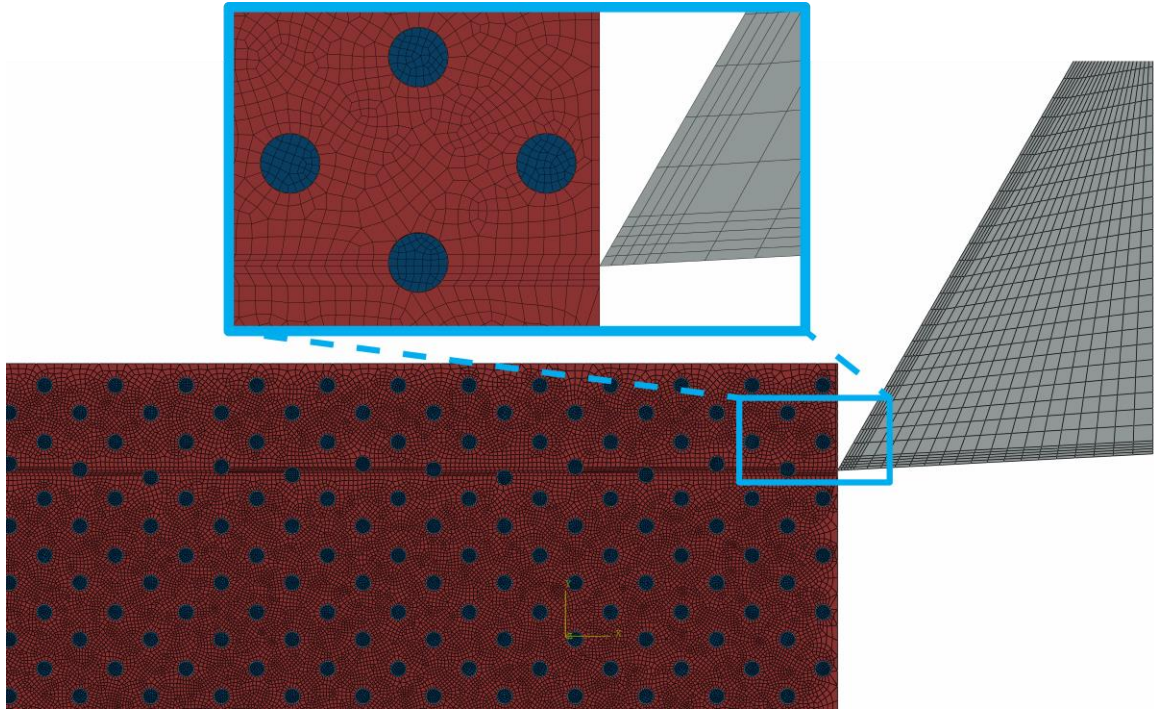


Figure 4.1 Meshed parts for the finite element analysis of model I (Al 6061/10% 15  $\mu\text{m}$   $\text{Al}_2\text{O}_3$ , rake angle=30°)

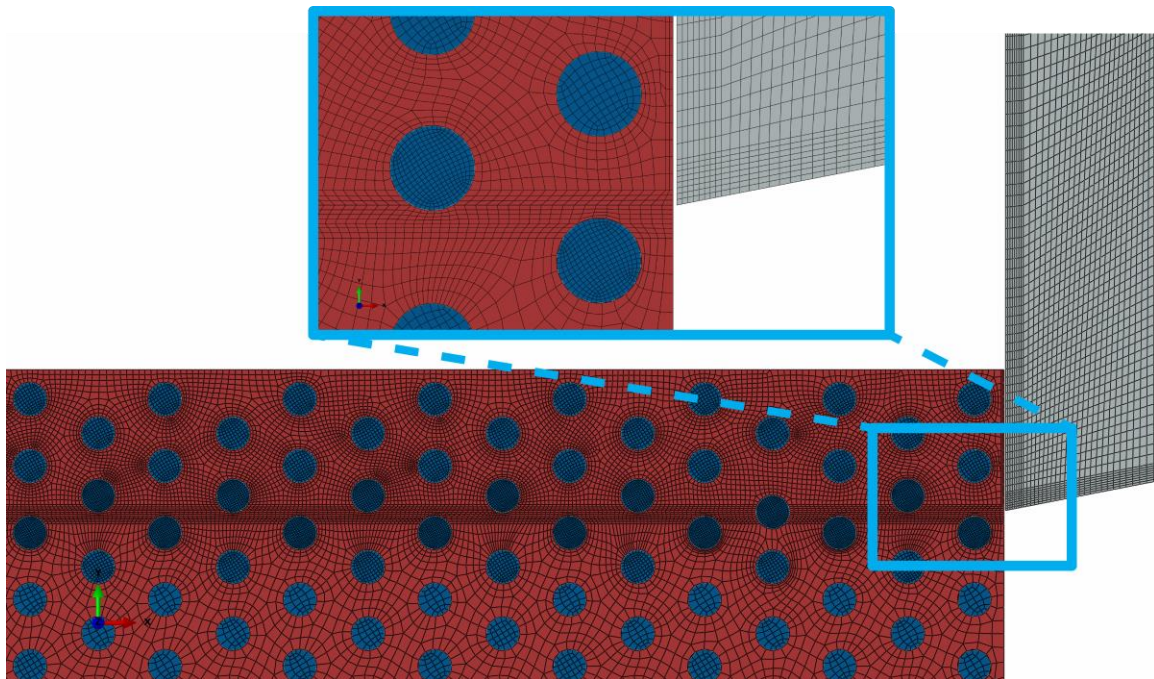


Figure 4.2 Meshed parts for the finite element analysis of model II (Al 6061/20% 23  $\mu\text{m}$   $\text{Al}_2\text{O}_3$ , rake angle=0°)

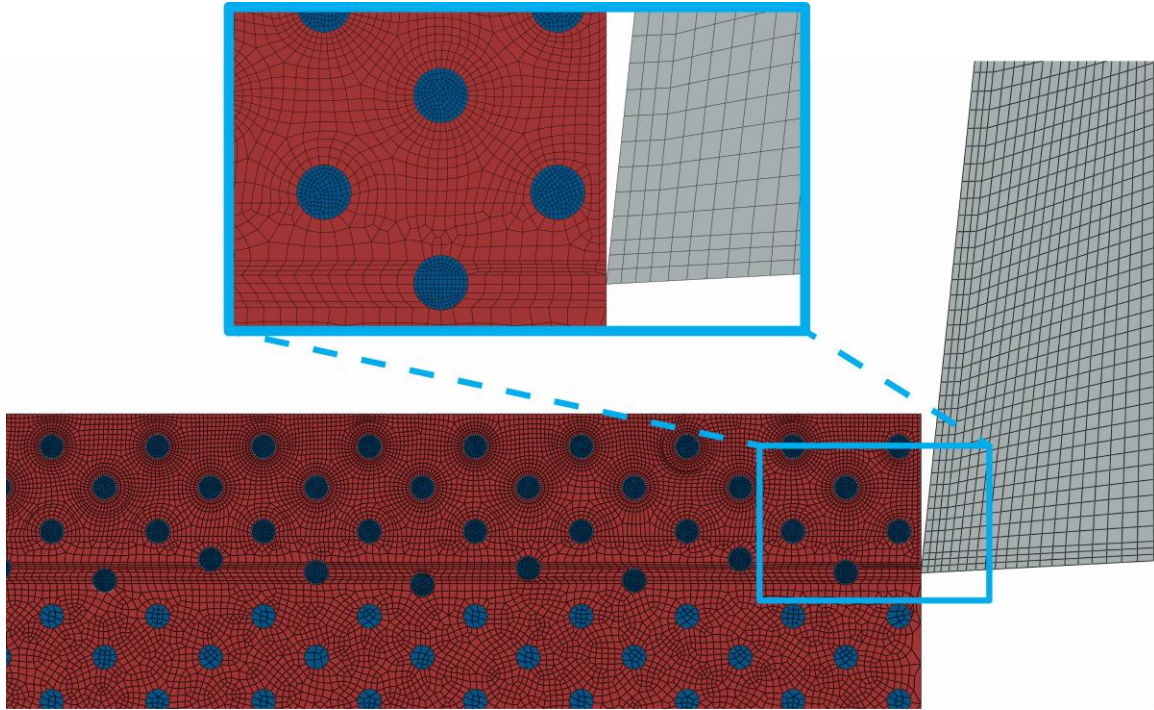


Figure 4.3 Meshed parts for the finite element analysis of model III (Al 6061/10% 17  $\mu\text{m}$   $\text{Al}_2\text{O}_3$ , rake angle=6°)

## 4.5 Results and discussion

The solution of the finite element model is performed using Abaqus. Results of the three finite element models will be presented and analyzed in this section.

### *4.5.1 Model I, analysis of various scenarios of tool-particle interactions:*

Investigation of the interactions between the cutting tool and reinforcements is an important part of understanding MMC machining. These interactions can cause fluctuations in the cutting force, deterioration of machined surface quality, and decline in the life of cutting tool. Tool-particle interactions during MMC cutting can lead to particles'

fracture, particles' debonding, or particles' squeeze into matrix material. The FE model will be able to capture these interactions and will be utilized for analyzing them.

a. *Model verification:* In order to validate the results of the finite element model, the obtained predicted values of the cutting force were compared with the experimental results from cutting tests performed under the same cutting conditions [53]. Comparison of the average cutting force during the steady phase of cutting process from the FEM and the one obtained in experiments is provided in Figure 4.4. As can be seen in this figure, the value of the cutting force obtained from the FE simulations is within the standard deviation error range of the experimental value. The difference between the average simulated and experimental values is 8.3%.

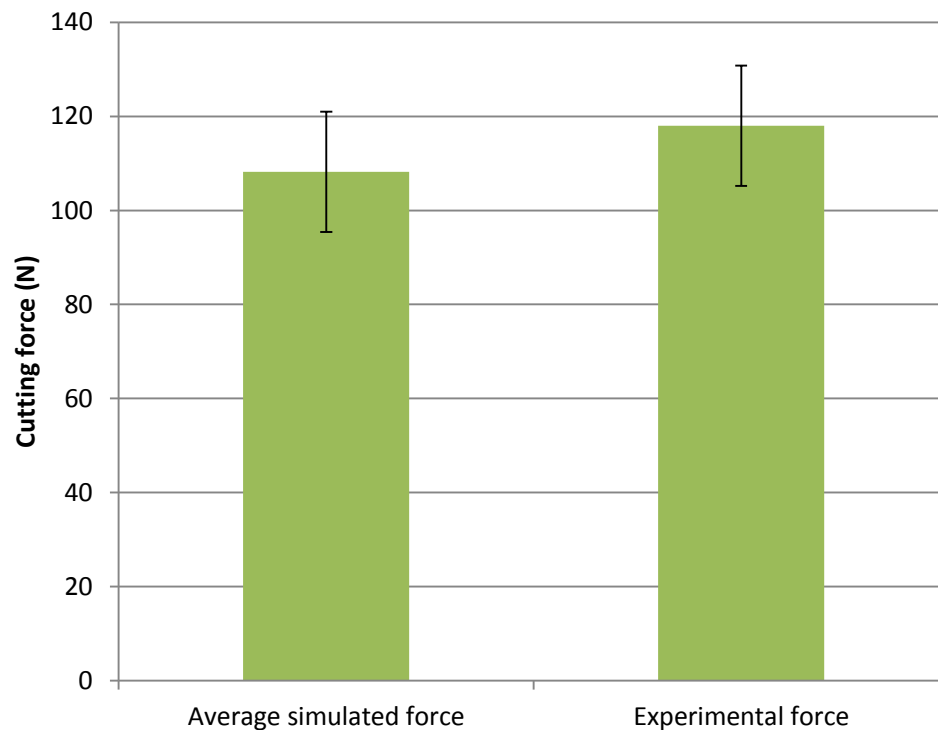


**Figure 4.4 Comparison of cutting forces obtained using FEM and experimental data [53] (Al 6061/10% 15  $\mu\text{m}$   $\text{Al}_2\text{O}_3$ ,  $v=85$  m/min, rake angle= $30^\circ$ , width of cut=3 mm)**

Figure 4.4 shows that the simulated cutting force is slightly smaller than the experimental force. This is expected in the finite element model since the cutting tool was assumed to be ideally sharp in the analysis, which is not the case in the actual machining tests. Even if the cutting tool is sharp at the beginning of the cut, the tool wear around the cutting edge will soon increase the cutting edge radius and thus the cutting force.

b. *Analysis of cutting force during machining:* Figure 4.5 shows the cutting force versus time obtained during finite element simulation of the steady phase of cutting process. Apparent in this figure are the peaks and troughs in the cutting force which are associated with the interactions between the cutting tool and reinforcements. It is evident from this figure that initiation and progress of crack in the particle can cause a drop in the cutting force. On the other hand, interaction of the particle with the cutting tool before the initiation of a crack results in an increase in the cutting force.

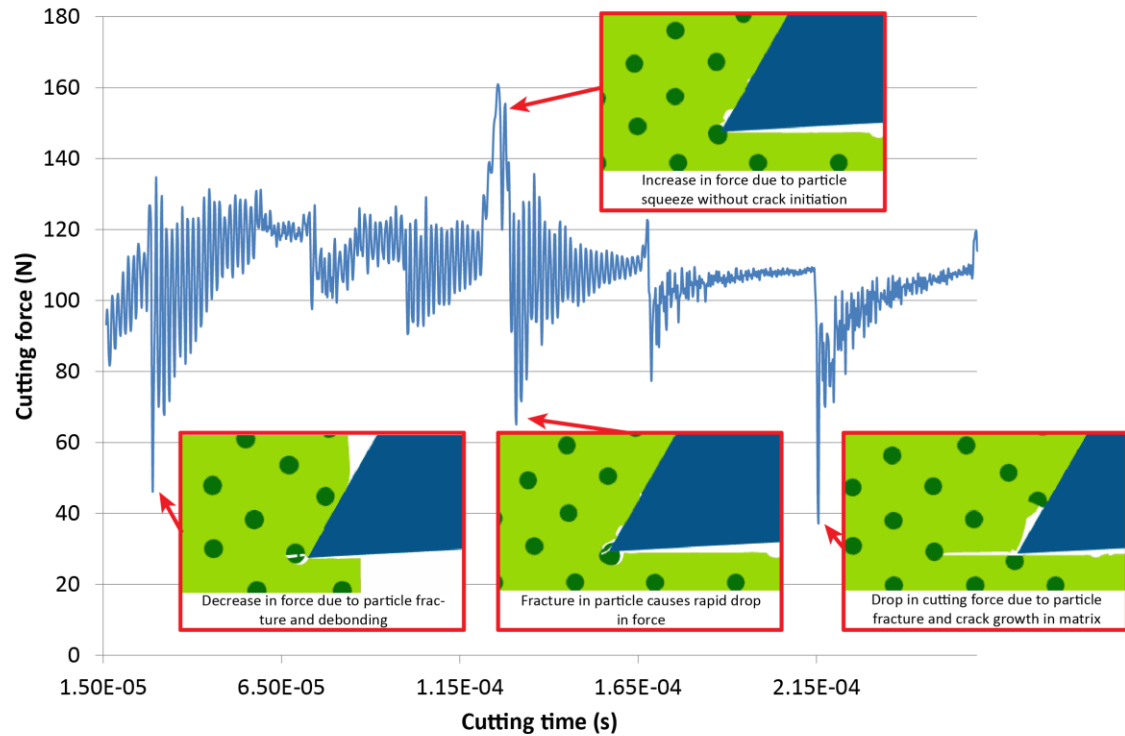


**Figure 4.5** Cutting forces obtained using finite element analysis (Al 6061/10% 15  $\mu\text{m}$   $\text{Al}_2\text{O}_3$ ,  $v=85$  m/min, rake angle= $30^\circ$ , width of cut=3 mm)

c. *Tool-particle interaction scenarios*: The ability of the developed FE model to simulate machining of the real MMC with all its phases makes it an appropriate tool for studying various interaction scenarios between the tool and particles. In this section, these interactions are studied for the particles close to the cutting path. Different cases of particle fracture and debonding can occur as the cutting tool approaches the particles. The main three scenarios for particles located along, above, and below cutting line are depicted in Figure 4.6. These cases will be analyzed in this section.

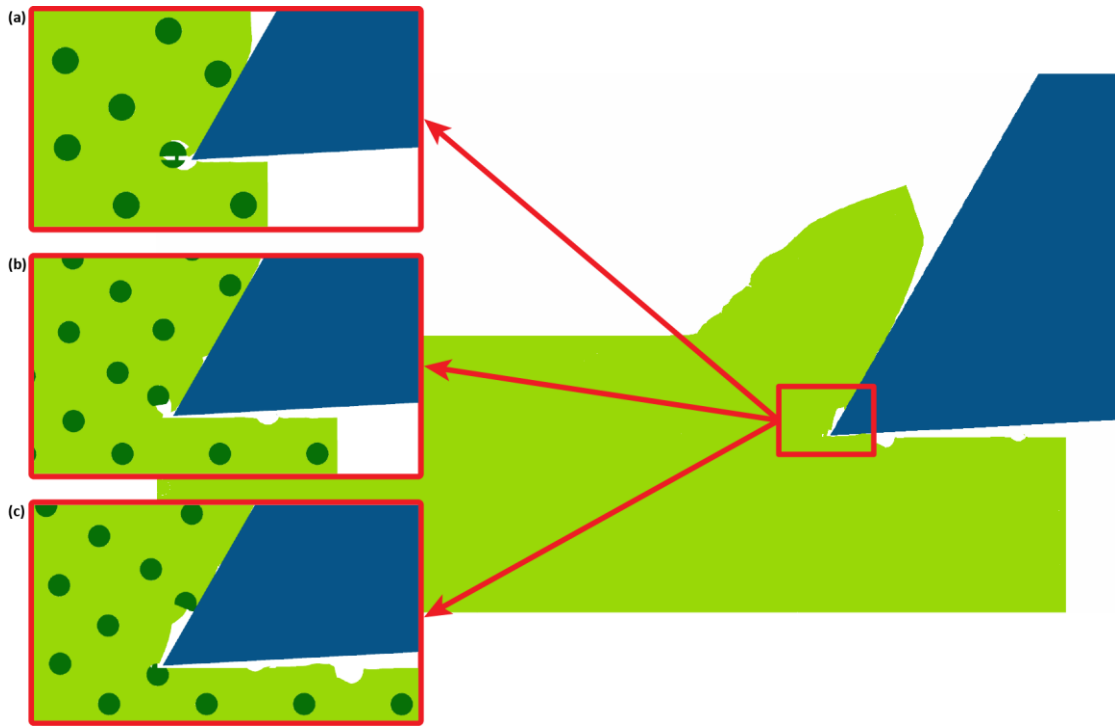


**Figure 4.6** Different scenarios of tool-particle interactions at three different time steps: (a) particle on the cutting line: fractured and debonded; (b) particle above the cutting line: pushed in the chip; (c) particle below cutting line: fractured and attached

Figure 4.7 shows the engagement of the cutting tool and a particle located along the cutting line. The cutting line passes through the central area of the particle. It is clear that as a result of engagement between the tool and the particle, the energy level has reached the critical value which is shown as deletion of cohesive interface elements. This indicates that debonding has started.

It is also apparent from Figure 4.7 that debonding of the particle initiated before any contact with the tool. This can be attributed to the plastic deformations in the matrix around the particle. Figure 4.8 shows the distribution of equivalent plastic strain around the debonded particle, where an increase in matrix plastic strain in the vicinity of the particle is observed.

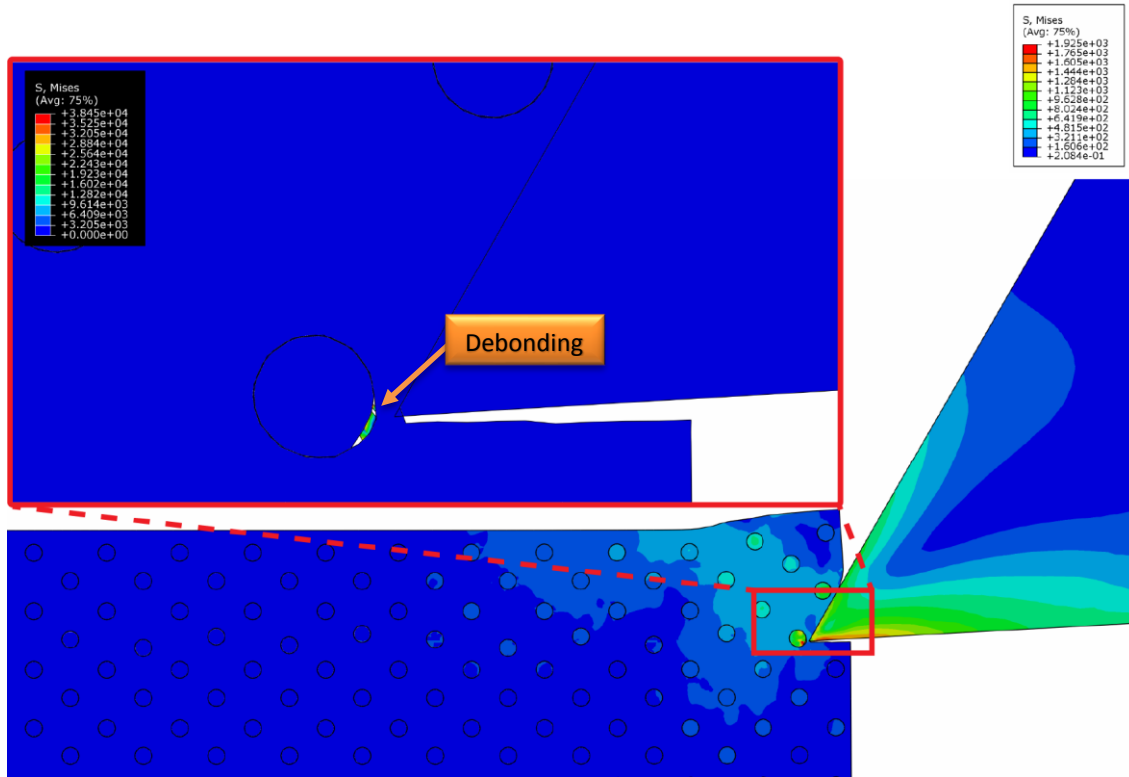


Figure 4.7 Stress (MPa) distribution during cutting tool engagement which results in particle debonding (Al 6061/10% 15  $\mu\text{m}$   $\text{Al}_2\text{O}_3$ ,  $v=85$  m/min, rake angle=30°, width of cut=3 mm)

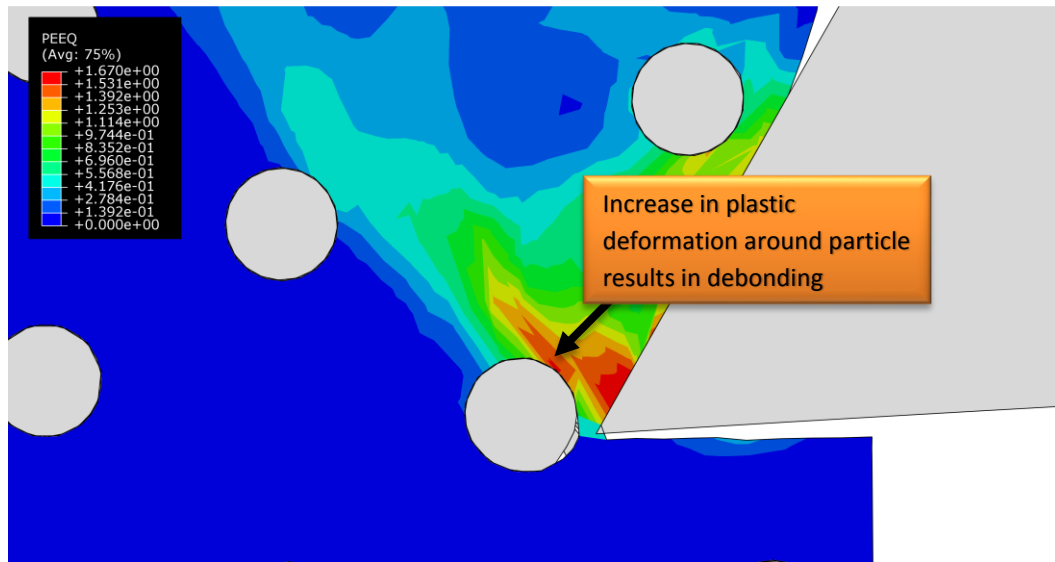
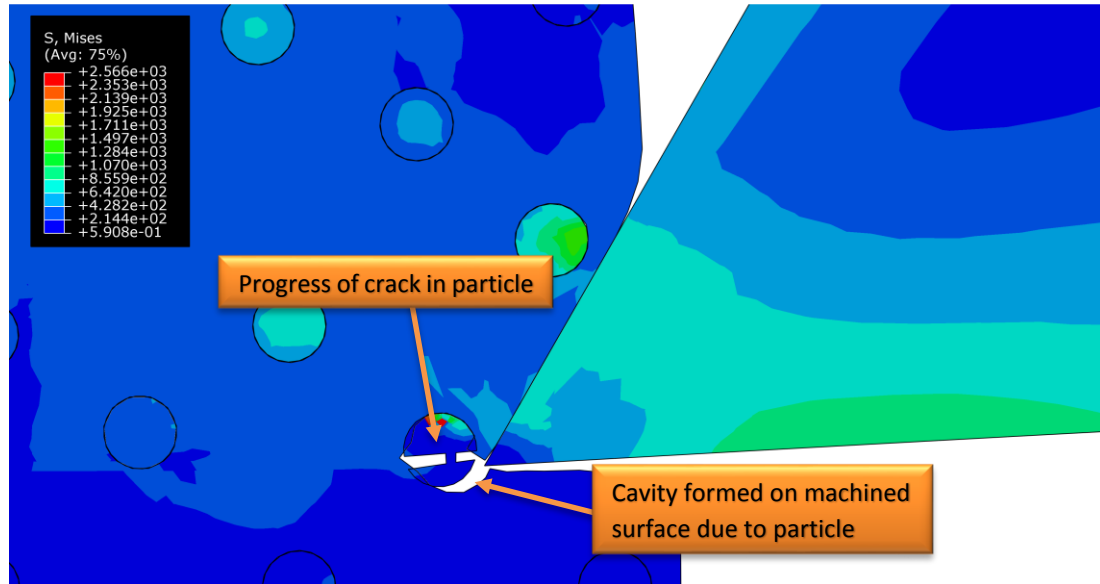


Figure 4.8 Distribution of equivalent plastic strain around the debonded particle (Al 6061/10% 15  $\mu\text{m}$   $\text{Al}_2\text{O}_3$ ,  $v=85$  m/min, rake angle=30°, width of cut=3 mm)

As the tool continues moving along its path, initiation and development of cracks become visible in the particle which is demonstrated in Figure 4.9. Moreover, it is evident

in this figure that as a result of debonding, cavities will be formed on the surface, which will consequently deteriorate the machined surface quality.



**Figure 4.9** Stress (MPa) distribution during initiation and growth of crack in the particle (Al 6061/10% 15  $\mu\text{m}$   $\text{Al}_2\text{O}_3$ ,  $v=85$  m/min, rake angle=30°, width of cut=3 mm)

Figure 4.10 shows the interaction between the cutting tool and a particle located slightly above the cutting line. In this case, the particle is debonded from the workpiece, but stays in the chip material. The stress distribution on the particle shows how the particle is pushed against the matrix material into the chip as a result of interaction with the cutting tool. This can be better understood by studying the pressure stress distribution as depicted in Figure 4.11. In this figure, the increase in pressure on the particles that are being forced into the chip material is evident.

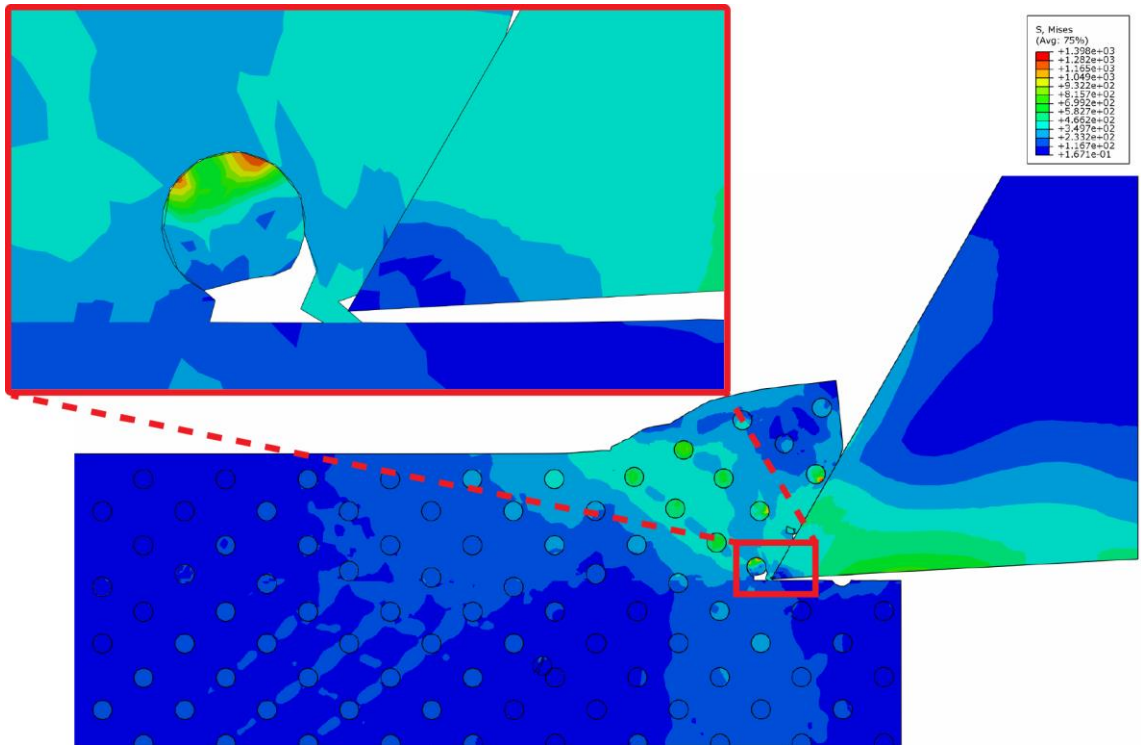


Figure 4.10 Stress (MPa) distribution during debonding of the particle while being pushed into the chip (Al 6061/10% 15  $\mu\text{m}$   $\text{Al}_2\text{O}_3$ ,  $v=85$  m/min, rake angle=30°, width of cut=3 mm)

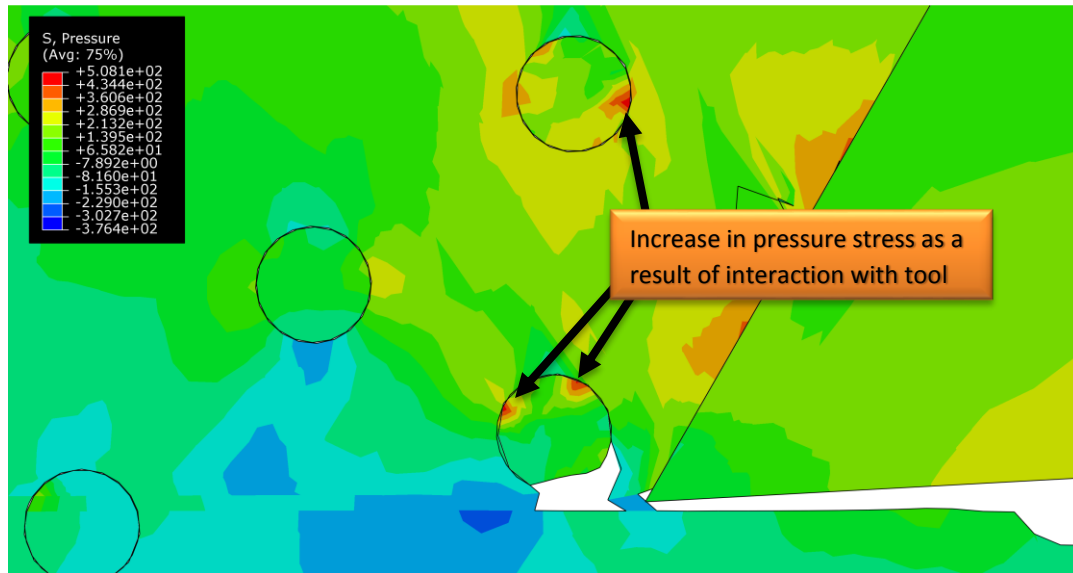
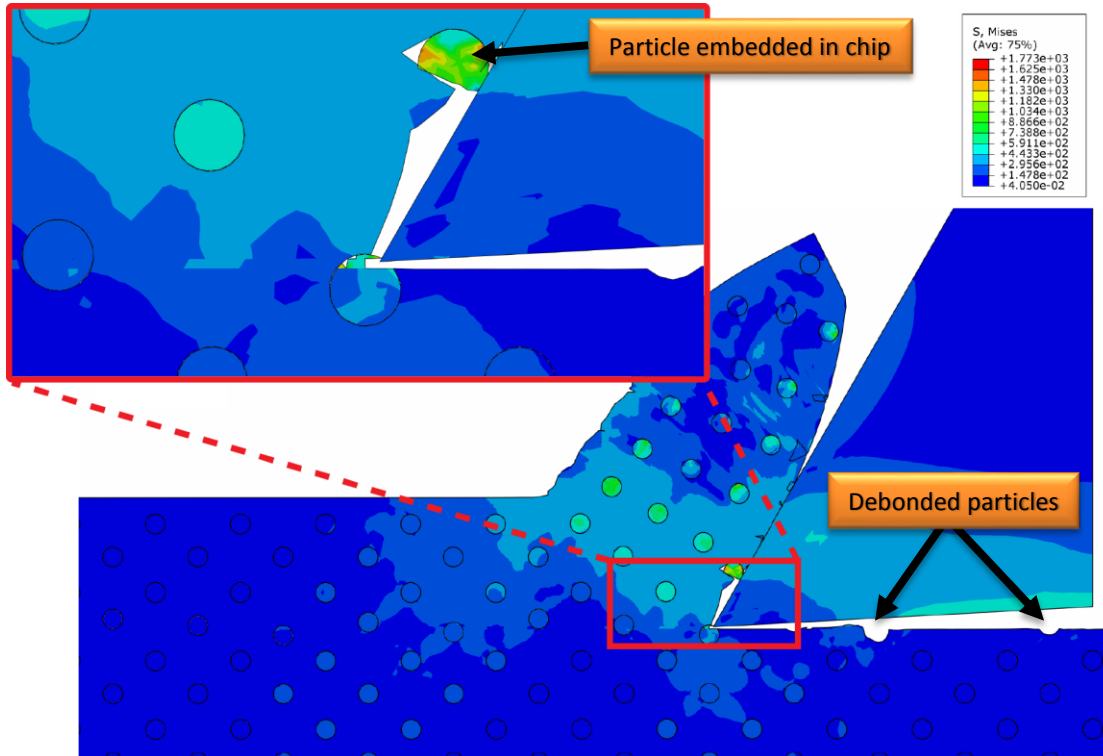


Figure 4.11 Pressure stress (MPa) distribution during debonding of the particle (Al 6061/10% 15  $\mu\text{m}$   $\text{Al}_2\text{O}_3$ ,  $v=85$  m/min, rake angle=30°, width of cut=3 mm)

In Figure 4.12, stress distribution during the interaction between the cutting tool and a particle below the cutting line is shown. It is clear that in spite of the fracture of a

small portion of the particle, the larger part of the particulate reinforcement stays bonded to the workpiece material. As a result, a massive increase in surface roughness will not be expected in this scenario. Figure 4.12 also shows particles embedded in the chip during cutting MMC.



**Figure 4.12** Stress (MPa) distribution during crack propagation in a particle below the cutting line (Al 6061/10% 15  $\mu\text{m}$   $\text{Al}_2\text{O}_3$ ,  $v=85$  m/min, rake angle=30°, width of cut=3 mm)

In order to better analyze the scenarios of interactions between the cutting tool and reinforcements, the plastic deformation in the matrix material around the particles is studied. Figure 4.13 shows the plastic strain in the matrix material around the particle versus distance along the particle perimeter. This graph is plotted for the three cases of the particle lying on, below, or above the cutting line. It is evident in this graph that high plastic deformation in the matrix material adjacent to the reinforcement can cause

debonding; the plastic strain around the particle on the cutting line is the highest which results in immediate debonding. On the other hand, the low plastic strain around the particle below the cutting line means the particle stays bonded to the matrix.

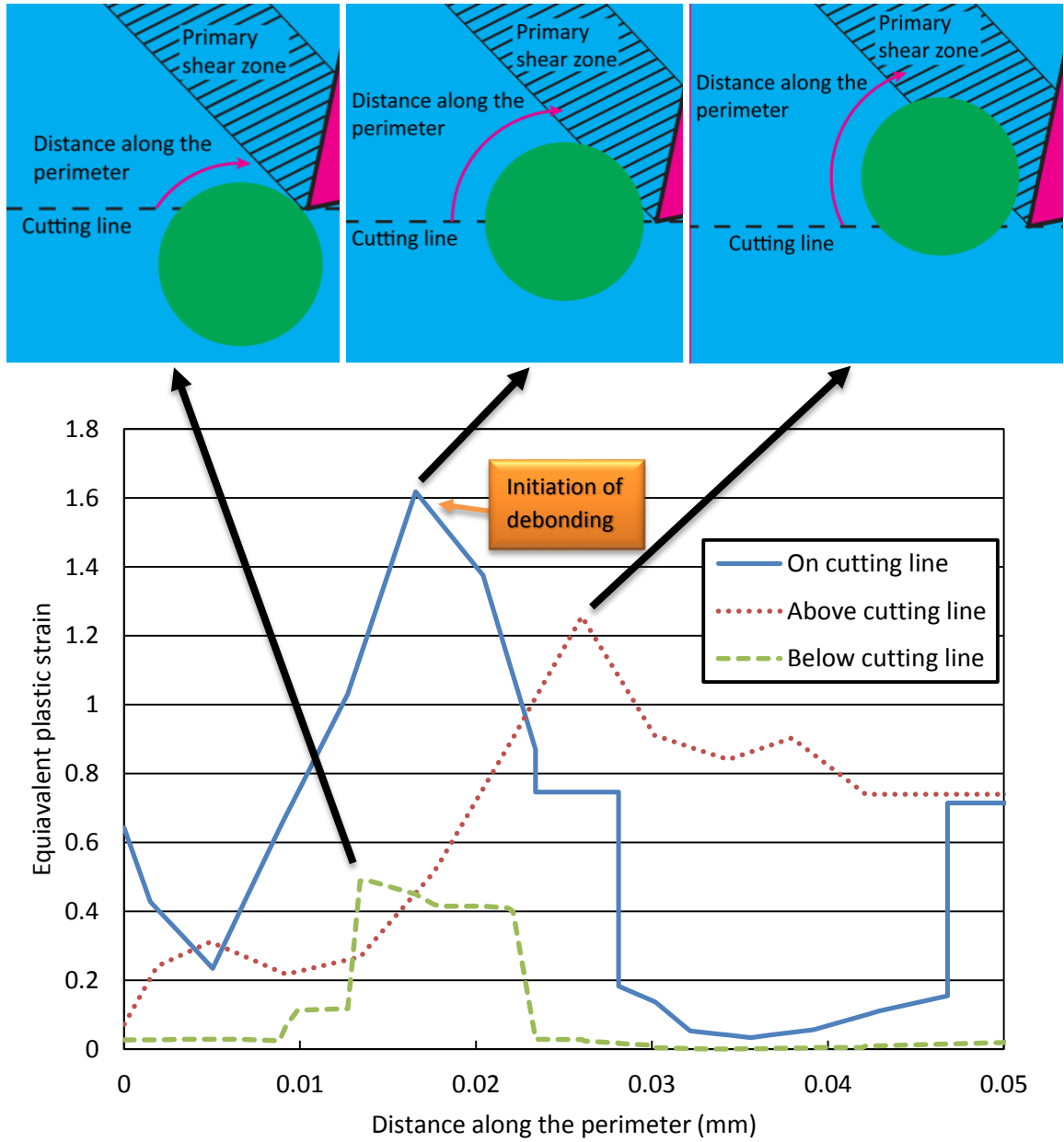


**Figure 4.13** Equivalent plastic strain in the matrix material versus distance along the perimeter around the particle for various tool-particle interaction scenarios (Al 6061/10% 15  $\mu\text{m}$   $\text{Al}_2\text{O}_3$ ,  $v=85$  m/min, rake angle=30°, width of cut=3 mm)

The knowledge regarding tool-particle interactions presented in this section is a great asset in studying the MMC machining system. This knowledge can only be achieved by means of a comprehensive finite element model which simulates all phases of a real composite.

**4.5.2 Model II, analysis of the effect of cutting speed:** The machining of MMCs, like any other machining process, is significantly affected by the cutting speed. Change in cutting speed can considerably alter the behavior of MMC during the metal removal process and can result in different levels of stress, temperature, and damage in the workpiece material. In this section, the developed finite element model will be utilized to investigate the effect of cutting speed on MMC machining and particularly the interactions between the matrix and particle which is well depicted in the developed model.

a. *Model verification:* Simulated cutting forces obtained from FE analysis are first compared with experimental data to verify the model predictions and its sensitivity to the cutting speed, as illustrated in Figure 4.14. This figure shows that the developed FE model can provide an accurate prediction of cutting forces for various cutting speeds. The average difference between FE predictions and experimental values for all cutting speeds is 8.63%. This difference can be attributed to the tool wear in cutting tests which increases

the cutting force as compared to the FE simulations, where the cutting tool is assumed to be ideally sharp.

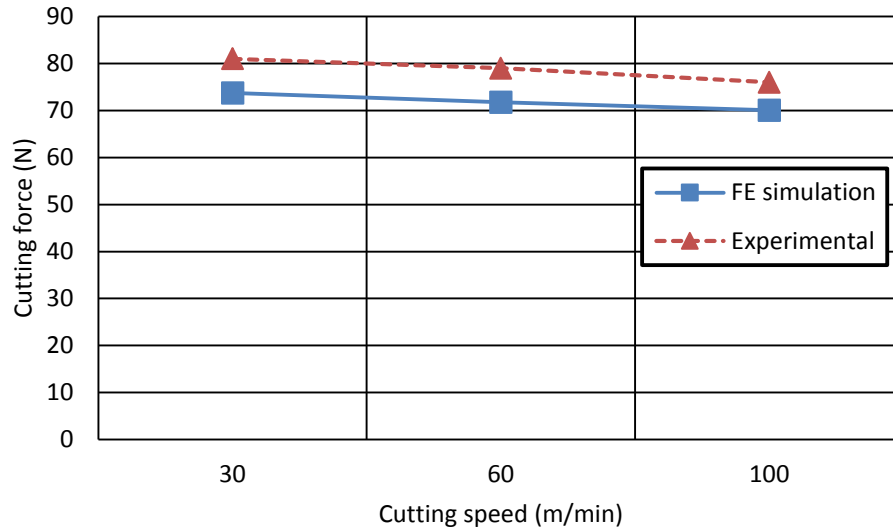


**Figure 4.14 Comparison of cutting forces obtained using FE simulations and experiments (Al 6061/20% 23  $\mu\text{m}$   $\text{Al}_2\text{O}_3$ , rake angle=0°, width of cut=1 mm)**

b. *Analysis of tool-workpiece interactions:* An important application of finite element modeling is in analysis of the interactions between the cutting tool and the workpiece MMC. In this section, the developed FE model will be used for studying various types of tool-workpiece interactions.

Figure 4.15 shows the interaction between the cutting insert and the particle located along the cutting line. This interaction leads to debonding of the reinforcement and removal of the particle from the matrix. As a result, cavities are formed on the machined surface which can result in deterioration of machined surface quality.

In Figure 4.15, two instances of the cohesive elements at the particle-matrix interface are depicted. These cohesive elements have an initial thickness of zero.

However, as a result of deformations during cutting, traction at the interface will increase and will lead to increased thickness of the interface elements. For the particle inside the chip, interface traction does not cause deletion of cohesive elements and thus, particle debonding does not occur. However, for the particle on the cutting line, as shown in Figure 4.15, cohesive elements are deleted due to interface traction and particle is detached from the matrix.

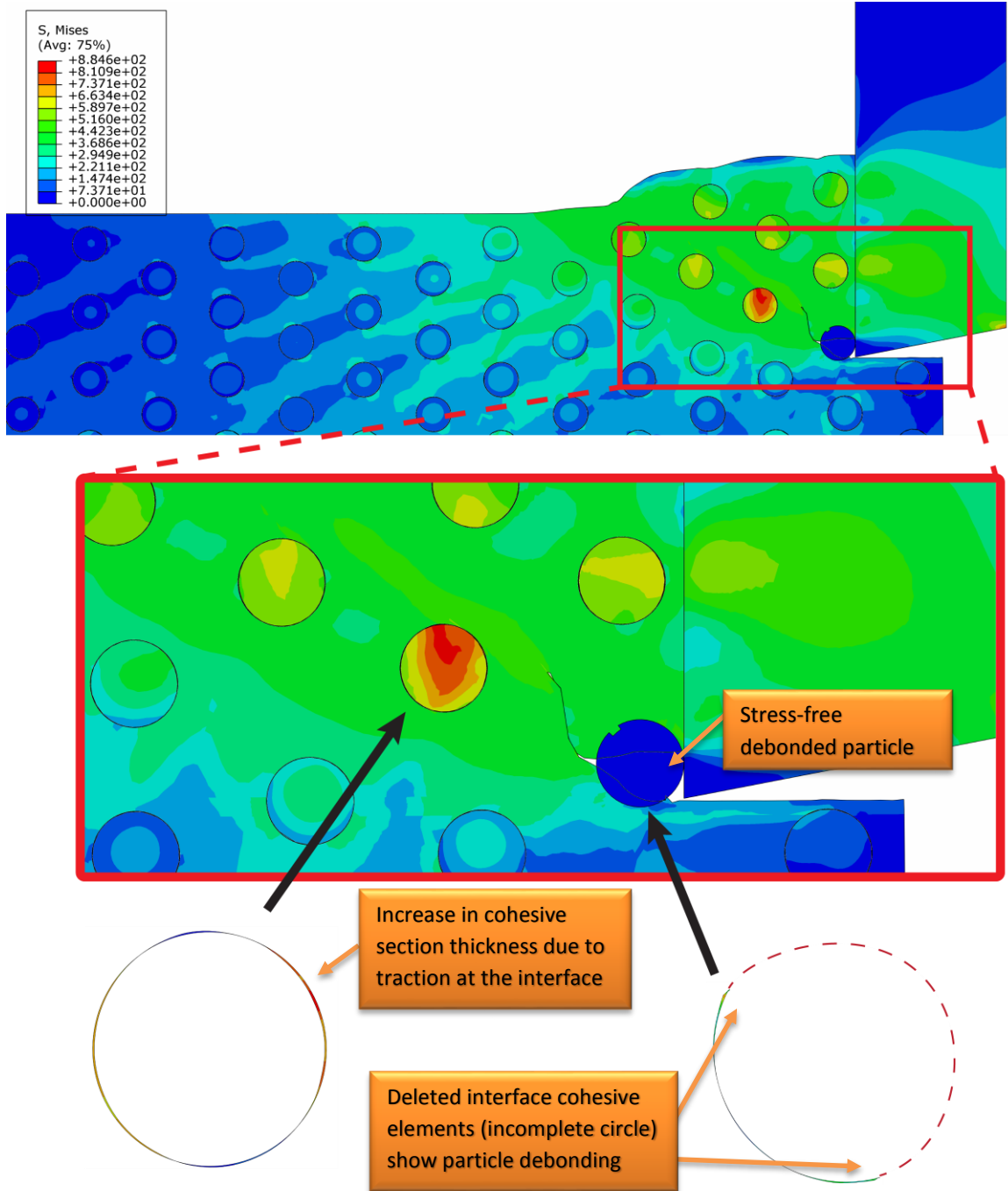


Figure 4.15 Interaction between cutting insert and particle located along the cutting line (Unit: MPa) (Al 6061/20% 23  $\mu\text{m}$   $\text{Al}_2\text{O}_3$ ,  $v=60$  m/min, rake angle= $0^\circ$ , width of cut=1 mm)

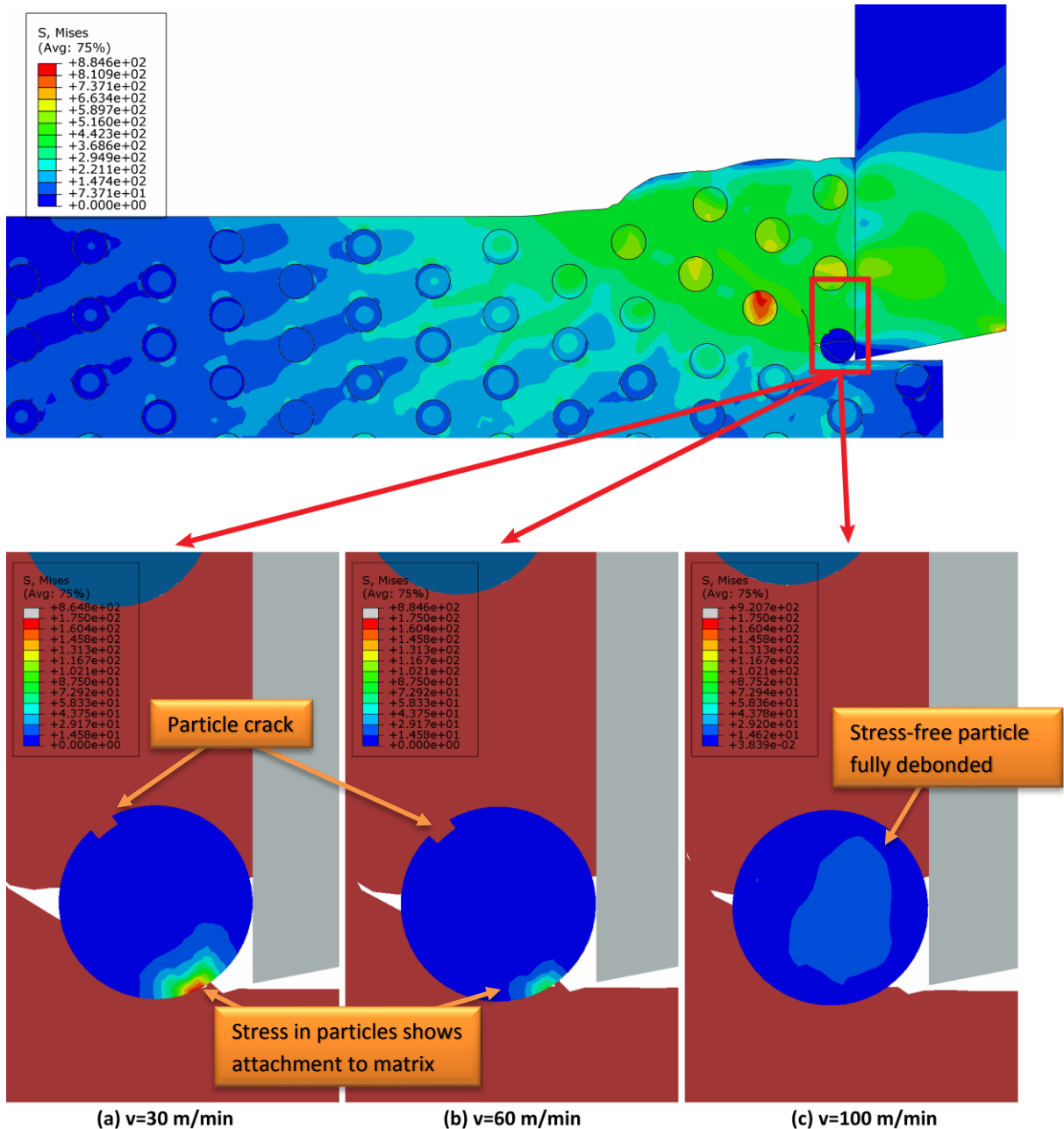


Figure 4.16 Stress (MPa) distribution during interaction in particles located along the cutting line (Al 6061/20% 23  $\mu\text{m}$   $\text{Al}_2\text{O}_3$ , rake angle=0°, width of cut=1 mm)

In Figure 4.16, stress distribution in the particle during the interaction with the cutting tool is depicted for different cutting speeds. Cracks in the particle are seen in this figure only for  $v=30$  m/min and  $v=60$  m/min. This figure also shows that particle debonding from the matrix occurs much faster as the cutting speed increases; while the

particle is fully stress-free and detached when  $v=100$  m/min, reinforcements are still attached to the matrix for the two lower cutting speeds.

In Figure 4.17 the interaction between the cutting tool and a particle with the center below the cutting line is illustrated. This interaction causes the fracture of reinforcement. As shown in Figure 4.17, for the fractured particle interacting with the cutting tool, some of the interface elements are deleted, though the fractured particle pieces are still attached to the matrix. Figure 4.17 also shows that for the particle above the cutting line in the chip, the interface cohesive elements are undamaged. Thus the particle is fully attached to matrix despite the traction that occurs at the interface.

Evolution of crack and particle fracture during this interaction is shown in Figure 4.18 to Figure 4.20. According to these figures, crack is initiated as a result of stress concentration when the particle comes in contact with the cutting tool (Figure 4.18). The crack is then progressed until complete fracture of the particle (Figure 4.19). As mentioned earlier, the particle pieces remain bonded to the matrix. One piece is pushed by the tool into the chip while the other remains in the matrix on the machined surface and avoid a massive deterioration of machines surface quality (Figure 4.20).

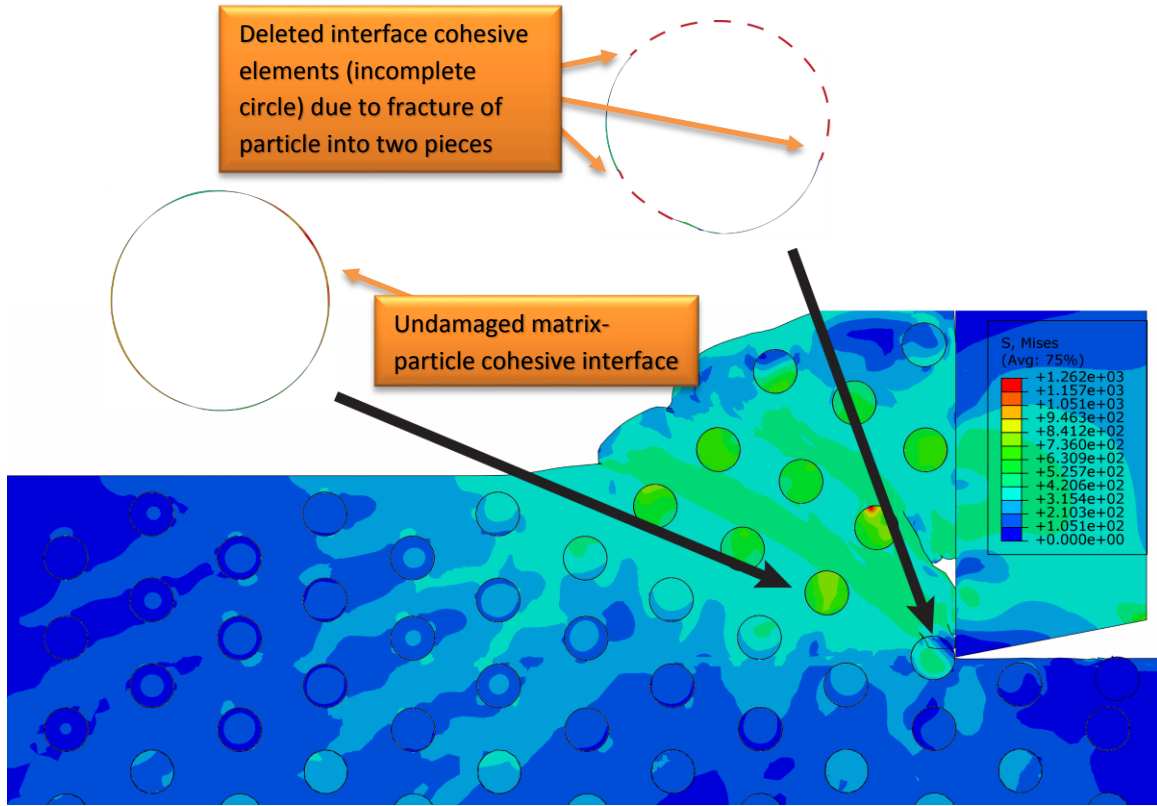


Figure 4.17 Interaction between cutting insert and particle located below the cutting line (Unit: MPa) (Al 6061/20% 23  $\mu\text{m}$   $\text{Al}_2\text{O}_3$ ,  $v=60$  m/min, rake angle= $0^\circ$ , width of cut=1 mm)

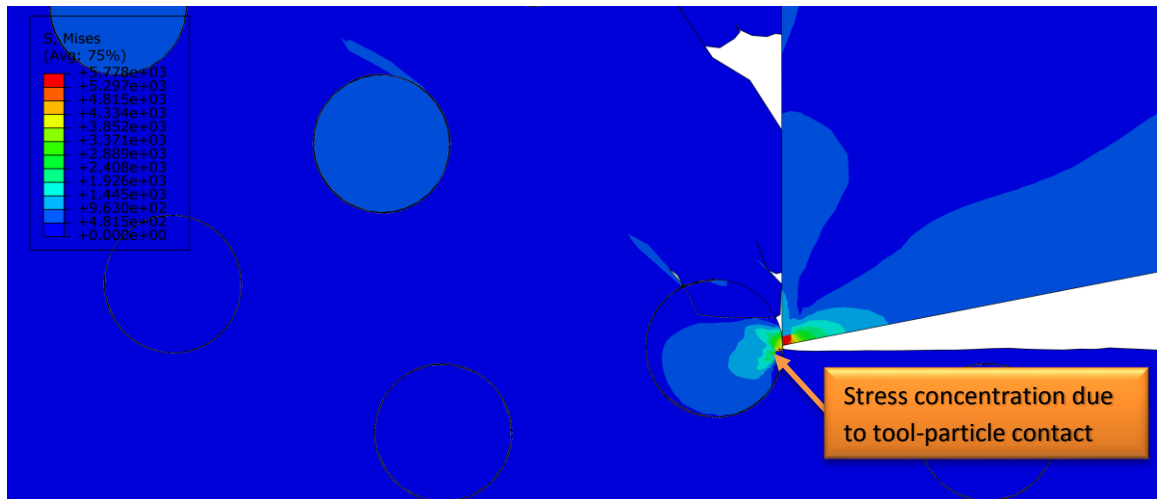


Figure 4.18 Evolution of crack due to interaction between cutting tool and particle located below the cutting line: initiation of interaction (Unit: MPa) (Al 6061/20% 23  $\mu\text{m}$   $\text{Al}_2\text{O}_3$ ,  $v=60$  m/min, rake angle= $0^\circ$ , width of cut=1 mm)

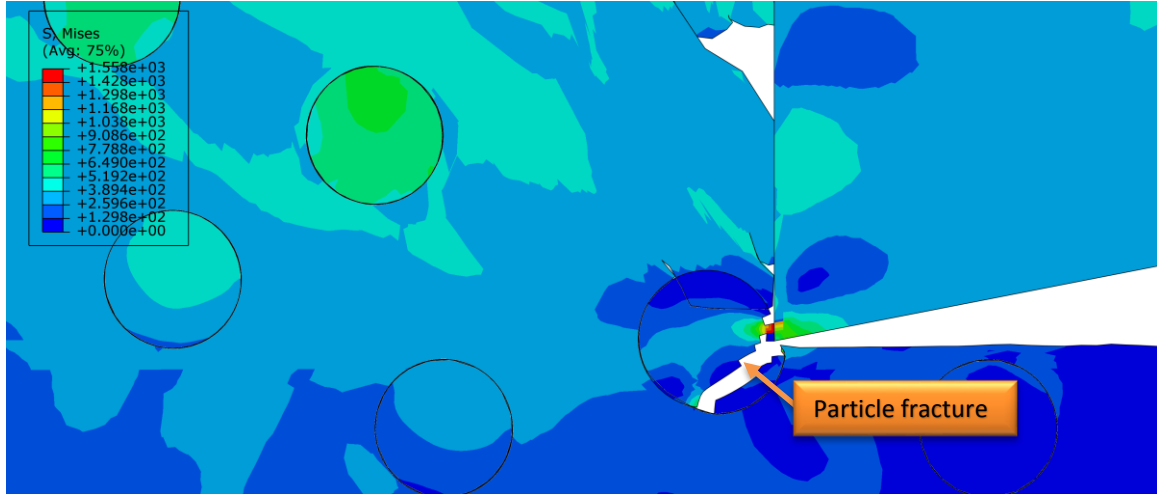


Figure 4.19 Evolution of crack due to interaction between cutting tool and particle located below the cutting line: evolution of crack in the particle (Unit: MPa) (Al 6061/20% 23  $\mu\text{m}$   $\text{Al}_2\text{O}_3$ ,  $v=60$  m/min, rake angle= $0^\circ$ , width of cut=1 mm)

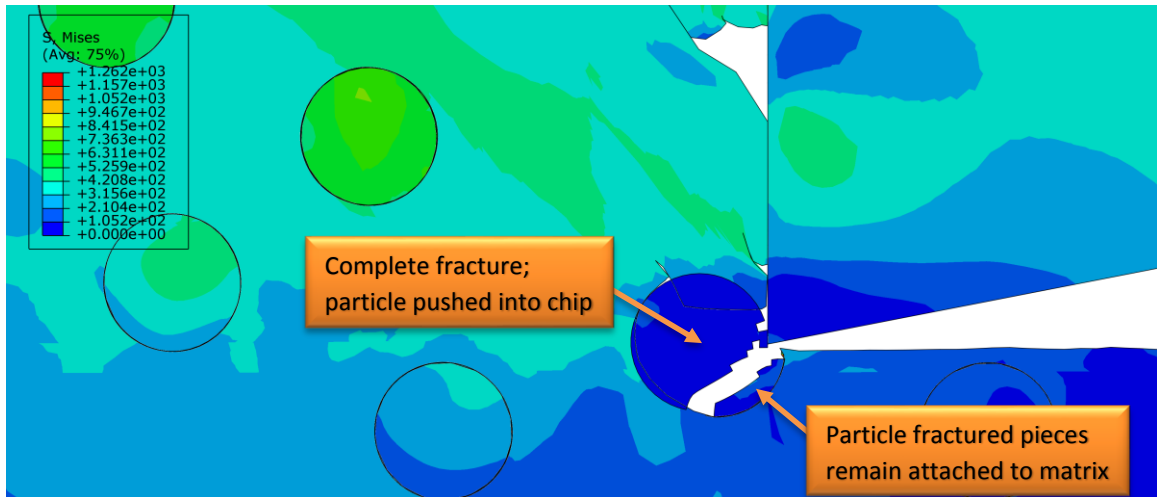


Figure 4.20 Evolution of crack due to interaction between cutting tool and particle located below the cutting line: complete fracture of particle (Unit: MPa) (Al 6061/20% 23  $\mu\text{m}$   $\text{Al}_2\text{O}_3$ ,  $v=60$  m/min, rake angle= $0^\circ$ , width of cut=1 mm)

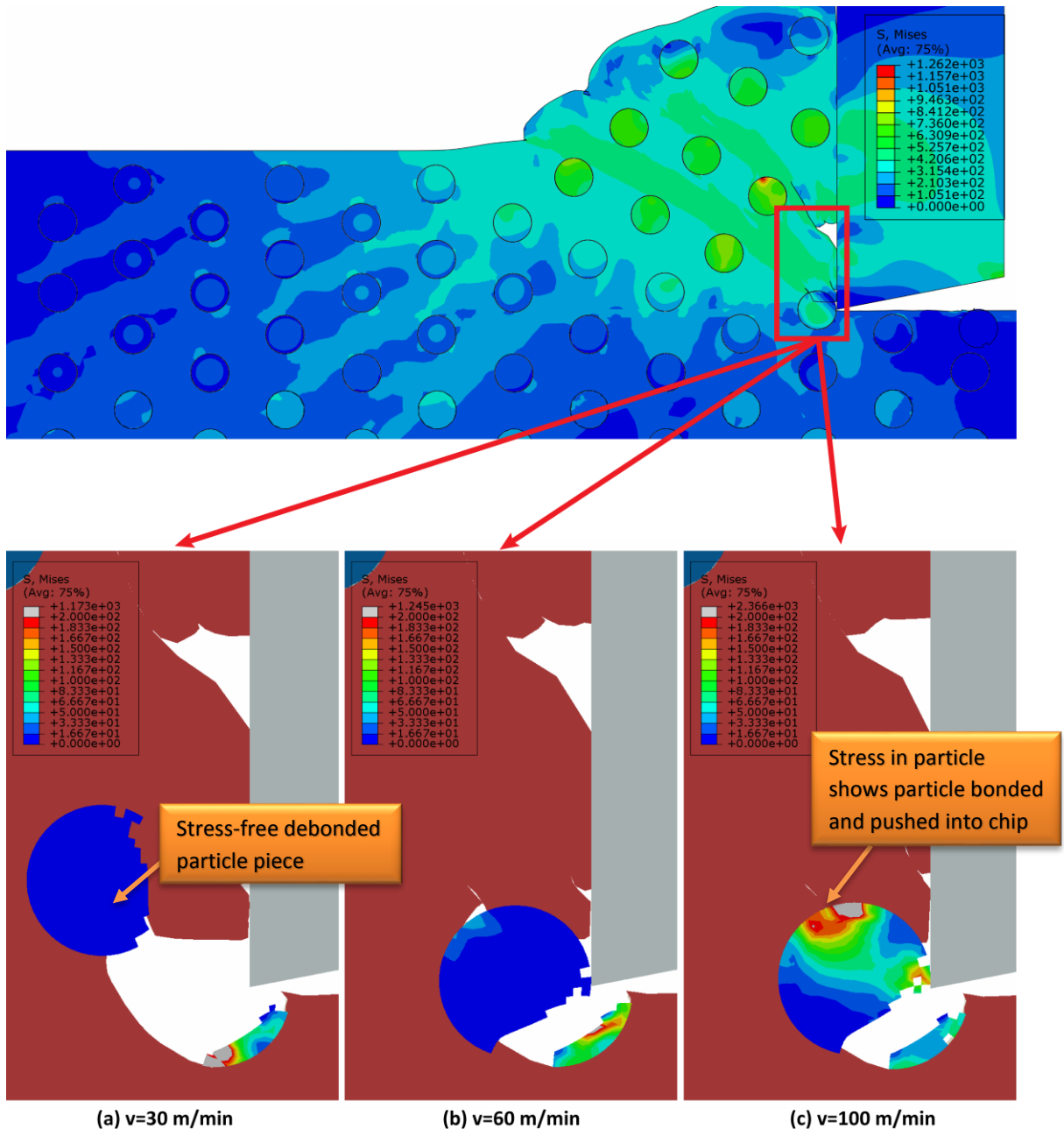
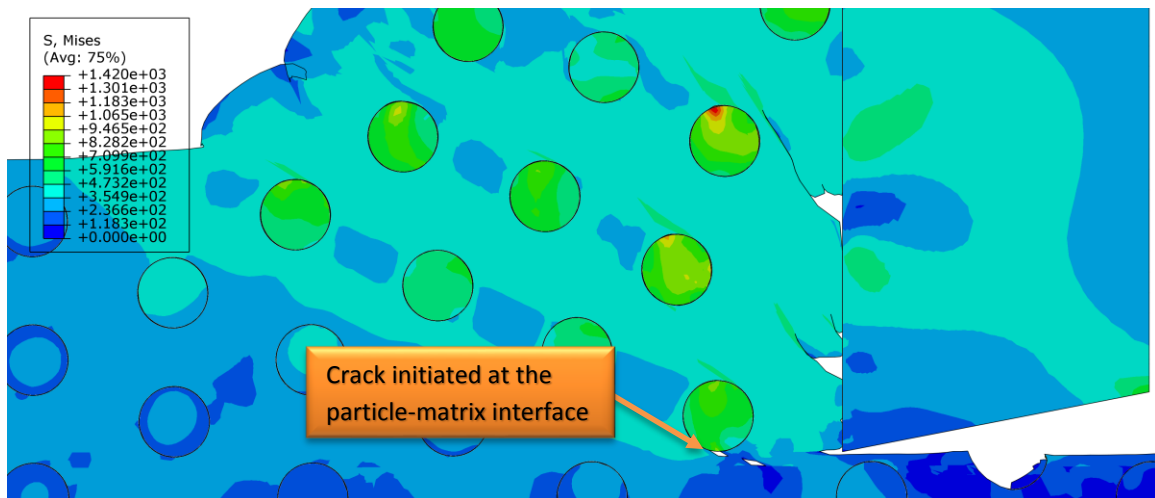


Figure 4.21 Stress (MPa) distribution during interaction in particles located below the cutting line (Al 6061/20%  $23 \mu\text{m}$   $\text{Al}_2\text{O}_3$ , rake angle= $0^\circ$ , width of cut=1 mm)

Figure 4.21 compares the interaction between the cutting tool and a particle located below the cutting line for different cutting speeds. It is shown in this figure that particle fracture occurs for all the three cutting speeds. However, the particle-matrix interface behaviour is not similar when using different cutting speeds. When machining with a

lower cutting speed, the interface is damaged more rapidly as compared to cutting with a higher cutting speed. For instance, when  $v=30$  m/min, the larger particle piece is completely debonded from the matrix; however when  $v=60$  m/min, the larger particle piece remains attached to the matrix and is pushed into the chip by the tool.

Figure 4.22 to Figure 4.25 show progressing frames of interaction between the cutting tool and a particle with the center above the cutting line. As depicted in Figure 4.22, this interaction causes initiation of crack at the particle-matrix interface. This happens before a direct contact between the cutting tool and particle occurs. Crack progresses into the matrix as the cutting tool advances (Figure 4.23). This progress leads to complete fracture in the matrix and formation of chip (Figure 4.24). In this interaction, the particle remains bonded to the matrix and is pushed into the chip (Figure 4.25). Figure 4.25 also shows that because of the fracture in the matrix ahead of the cutting tool, machined surface roughness will be slightly increased.



**Figure 4.22** Interaction between cutting insert and particle located above the cutting line; initiation of crack (Unit: MPa) (Al 6061/20% 23  $\mu\text{m}$   $\text{Al}_2\text{O}_3$ ,  $v=60$  m/min, rake angle= $0^\circ$ , width of cut=1 mm)

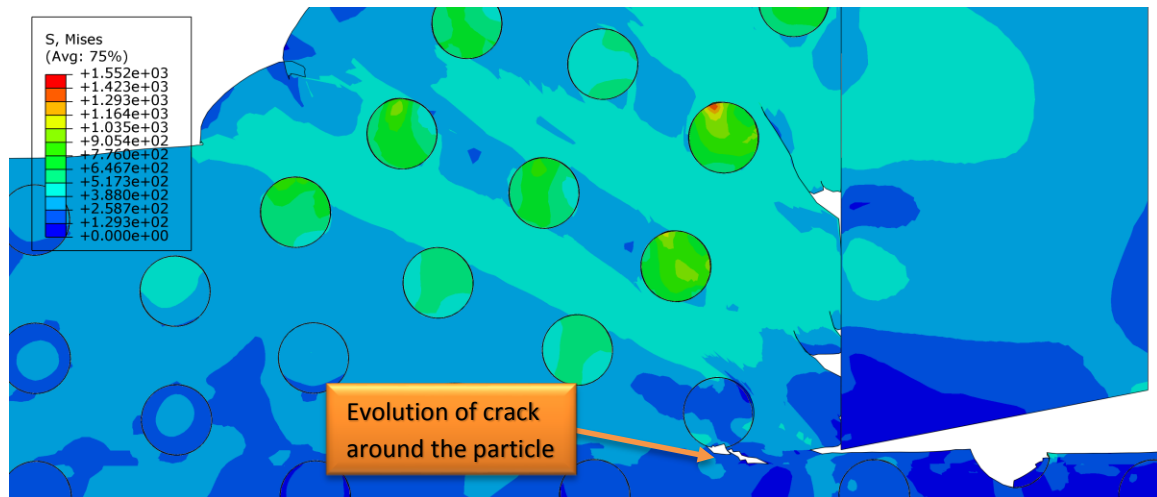


Figure 4.23 Interaction between cutting insert and particle located above the cutting line; evolution of crack (Unit: MPa) (Al 6061/20% 23  $\mu\text{m}$   $\text{Al}_2\text{O}_3$ ,  $v=60$  m/min, rake angle= $0^\circ$ , width of cut=1 mm)

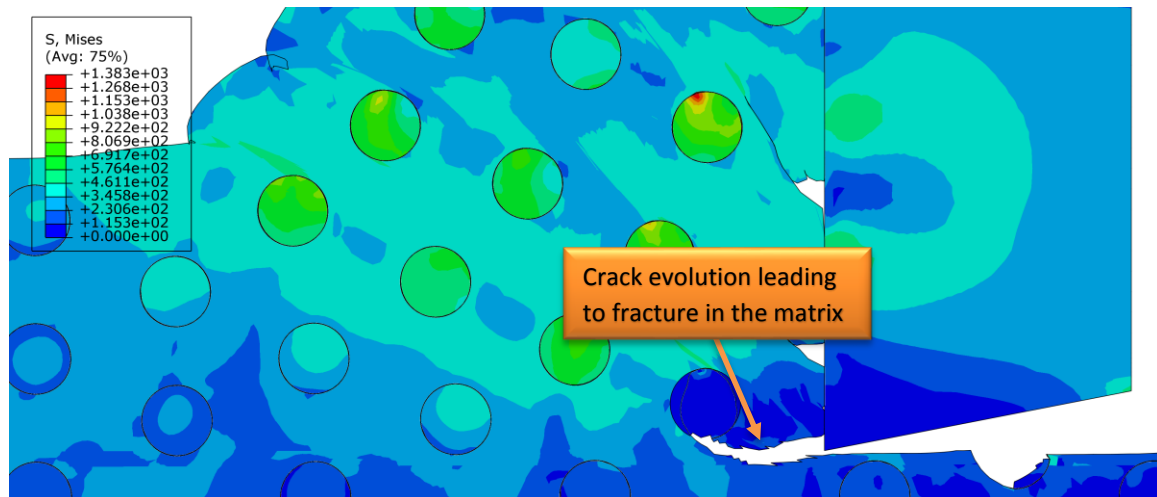
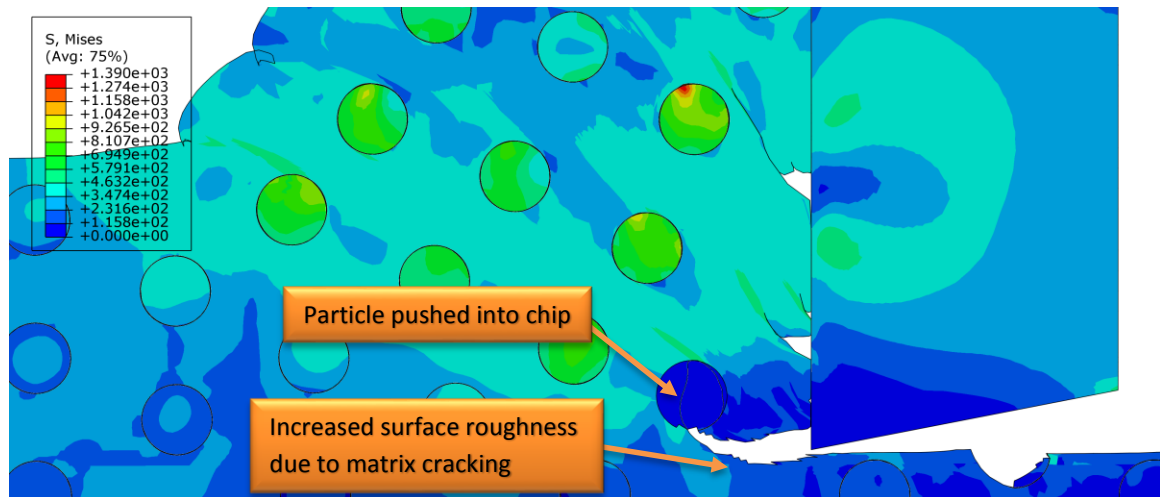


Figure 4.24 Interaction between cutting insert and particle located above the cutting line; complete cracking (Unit: MPa) (Al 6061/20% 23  $\mu\text{m}$   $\text{Al}_2\text{O}_3$ ,  $v=60$  m/min, rake angle= $0^\circ$ , width of cut=1 mm)



**Figure 4.25 Interaction between cutting insert and particle located above the cutting line; particle pushed into chip (Unit: MPa) (Al 6061/20% 23  $\mu\text{m}$   $\text{Al}_2\text{O}_3$ ,  $v=60$  m/min, rake angle= $0^\circ$ , width of cut=1 mm)**

In Figure 4.26, the interaction between cutting tool and particle located above the cutting line is compared for different cutting speeds. This figure shows that the change in cutting speed can modify the effect of interaction on reinforcement debonding and fracture. For the cutting speeds of  $v=30$  m/min and  $v=60$  m/min, cracking starts ahead of the tool at the particle-matrix interface and then progresses into the matrix. However, when machining using  $v=100$  m/min, cracking starts in the matrix at the tool-matrix contact region. This clearly demonstrates the effect of cutting speed on the mechanics of chip formation during machining MMCs. When using lower cutting speeds, chip is formed as a results of evolution of cracks initiating from the particle-matrix interface. Since these cracks are created ahead of the cutting tool, their progress in the matrix can adversely affect the machined surface quality.

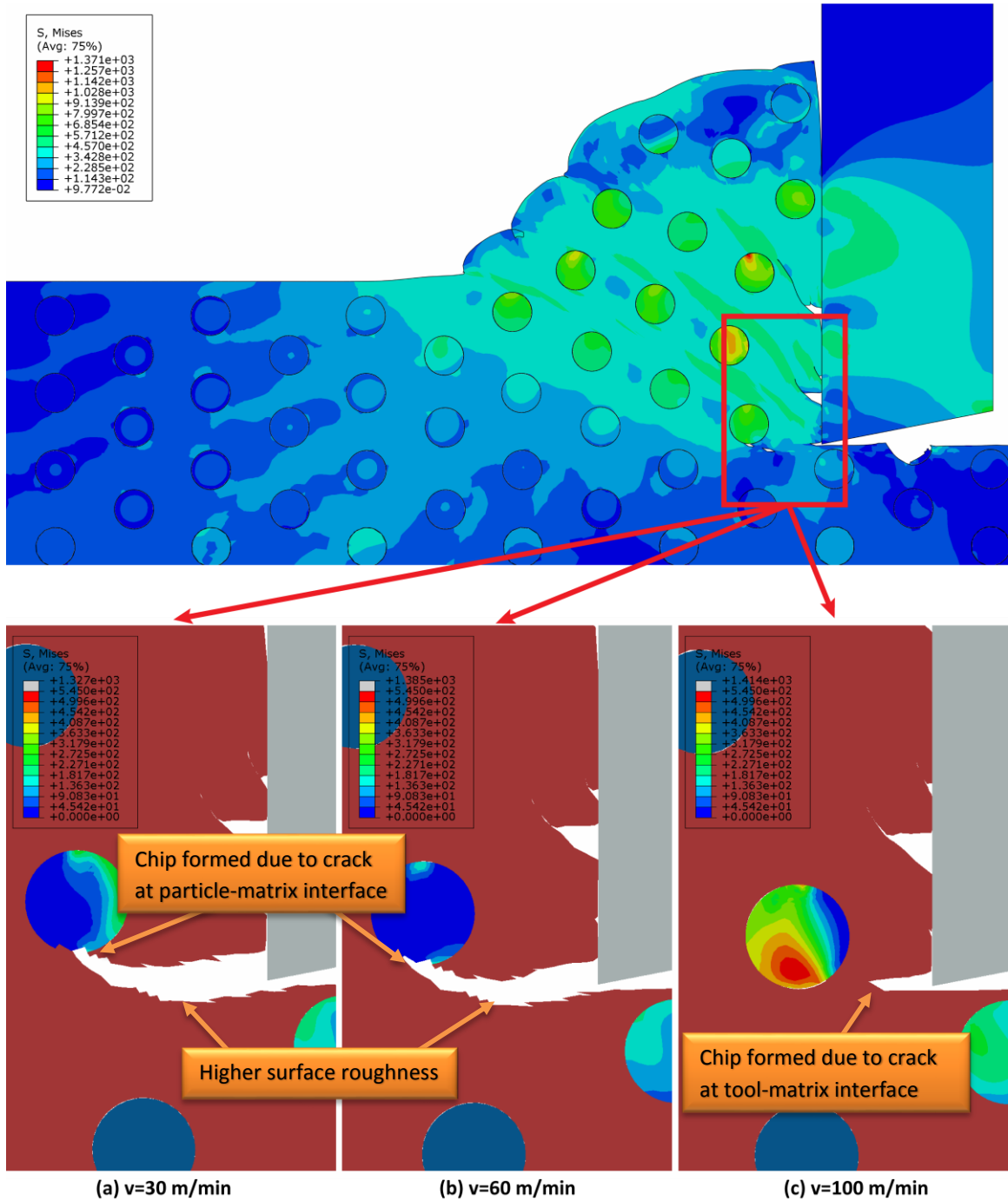


Figure 4.26 Stress (MPa) distribution during interaction in particles located above the cutting line (Al 6061/20% 23  $\mu$ m  $Al_2O_3$ , rake angle=0°, width of cut=1 mm)

c. *Analysis of the effect of cutting speed on temperature:* Finite element analysis can provide valuable information regarding the temperature distribution during metal cutting and how it is affected by the cutting speed. Figure 4.27 compares the temperature distribution in the chip area during cutting with different speeds. An increase in the temperature with an increase in cutting speed is apparent in this figure. This increase in temperature softens the matrix material, which will in turn result in a decrease in cutting forces as the cutting speed increases, as shown in Figure 4.14.

Figure 4.27 also shows that the area in the chip with maximum temperature exists on the tool rake face away from the tool tip. Such occurrence has been reported in the metal cutting literature [119]. Existence of such high temperature at this point results in formation of crater wear in this region of the tool face, which in turn alters the effective rake angle.

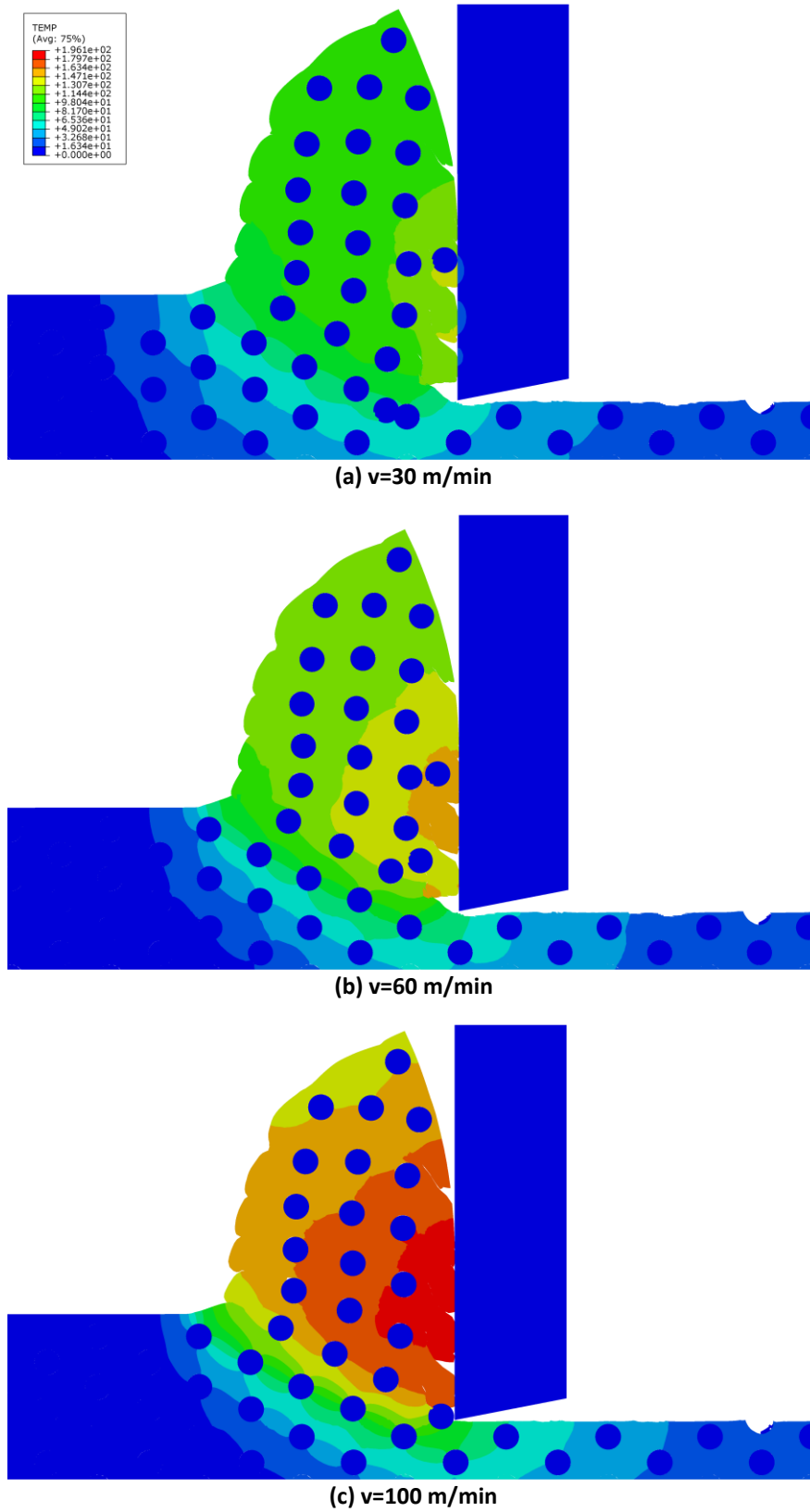


Figure 4.27 Temperature ( $^{\circ}\text{C}$ ) distribution during cutting MMC with different cutting speeds (Al 6061/20%  $23\ \mu\text{m}\ \text{Al}_2\text{O}_3$ , rake angle= $0^{\circ}$ , width of cut=1 mm)

d. *Analysis of the effect of cutting speed on stress:* Analysis of the stress in the workpiece material during machining is an important step in studying the material behavior during the cutting process. The FE model is utilized for investigating the effect of cutting speed on stress distribution during MMC machining. Figure 4.28 shows the distribution of stress in the matrix phase of MMC during machining with different cutting speeds. These stress distributions are captured at a single time frame. As expected in a metal cutting operation, the areas with large stress are located in the primary and secondary shear zones. However, because of existence of reinforcements in the MMC, the stress distribution is slightly altered; the maximum stress during MMC cutting is seen close to the cracks around the particles. This is different from machining monolithic materials, where the maximum stress occurs in the primary shear zone. This observation can be attributed to the stress concentration around the cracks at the particle-matrix interface in MMCs.

Figure 4.28 also shows a decrease in the level of stress in the shear zones with an increase of the cutting speed. An increase in cutting speed results in higher strain rate and higher temperature in the material. Both of these factors result in a reduction in matrix material strength and lower stress and cutting forces.

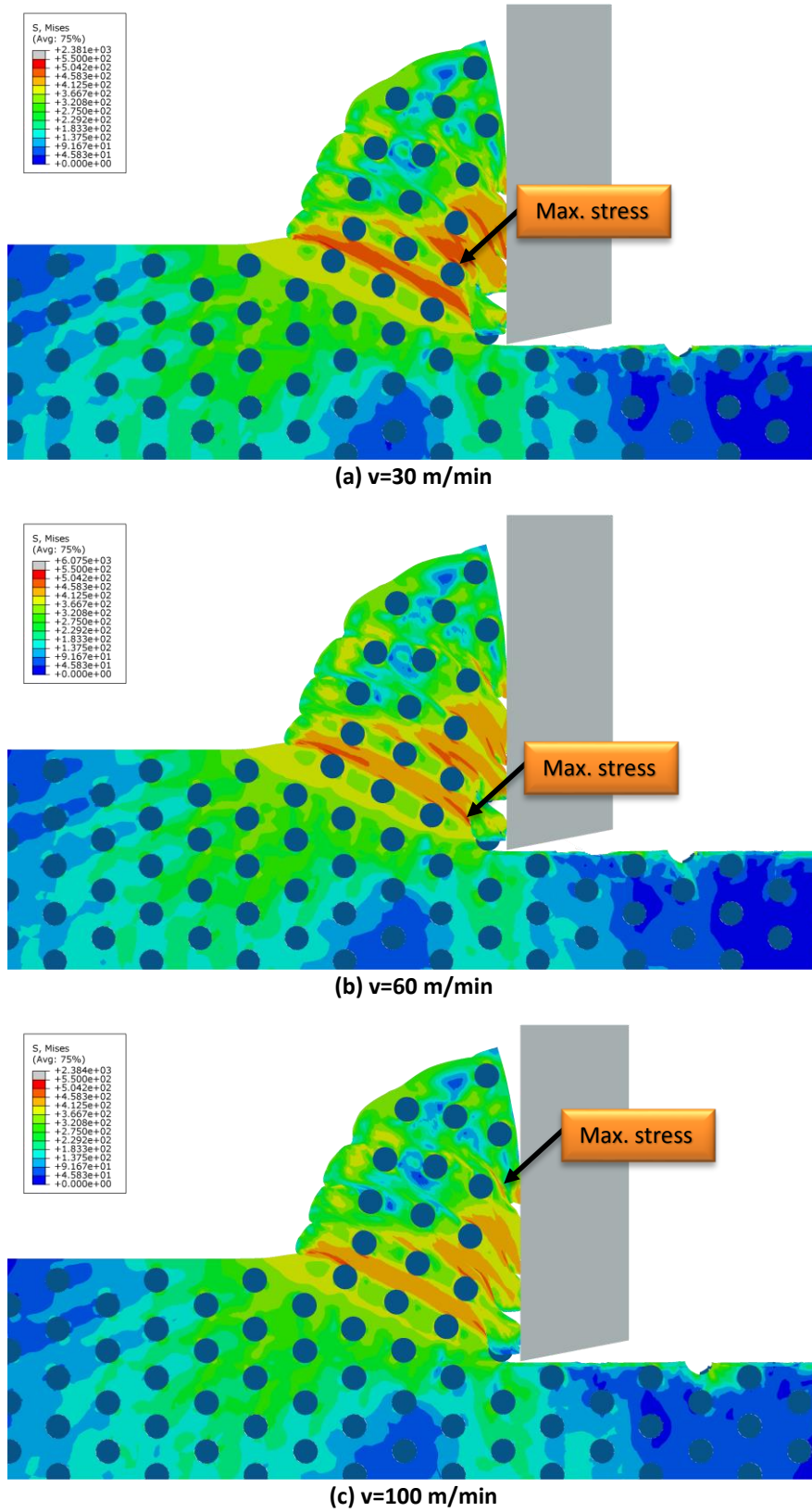
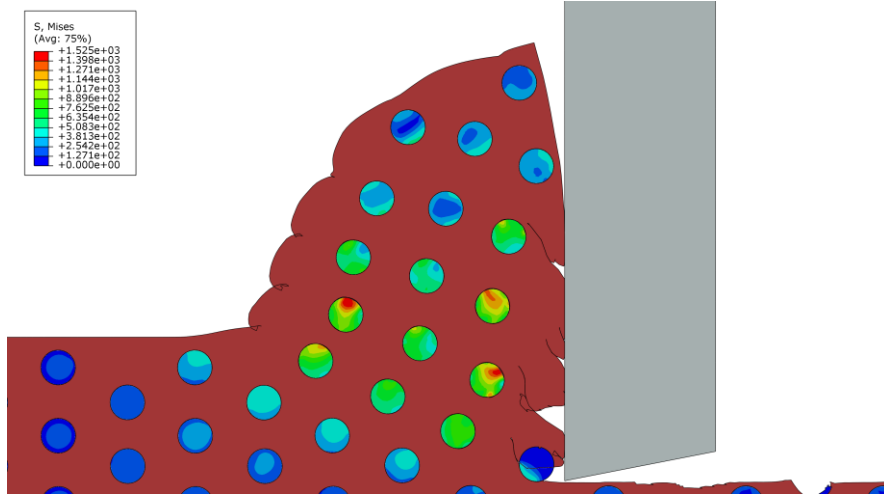


Figure 4.28 Distribution of stress (MPa) in the matrix during cutting MMC with different cutting speeds (Al 6061/20% 23  $\mu\text{m}$   $\text{Al}_2\text{O}_3$ , rake angle=0°, width of cut=1 mm)

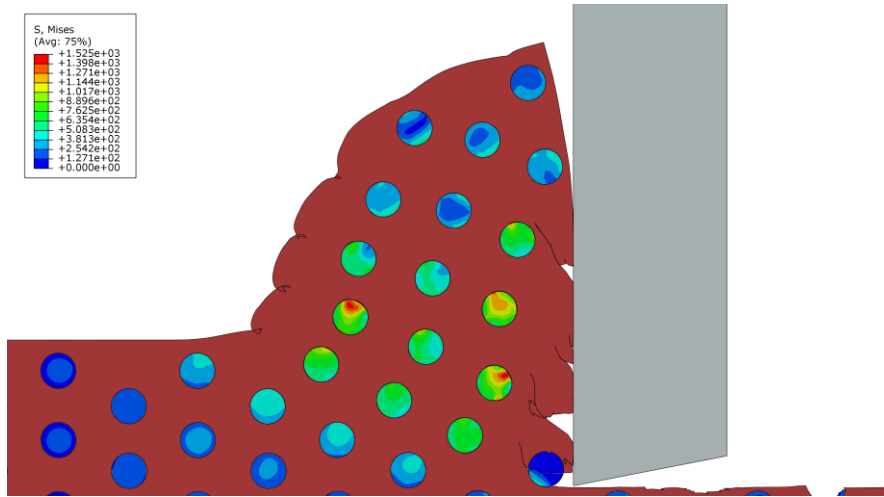
Stress distribution in the particulate reinforcements during machining is presented in Figure 4.29 for different cutting speeds. This figure shows concentration of stress in the particles in the primary shear zone. This stress concentration can result in cracking and breakage of particles during cutting.

Figure 4.29 also shows a decrease in the particle stress with the increase of cutting speed. As mentioned earlier, this decrease, which is consistent with the decrease in stress in the matrix, is a result of matrix material softening which is caused by higher strain rate and temperature.

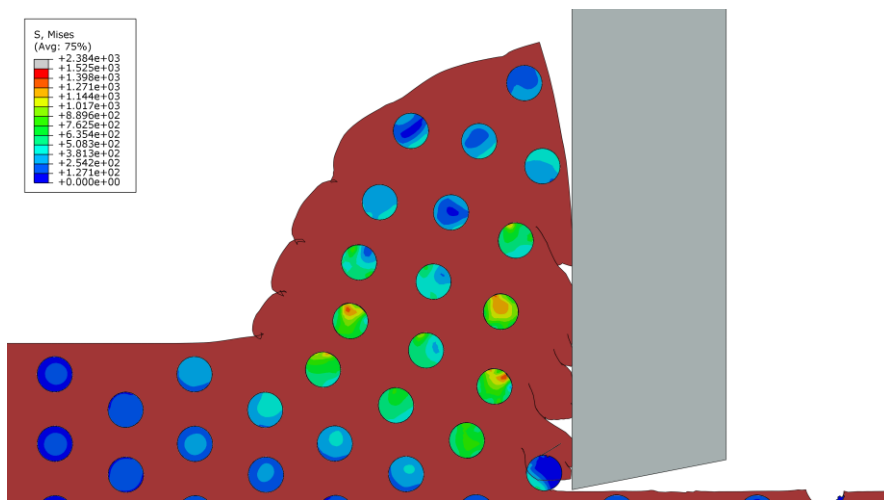
Figure 4.30 illustrates the Johnson-Cook damage parameter beneath the machined surface along the cutting path during machining with different cutting speeds. The maximum value of 1.0 for this damage parameter is a sign of complete failure. It is evident in this figure at most points, as the cutting speed is increased, the damage beneath the surface decreases. This observation can be explained by considering the parameters affecting the ductile damage, as described in equations (2-13) and (2-14). According to these equations, increasing temperature and strain rate result in a higher value of strain to fracture. Thus, with similar strain conditions, the damage parameter, which is defined as strain divided by strain to fracture, will be smaller when temperature and strain rate are increased. Therefore, higher cutting speed results in lower damage beneath the machined surface.



(a) v=30 m/min



(b) v=60 m/min



(c) v=100 m/min

Figure 4.29 Distribution of stress (MPa) in particles during cutting MMC with different cutting speeds (Al 6061/20% 23  $\mu\text{m}$   $\text{Al}_2\text{O}_3$ , rake angle=0°, width of cut=1 mm)

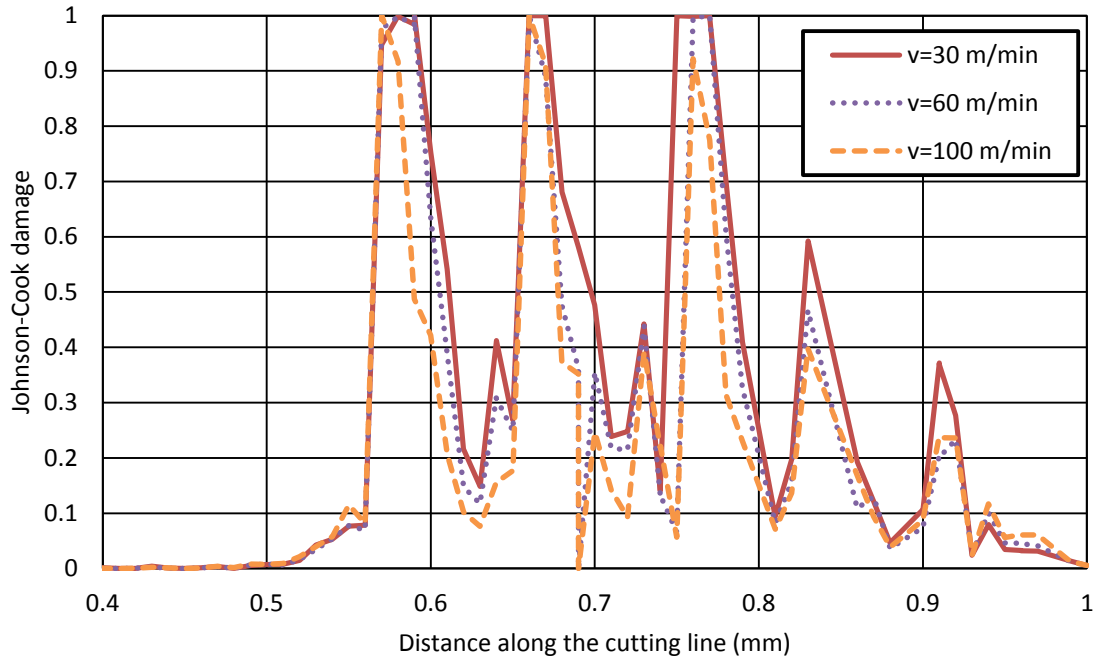


**Figure 4.30** Damage beneath the machined surface along the cutting line for various cutting speeds (Al 6061/20% 23  $\mu\text{m}$   $\text{Al}_2\text{O}_3$ , rake angle=0°, width of cut=1 mm)

The FE model presented in this section was utilized for studying MMC machining using various cutting speeds. Due to the comprehensive nature of the developed FE model, i.e. simulation of all phases of MMC during cutting using the finite element method, the model was successful in providing a complete understanding of MMC behavior and tool-reinforcement interactions when machining using different cutting speeds.

**4.5.3 Model III, analysis of plastic deformation:** Plastic deformations in the workpiece material are a major factor contributing to the variation of the behavior of MMCs during machining. The ductile matrix in MMCs will undergo severe plastic

deformations, particularly around the brittle reinforcements. These deformations will then cause different types of fracture and debonding in particles.

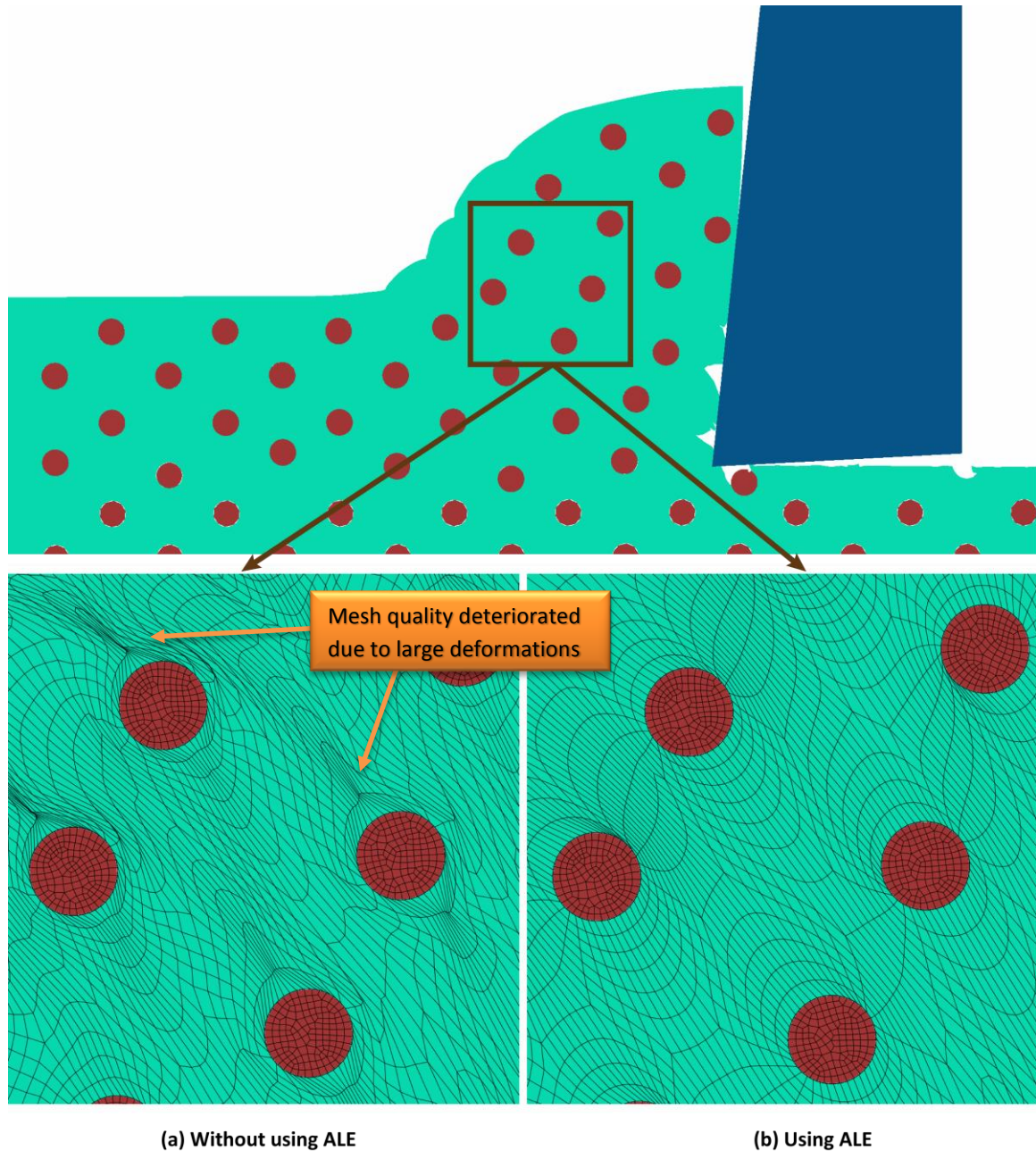


Figure 4.31 Analysis of the effect of using ALE adaptive meshing on mesh quality (Al 6061/10% 17  $\mu\text{m}$   $\text{Al}_2\text{O}_3$ ,  $v=60$  m/min, rake angle=6°, width of cut=1 mm)

As mentioned previously, the large deformations during the cutting process can lead to severe degradation of mesh quality in the chip area during finite element modeling using Lagrangian analysis. In order to overcome this obstacle, the ALE adaptive meshing technique is used in model III. Figure 4.31 shows the effect of using ALE technique on the mesh quality. Comparison of the two models depicted in this figure shows that using the ALE technique can immensely improve the mesh quality, especially around the particles. The ALE technique avoids a large increase in the element aspect ratios as a result of deformations during machining.

Plastic deformation in the matrix phase of MMC can be measured using equivalent plastic strain, as shown in Figure 4.32. This figure illustrates the unique shape of plastic deformations during MMC machining. Existence of reinforcements leads to non-uniform plastic strains in MMCs, which is different from the deformations observed in machining monolithic materials. Figure 4.32 depicts the zones of high deformation along the particles as well as the zones of low deformation between the particles. This figure also shows the high plastic strain in the matrix areas adjacent to the particles. The stress distribution in particles, shown in Figure 4.32, proves that the large plastic strains in the matrix results in high stress concentration in the particles, which can cause particle fracture.

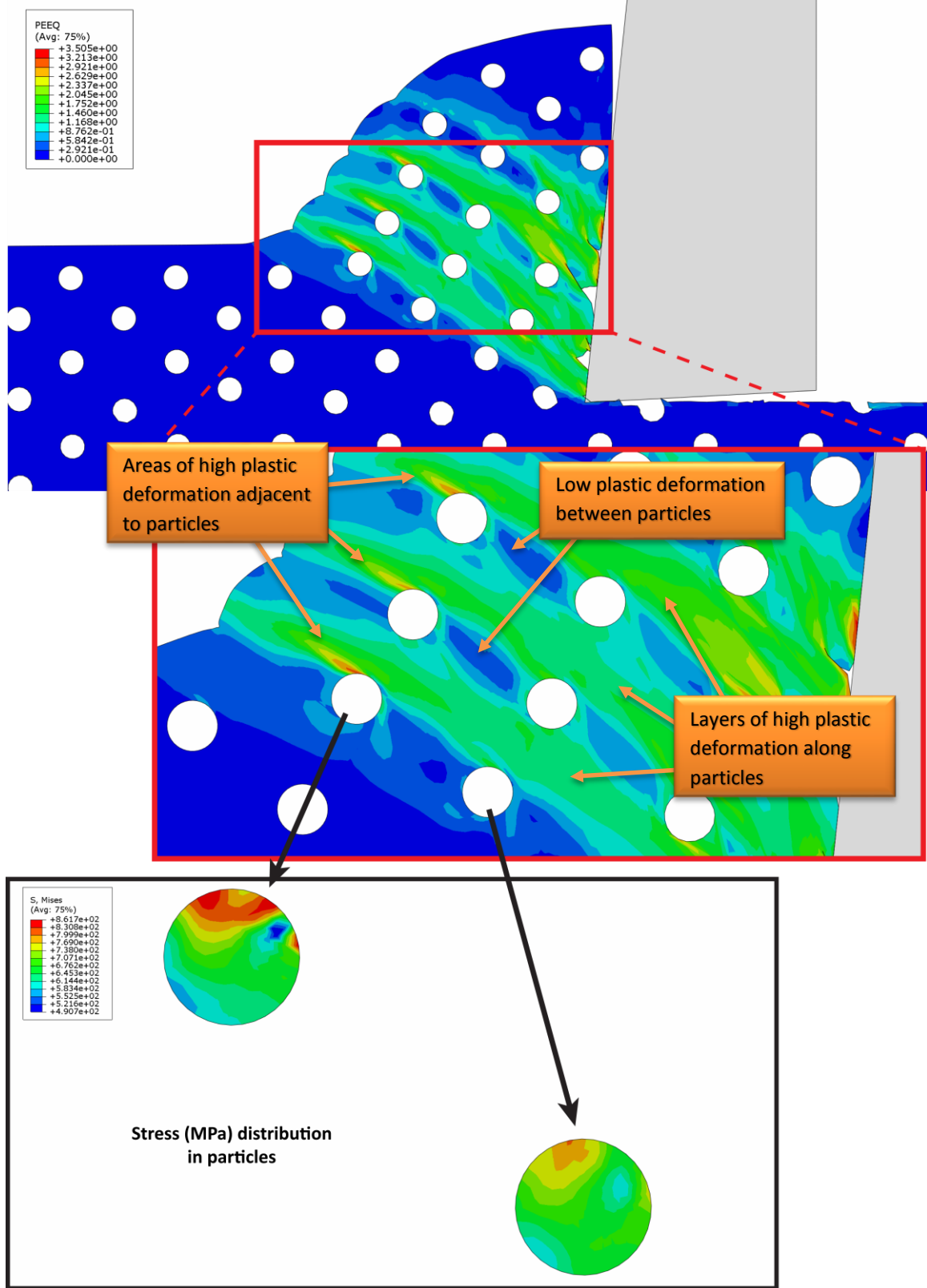


Figure 4.32 Equivalent plastic strain during MMC cutting (Al 6061/10% 17  $\mu\text{m}$   $\text{Al}_2\text{O}_3$ ,  $v=60$  m/min, rake angle= $6^\circ$ , width of cut=1 mm)

Figure 4.33 shows the plastic deformation beneath the machined surface. This plastic deformation is due to the interaction between the cutting tool and a particle along the cutting line. This interaction, which leads to particle debonding, causes a local increase in the plastic strain beneath the surface adjacent to particle cavity.

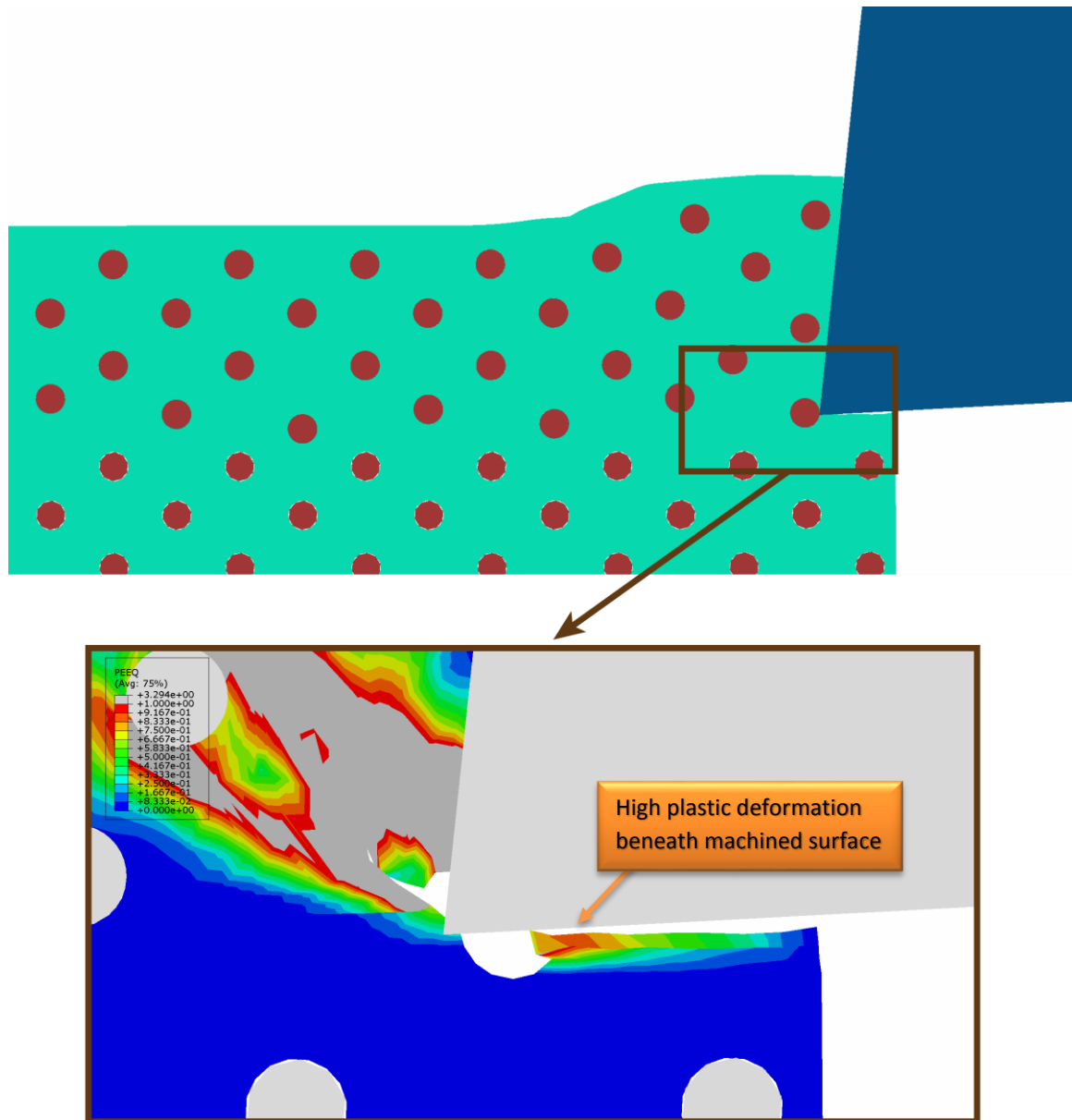
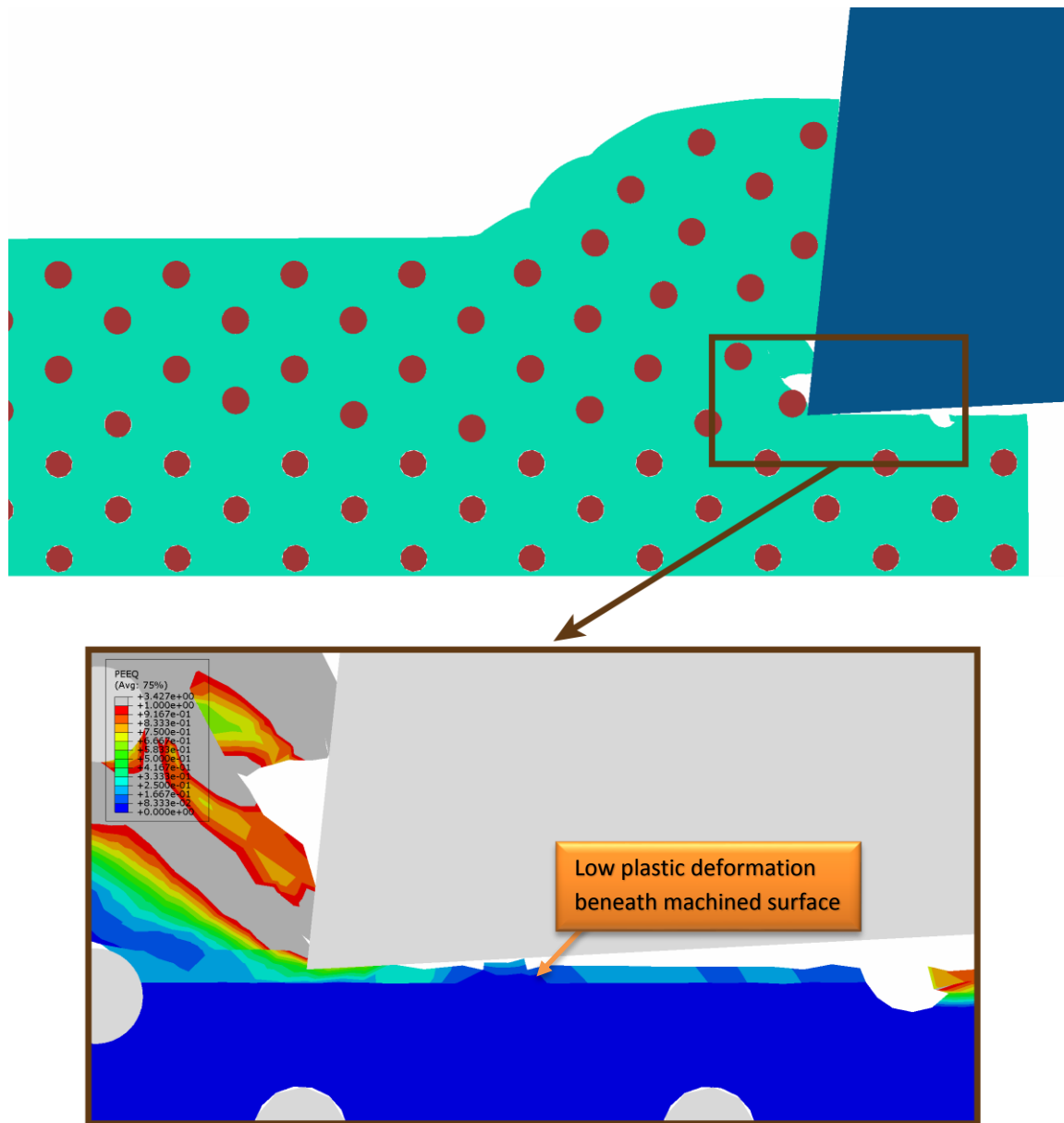


Figure 4.33 Equivalent plastic strain during interaction between cutting tool and a particle located on the cutting line (Al 6061/10% 17  $\mu\text{m}$   $\text{Al}_2\text{O}_3$ ,  $v=60$  m/min, rake angle=6°, width of cut=1 mm)



**Figure 4.34** Equivalent plastic strain during interaction between cutting tool and a particle located above the cutting line (Al 6061/10% 17  $\mu\text{m}$   $\text{Al}_2\text{O}_3$ ,  $v=60$  m/min, rake angle= $6^\circ$ , width of cut=1 mm)

In Figure 4.34, the plastic deformation beneath the surface due to interaction between the tool and a particle located above the cutting line is depicted. This figure proves that because of the particle, the plastic strain beneath the surface is very low; this strain is even lower than the areas where there is no tool-particle interaction. The reason for this observation is that in this area, chip is formed through debonding of particle,

which causes minimal plastic deformation beneath the surface. This is different from the areas with no tool-particle interaction, where chip is formed due to separation of the matrix.

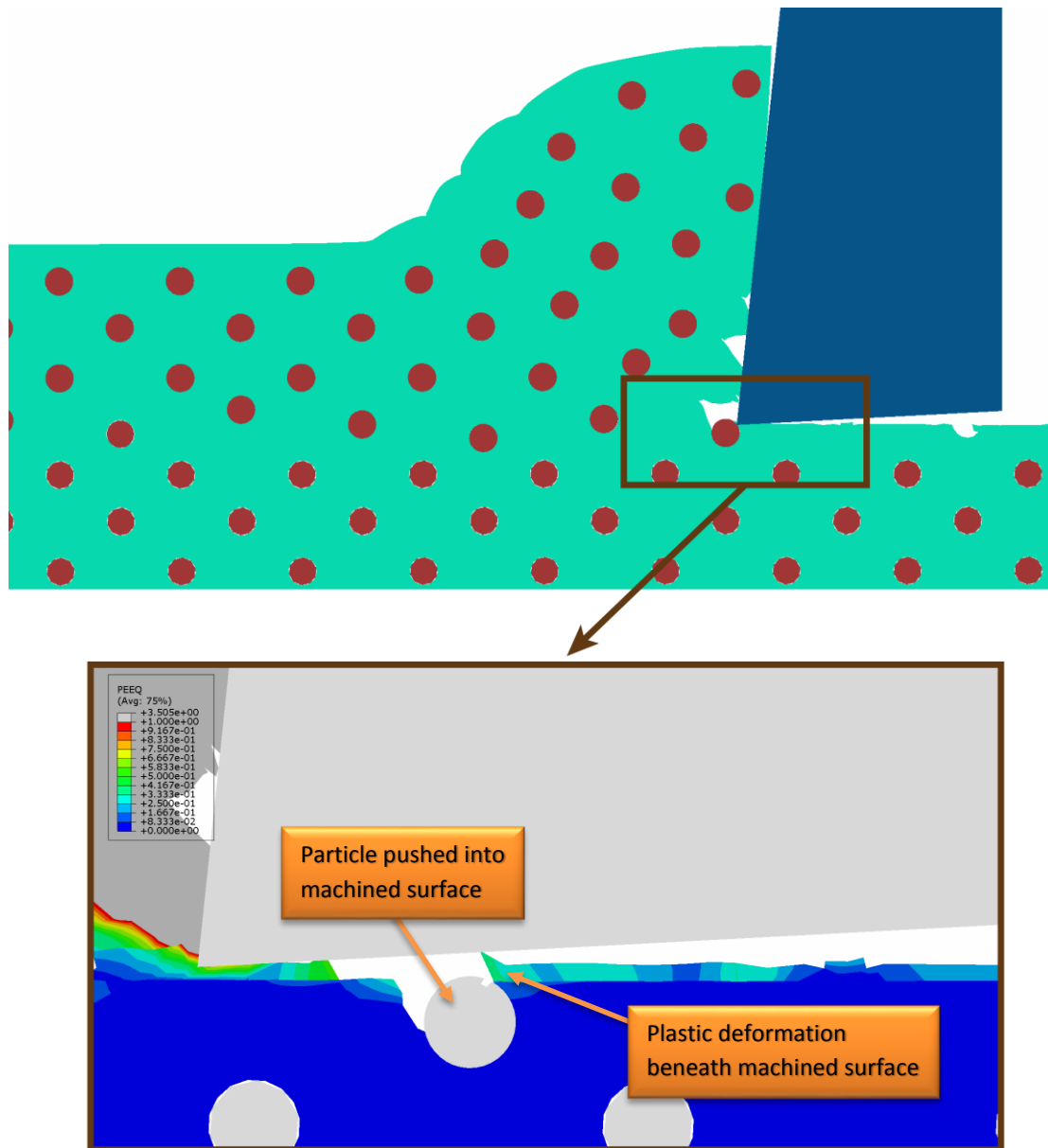


Figure 4.35 Equivalent plastic strain during interaction between cutting tool and a particle located below the cutting line (Al 6061/10% 17  $\mu\text{m}$   $\text{Al}_2\text{O}_3$ ,  $v=60$  m/min, rake angle= $6^\circ$ , width of cut=1 mm)

Figure 4.35 illustrates the plastic deformation beneath the surface in the interaction between tool and a particle located below the cutting line. Here, the cutting tool pushes the particle into the machined surface. The plastic deformation observed in this case is not as large as the one seen in the first interaction (between cutting tool and particle located on the cutting line).

#### **4.6 Closing remarks**

Details of finite element modeling of machining particle-reinforced MMCs were presented in this chapter. The finite element models were utilized for analysis of various unique aspects of MMC machining. The developed FE models simulated the main phases of a real MMC workpiece, namely the matrix phase, the particle phase, and the matrix-particle interface. Thus, the developed models were successful in providing an accurate description of the MMC behavior during the cutting process along with all the interactions between the particles, the matrix, and the cutting tool. This achievement differentiates the developed models from the previously developed FE models for MMC machining. In the next chapter, details of analytical modeling for studying the MMC machining process will be presented.

# Chapter 5 Analytical Model for Cutting Force

## 5.1 Introduction

The mechanistic models for simulation of cutting force are developed based on the single shear plane model for the cutting process. The assumptions that are used in these models are far from reality and thus, mechanistic models lack the ability to provide an accurate estimation of the cutting forces [61, 72]. On the other hand, models for calculation of cutting force that are developed based on the consumption of energy in different parts of the cutting system can provide a more comprehensive analysis of the cutting process and a more accurate estimation of the cutting force. An example of these models is the work by Kishawy et al. [75] for prediction of the cutting forces during the broaching operation. In this section, a novel model for prediction of cutting force during machining MMCs based the energy consumption in the cutting system is proposed. This model uses a conventional constitutive equation which has been used by researchers for modeling material behavior during machining.

## 5.2 Modeling cutting force based on partition of energy

**5.2.1 Energy partition of cutting system:** According to Astakhov and Xiao [74], the total power consumption in the cutting system for a monolithic material is the sum of power consumption for plastic deformation, power spent at the tool-chip interface, power spent at the tool-workpiece interface, power required for formation of new surfaces, and the power spent due to the effect of the minor cutting edge. During MMC machining, debonding of reinforcements leads to addition of an extra term to the total power consumption of the cutting system. Therefore, the total power consumption in the MMC cutting system,  $P_c$ , can be written as:

$$P_c = P_{pd} + P_{tc} + P_{tw} + P_{fns} + P_{mnc} + P_{deb} \quad (5-1)$$

where  $P_{pd}$  is the power required for plastic deformation,  $P_{tc}$  is the power consumption at tool-chip interface, and  $P_{tw}$  is the power consumption at tool-workpiece interface.  $P_{fns}$  and  $P_{mnc}$  are the power for formation of new surfaces and the power due to minor cutting edge, respectively.  $P_{deb}$  denotes the power required for debonding of particles during cutting MMCs. Therefore, the cutting force,  $F_c$ , can be calculated as:

$$F_c = \frac{P_c}{v} \quad (5-2)$$

where  $v$  is the cutting velocity.

In the next parts, each of the power components for the MMC machining system will be calculated. It should be noted that the power required for formation of new

surfaces is considered to be negligible in this research as its effect is shown to be minimal in experiments with low to medium cutting speeds [74].

**5.2.2 Power for plastic deformation:** Strain energy density can be used for calculation of the power required for plastic deformation of material layer being removed.

Using this concept, the required power can be calculated as:

$$P_{pd} = vA_c \int_0^{\epsilon} \sigma d\epsilon \quad (5-3)$$

Here,  $A_c$  is the area of the cross-section of the uncut chip and is obtained using the following equation:

$$A_c = d_c f \quad (5-4)$$

where  $d_c$  is the depth of cut and  $f$  is the feed rate.

Several equations exist in the literature for describing the constitutive behavior of the material. One of the most commonly used constitutive equations for modeling material behavior during processes that involve large strains, high strain rates, and high temperatures is presented by Johnson and Cook [80]. Since this model is proven to be able to provide an accurate simulation of material behavior during machining [120], it will be used in this section. Using equation (2-12), the power required for plastic deformation can be calculated as shown in equation (5-5).

$$P_{pd} = vA_c \left( A\epsilon + \frac{B}{n+1} \epsilon^{n+1} \right) \left[ 1 + C \ln \left( \frac{\dot{\epsilon}}{\dot{\epsilon}_0} \right) \right] \left[ 1 - \left( \frac{T - T_{\text{transition}}}{T_{\text{melt}} - T_{\text{transition}}} \right)^m \right] \quad (5-5)$$

The equivalent plastic strain,  $\epsilon$ , during machining can be obtained as a function of chip compression ratio [121]:

$$\epsilon = 1.15 \ln \zeta \quad (5-6)$$

where  $\zeta$  is the chip compression ratio and is defined as the ratio of the chip thickness to the uncut chip thickness.

**5.2.3 Power for friction at tool-chip interface:** Flow of the chip over the rake face of the cutting tool requires overcoming the friction between the MMC chip surface and the tool rake face.

a. *Tool-chip friction force*: The friction force at the tool-chip interface,  $F_f$ , is considered to be the sum of the friction at the tool-particle interface ( $F_{fP}$ ) and the friction at the tool-matrix interface ( $F_{fM}$ ):

$$F_f = F_{fP} + F_{fM} \quad (5-7)$$

b. *Tool-matrix interface*: The friction at the tool-matrix interface is similar to the friction between the tool and the chip produced during cutting a monolithic material. Thus, this friction force can be calculated as [74]:

$$F_{fM} = \tau_c l_c b_{1T} \quad (5-8)$$

where  $\tau_c$  is the average shear stress at the tool-chip contact,  $b_{1T}$  is the true chip width, and  $l_c$  is the tool-chip contact length. Equations (5-9) and (5-10) can be used for calculation of  $\tau_c$  and  $l_c$  [74].

$$\tau_c = 0.28\sigma_R \quad (5-9)$$

$$l_c = t_{1T}\zeta^{1.5} \quad (5-10)$$

Here,  $\sigma_R$  is the ultimate tensile strength of the matrix material and  $t_{1T}$  is the true uncut chip thickness. Astakhov [61] has provided equations for calculation of the true chip width ( $b_{1T}$ ) and uncut chip thickness ( $t_{1T}$ ) for various cutting geometries.

c. *Tool-particle interface*: The friction at the tool-particle interface is considered to be a combination of two-body abrasive friction and three-body rolling friction [81]. Particles in the MMC chip can get involved in abrasion of the cutting tool as long as they are attached to the matrix. When debonded from the chip, these hard particles can roll between the matrix and the cutting tool. Thus, the total friction force at tool-particle interface will be obtained by:

$$F_{fP} = F_{f-2body} + F_{f-3body} \quad (5-11)$$

where  $F_{f-2body}$  is the two-body abrasion friction and  $F_{f-3body}$  represents the three-body rolling friction.

The two-body friction force component (ploughing force component of friction) can be found as a function of tool material Vickers hardness,  $H_{tool}$ , and contact conditions [81]:

$$F_{f-2body} = N_p A_i H_{tool} t_{2body} \quad (5-12)$$

In equation (5-12),  $t_{2body}$  is the fraction of particles involved in two-body abrasion, which is assumed to be 40% for the type of MMC studied in this research. The same

assumption has been used by researchers in this field [81].  $N_p$  is the number of particles at the tool-chip interface and is obtained by:

$$N_p = \frac{V_f A_c}{\pi R^2} \quad (5-13)$$

where  $V_f$  and  $R$  are the volume fraction and average radius of particles, respectively.  $A_i$  is the contact area at the particle-tool interface and is given by:

$$A_i = \frac{R^2}{2} [2\theta_p - \sin(2\theta_p)] \quad (5-14)$$

Here,  $\theta_p$  is the angle of contact and is calculated as a function of groove depth,  $\delta_{p0}$ , using equation (5-15).

$$\theta_p = \cos^{-1} \left( 1 - \frac{\delta_{p0}}{R} \right) \quad (5-15)$$

As presented by Jiang et al. [122] when modeling two-body abrasive wear, the groove depth can be calculated by:

$$\delta_{p0} = \left( \frac{9\pi}{4} \right)^2 \left( \frac{H_{\text{tool}}}{3E^*} \right)^2 R \quad (5-16)$$

where  $E^*$  is the combined modulus and can be obtained as a function of tool and particle moduli of elasticity,  $E_1$  and  $E_2$ , and the Poisson's ratios,  $\nu_1$  and  $\nu_2$ , using:

$$\frac{1}{E^*} = \frac{(1 - \nu_1)^2}{E_1} + \frac{(1 - \nu_2)^2}{E_2} \quad (5-17)$$

Parameters used in these calculations are shown in Figure 5.1.

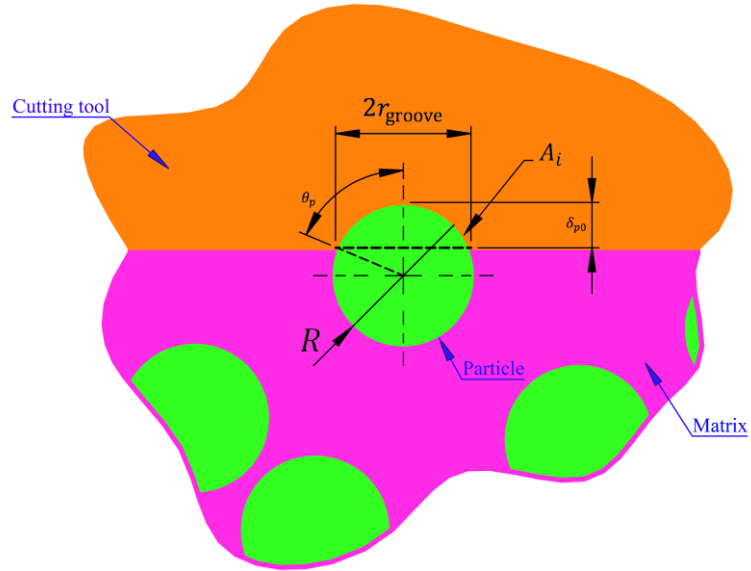


**Figure 5.1 Parameters of two-body abrasive contact between the particle and cutting tool**

The three-body rolling friction can be calculated using the three-body friction coefficient,  $\mu_{3\text{body}}$ , and the total normal force between particles and the tool rake face,  $F_N$ , using equation (5-18) [81].

$$F_{f-3\text{body}} = \mu_{3\text{body}} F_N \quad (5-18)$$

The total normal force can be calculated using the force exerted by one particle,  $F_{N_i}$ , and the number of particles at the tool-chip interface:

$$F_N = F_{N_i} N_p \quad (5-19)$$

The equation for calculation of the force exerted by an individual particle has been developed by Jiang et al. [122] in their two-body wear studies:

$$F_{N_i} = 0.967\pi R H_{\text{tool}} \delta_{p0} \quad (5-20)$$

Calculation of the three-body rolling friction coefficient has been presented by Goddard and Wilman [123]:

$$\mu_{3\text{body}} = \frac{s}{\pi p_m} \left( \frac{2R}{r_{\text{groove}}} \right)^2 \left\{ 1 - \left[ 1 - \left( \frac{r_{\text{groove}}}{R} \right)^2 \right]^{1/2} \right\} \quad (5-21)$$

where  $r_{\text{groove}}$  is equal to half of the groove width (as shown in Figure 5.1).  $s$  and  $p_m$  are the shear stress at the contact interface and maximum tool material flow stress, respectively. The ratio of  $s/p_m$  is assumed to be approximately equal to 1/6, as suggested by Sin et al. [124] in their abrasive wear studies.

**5.2.4 Power for friction at tool-workpiece interface:** The power consumption at the tool-workpiece interface during machining MMC is assumed to be equal to the power consumption at this interface during cutting a monolithic material. This assumption has been used by other researchers in the field [12]. Thus, the power dissipation due to friction at tool-workpiece interface can be calculated using the model provided by Astakhov and Xiao [74]:

$$P_{tw} = 0.625 \tau_y \rho_{ce} d_c \sqrt{\frac{Br}{\sin \alpha}} \quad (5-22)$$

In equation (5-22),  $\tau_y$  is the shear strength of the matrix material,  $\rho_{ce}$  is the cutting edge radius, and  $\alpha$  is the normal flank angle of the cutting tool.  $Br$  is the Briks similarity criterion and is defined as [61]:

$$Br = \frac{\cos \gamma}{\zeta - \sin \gamma} \quad (5-23)$$

where  $\gamma$  represents the normal rake angle of the cutting tool.

**5.2.5 Power due to effect of minor cutting edge:** The minor cutting edge can have a significant influence on the total power consumption of the cutting system. This effect mainly depends on the minor cutting edge angle,  $\kappa_{r1}$ . An ideal cutting edge with  $\kappa_{r1} = 90^\circ$  will have no minor cutting edge effect on the power consumption. However, when using real cutting inserts in everyday machining practice, the minor cutting edge effect should be considered. Through analysis of experimental results, researchers have provided factors for increase in the total power consumption as a result of minor cutting edge for various angles [74]. These factors are presented in Table 5.1.

**Table 5.1 Increase in power consumption due to the effect of minor cutting edge**

Minor cutting edge angle ( $\kappa_{r1}$ )	Increase in total power consumption
$30^\circ \leq \kappa_{r1} \leq 45^\circ$	14%
$15^\circ \leq \kappa_{r1} < 30^\circ$	17%
$10^\circ \leq \kappa_{r1} < 15^\circ$	20%
$\kappa_{r1} < 10^\circ$	23%

**5.2.6 Power for debonding of reinforcements:** The power dissipated as a result of debonding of the reinforcements during machining MMCs depends on the energy absorbed during failure of the bond of each particle and the probability of debonding of the reinforcement. Hence, the power for debonding can be obtained as the product of number of debonded particles and the energy required for debonding of each particle using equation (5-24).

$$P_{deb} = A_c v V_f P_{fr} \left( \frac{3}{4\pi R^3} \right) \Gamma \quad (5-24)$$

where  $P_{fr}$  is the probability of debonding of the reinforcement and  $\Gamma$  is the energy required for debonding of one particle.

According to Nicholson's work on the detachment of reinforcements from an elastic matrix [109], the energy required for failure of the unit area of bond between the reinforcement and the matrix can be calculated by:

$$u = \frac{9R\sigma^2}{4E_{mat}} \left[ \frac{(1 - \nu_{mat})^2}{1 + \nu_{mat}} \right] \quad (5-25)$$

where  $E_{mat}$  and  $\nu_{mat}$  are the matrix modulus of elasticity and Poisson's ratio, respectively. Thus, the energy absorbed during debonding of a particle,  $\Gamma$ , can be obtained as:

$$\Gamma = 4\pi R^2 u \quad (5-26)$$

Probability of debonding for particles in MMCs can be modeled using the weakest link model proposed by Weibull [125]. For spherical particles, the probability of debonding,  $P_{fr}$ , can be written as [104]:

$$P_{fr} = 1 - \exp \left[ - \frac{8R^3}{d_N^3} \left( \frac{\sigma}{\sigma_0} \right)^q \right] \quad (5-27)$$

In equation (5-27),  $q$  is the Weibull inhomogeneity factor and  $\sigma_0$  and  $d_N$  are normalizing constants.

The equations presented in this section can be used for calculation of various components of machining power. The flowchart for calculation of cutting force is presented in Figure 5.2.

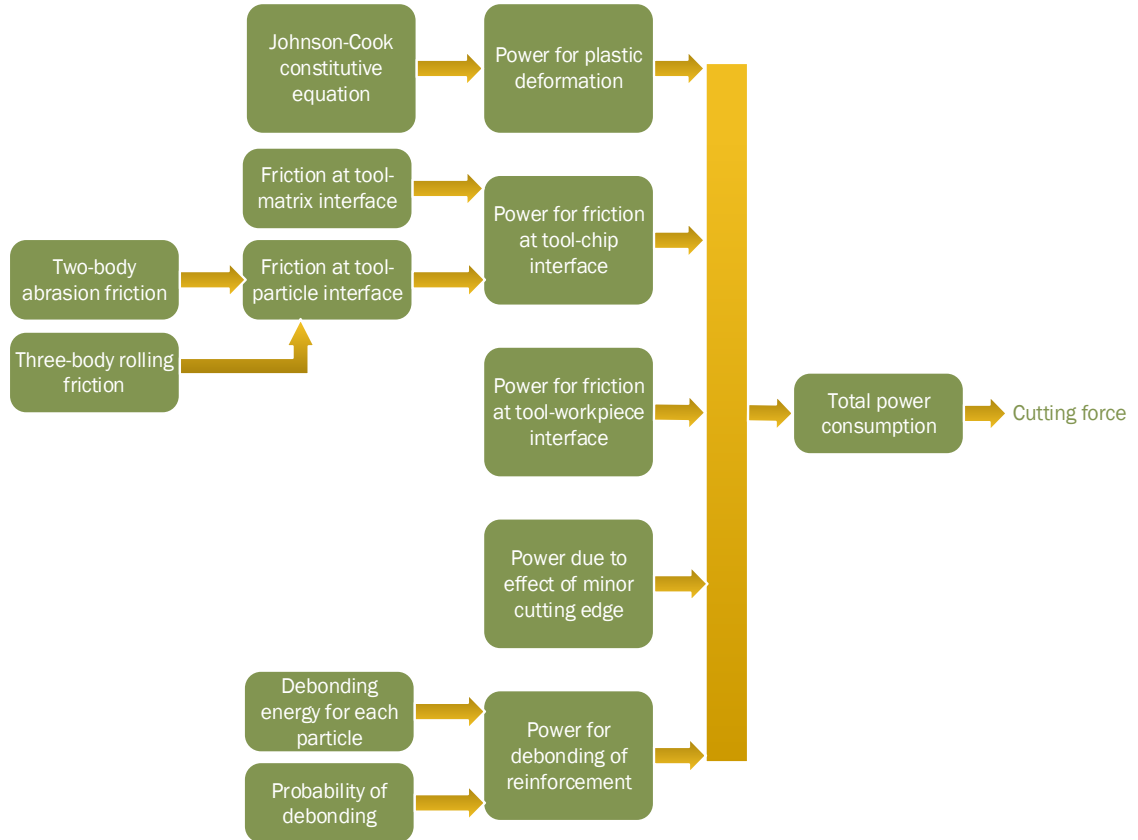


Figure 5.2 Flowchart for calculation of cutting force

### 5.3 Experimental verification of model results

Verification of the proposed force model is achieved through comparison of the model results with experimental data. Orthogonal cutting tests were performed on Al 6061/Al<sub>2</sub>O<sub>3</sub> and Al 7075/Al<sub>2</sub>O<sub>3</sub> particle reinforced MMCs. Two sets of tungsten carbide cutting inserts with 0° and 6° rake angles were used for turning experiments. Both sets of inserts have a flank angle of 11° and a minor cutting edge angle of 30°. Workpiece and tool material properties are listed in Table 5.2. Cutting test parameters are provided in Table 5.3.

**Table 5.2 Properties of the workpiece and tool materials**

Tool Vickers hardness [126]	23.5	
Tool modulus of elasticity (GPa) [126]	668.35	
Tool Poisson's ratio [126]	0.24	
Particle modulus of elasticity (GPa) [118]	416	
Particle Poisson's ratio [118]	0.231	
	Al 6061	Al 7075
Matrix ultimate tensile strength (MPa) [127]	310	572
Matrix shear strength (MPa) [127]	207	331
Matrix modulus of elasticity (GPa) [127]	68.9	71.7
Matrix Poisson's ratio [127]	0.33	0.33
Particle volume fraction (%)	10, 20	10, 15
Average particle diameter ( $\mu\text{m}$ )	9.5, 17, 20, 23, 25	15, 17
Johnson-Cook model parameters [117, 128]		
<i>A</i> (MPa)	324	496
<i>B</i> (MPa)	114	310
<i>C</i>	0.002	0.0
<i>n</i>	0.42	0.3
<i>m</i>	1.34	1.2
<i>T</i> <sub>melt</sub> (°C)	582	635
<i>T</i> <sub>transition</sub> (°C)	20	20
$\dot{\epsilon}_0$	1.0	1.0

**Table 5.3 Parameters of the cutting tests**

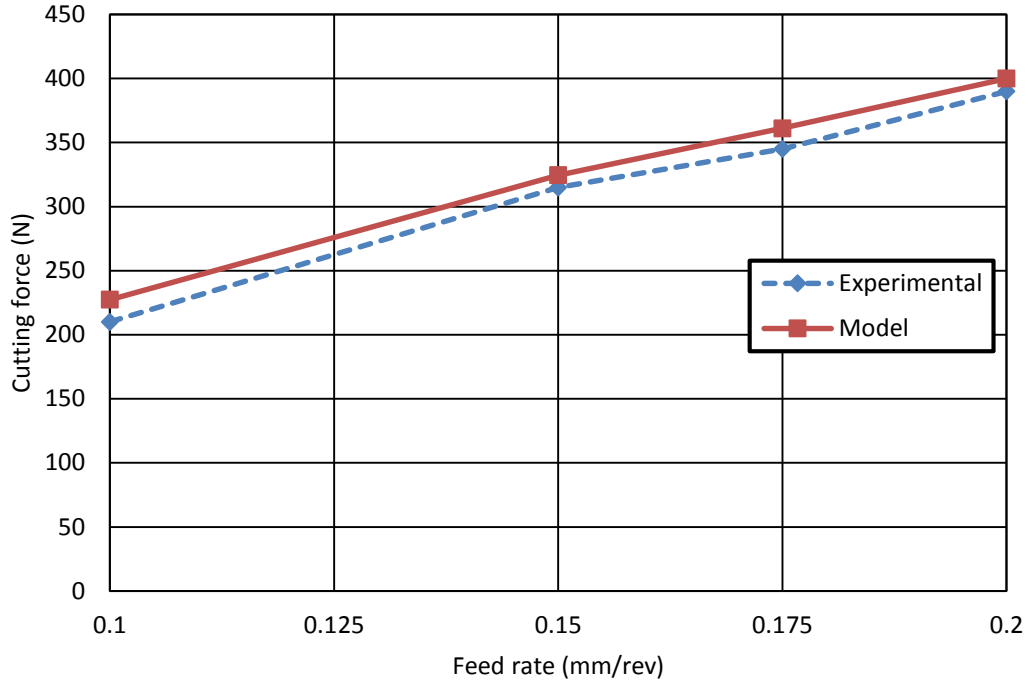
Feed rate (mm/rev)	0.1, 0.15, 0.175, 0.2
Cutting speed (m/min)	30, 60, 100
Depth of cut (mm)	3

## 5.4 Results and discussion

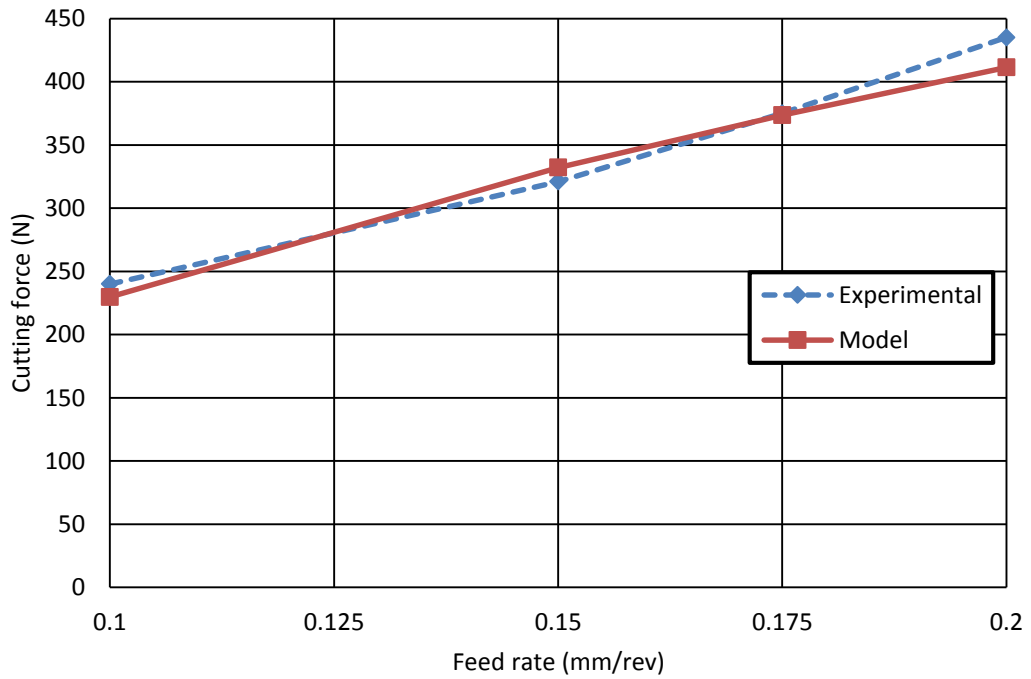
Experimental values for the cutting force are compared with the values obtained from the developed model as shown in Figure 5.3 and Figure 5.4. It is clear from these figures that model results are in very good agreement with the experimental data. The

maximum difference between the predicted cutting force and experimental value is 8.3%, which is only seen in one of the tests (Machining Al6061/10% 17  $\mu\text{m}$   $\text{Al}_2\text{O}_3$  with a feed rate of 0.1 mm/rev). In all other cutting tests, the deviation between predicted and measured results is less than 5%. This demonstrates the ability of the proposed force model to simulate the MMC machining process.

Power partition of MMC machining system is shown in Figure 5.5. As can be seen, the major power dissipation during machining is related to the plastic deformation of matrix material while the debonding of particles has the least influence on the total power consumption. Figure 5.5 also shows the increase in components of power consumption with an increase in feed rate. It should be noted that as the feed rate increases from 0.1 mm/rev to 0.15 mm/rev, all power components increase by around 40% except the power dissipation at the tool-workpiece interface, which displays an increase of only 1.5%. This observation is expected as the feed rate does not have a considerable influence on the tool-workpiece interface.

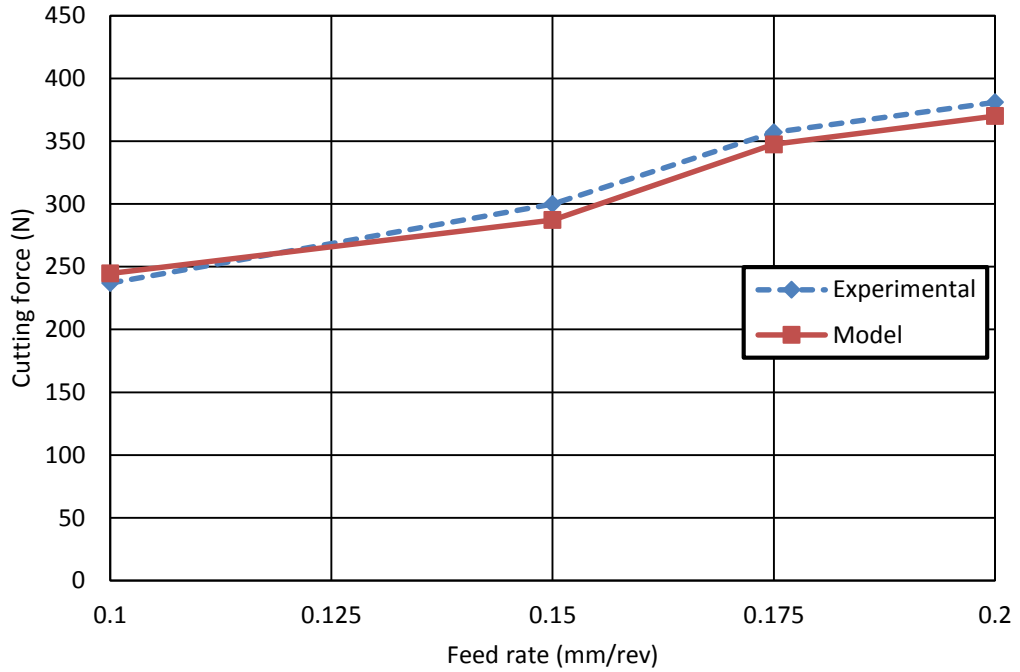


(a) Al 6061/10% 17  $\mu\text{m}$   $\text{Al}_2\text{O}_3$

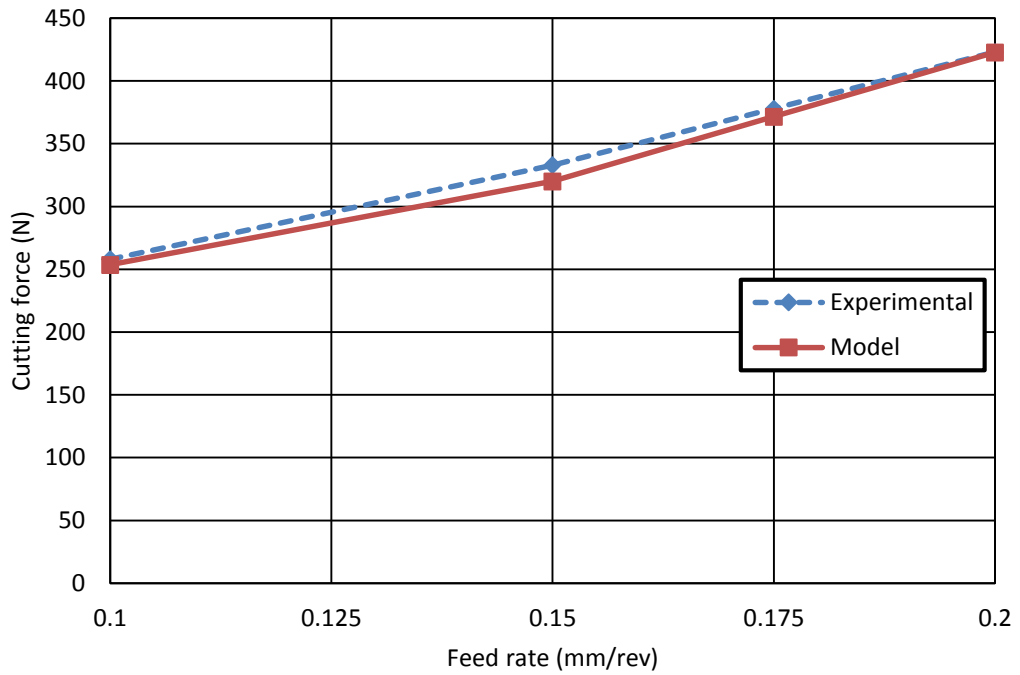


(b) Al 6061/20% 23  $\mu\text{m}$   $\text{Al}_2\text{O}_3$

Figure 5.3 Comparison of cutting force from experiments and developed model at various feed rates for machining MMCs ( $v=60$  m/min, rake angle= $6^\circ$ )

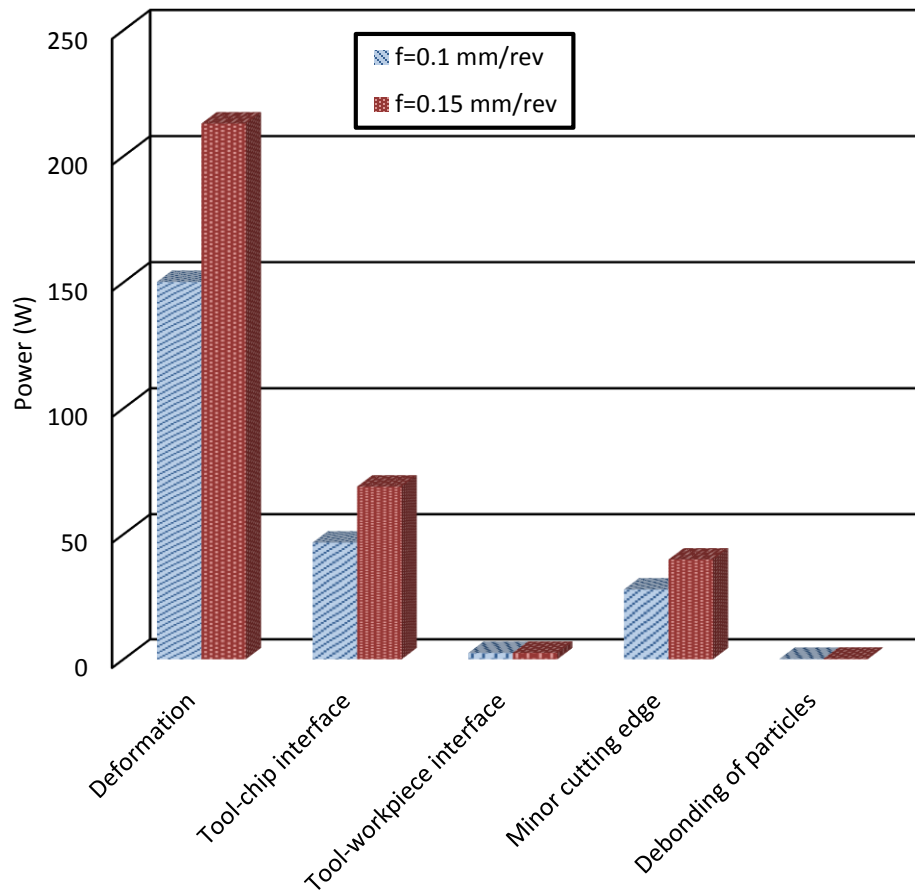


(a) Al 7075/10% 15  $\mu\text{m}$   $\text{Al}_2\text{O}_3$



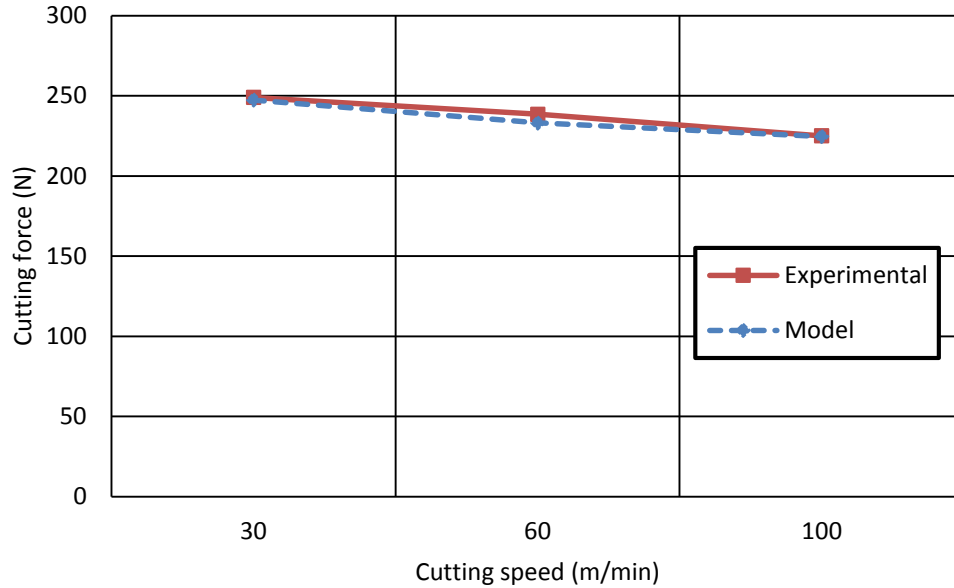
(b) Al 7075/15% 17  $\mu\text{m}$   $\text{Al}_2\text{O}_3$

Figure 5.4 Comparison of cutting force from experiments and developed model at various feed rates for machining MMCs ( $v=60$  m/min, rake angle= $6^\circ$ )



**Figure 5.5** Partition of power consumption in the MMC machining system for various feed rates (Al 6061/10% 17  $\mu\text{m}$   $\text{Al}_2\text{O}_3$ ,  $v=60$  m/min, rake angle=6°)

Figure 5.6 compares the experimental and predicted cutting force during machining MMC at different cutting speeds. This figure shows excellent agreement between the predicted and measured values; the maximum difference here is 2.2% for the case of machining at 60 m/min while the average difference between experimental and model results is 1.0%. The trend seen in this figure is expected as cutting force usually decreases with an increase in the cutting speed. This comparison proves the applicability of the proposed model in a wide range of cutting speeds.



**Figure 5.6 Comparison of cutting force from experiments and predictions by proposed model at various cutting speeds for machining Al 6061/20% 23  $\mu\text{m}$   $\text{Al}_2\text{O}_3$  (feed rate=0.1 mm/rev, rake angle=0°)**

Figure 5.7 shows the power partition of MMC machining system for various cutting speeds. As expected, the power required for plastic deformation of matrix material is the major component in total power consumption. This figure also shows an increase in components of power consumption with the increase in cutting speed. However, since the increase in power is less than the increase in the speed, the resulting cutting force will drop. As an example, as the speed increases from 30 m/min to 60 m/min (100% increase), the power components will increase by an average of only 91%; the maximum increase is seen in the power at tool-workpiece interface (around 100%) while the minimum increase occurs for the power for particle debonding (around 83%). This is because the cutting speed does not have direct influence on most of the power components of the MMC machining system. Therefore, total power consumption does not grow as much as the

cutting speed and consequently, the cutting force, which is calculated as the total power divided by the cutting speed, decreases.

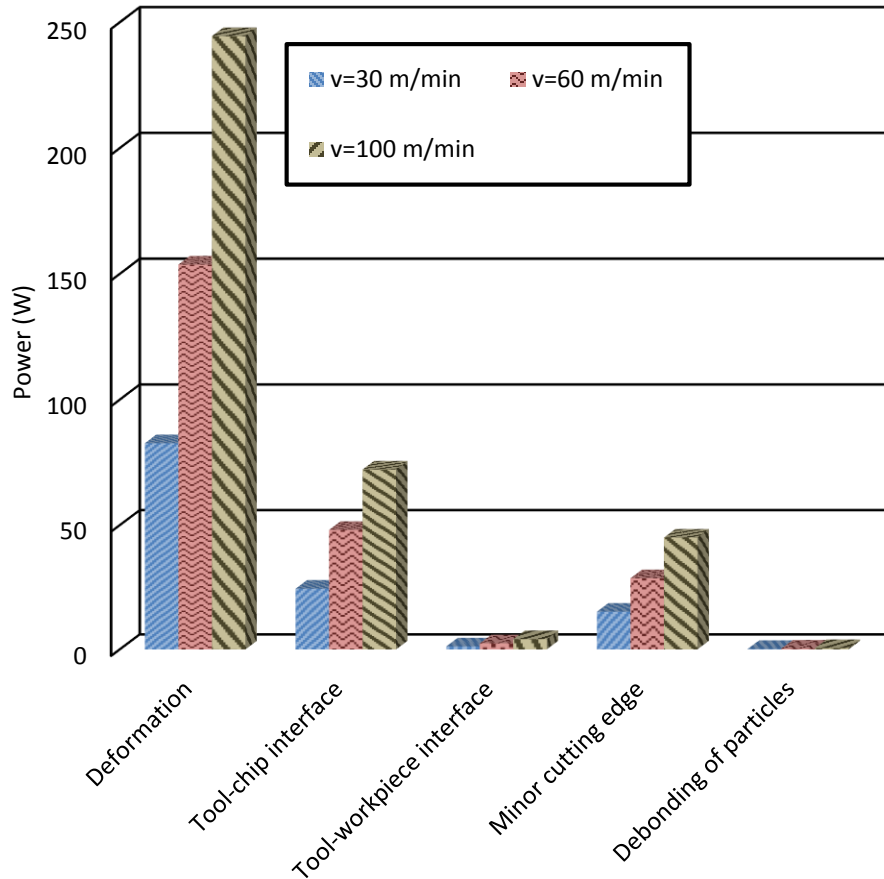


**Figure 5.7 Partition of power consumption in the MMC machining system for various cutting speeds (Al 6061/20% 23  $\mu\text{m}$   $\text{Al}_2\text{O}_3$ , feed rate=0.1 mm/rev)**

Cutting forces obtained from experiments are compared with model predictions for different particle sizes as shown in Figure 5.8. The relative difference between model results and experimental values ranges from 4.6% for a particle diameter of 9.5  $\mu\text{m}$  to 10.4% for a particle diameter of 25  $\mu\text{m}$ . Although these predictions may be acceptable, considering the wide range of particle sizes covered in this graph, the deviation of model predictions from test results is still large. This may be related to the fact that the model

presented in this section relies on a conventional constitutive equation that was proposed for traditional monolithic materials. In the next chapters, novel models will be developed that would better describe MMC behavior during machining.

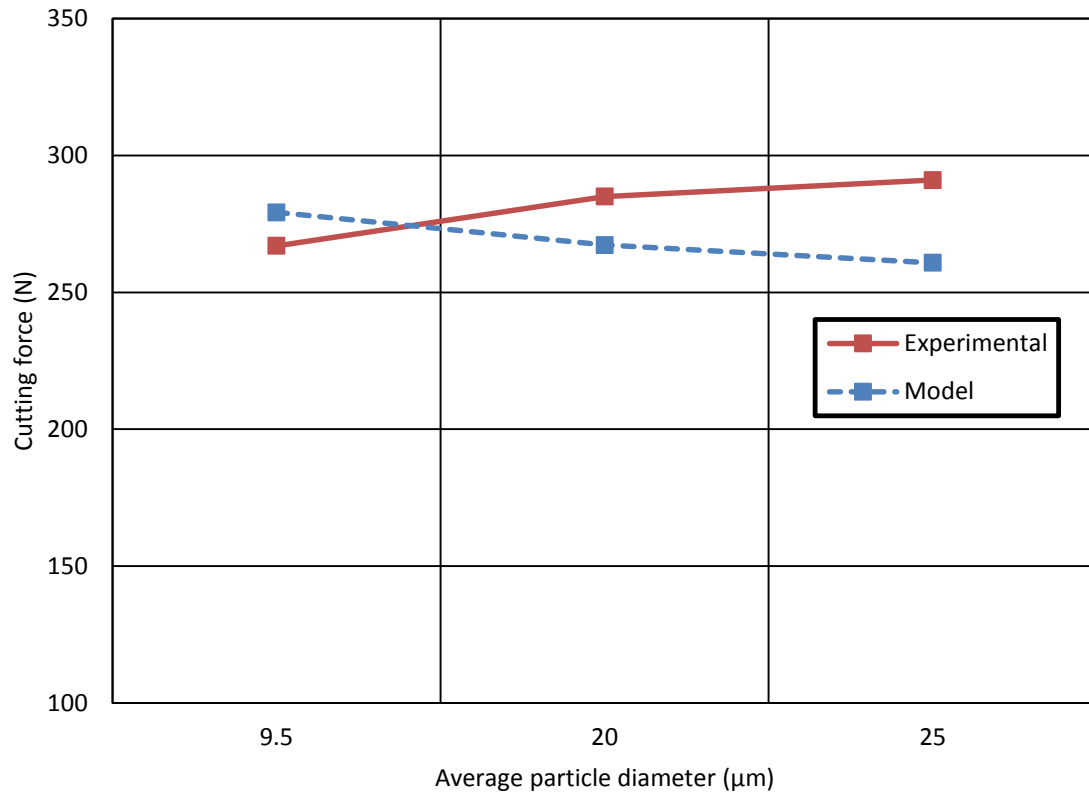


**Figure 5.8 Comparison of cutting force from experiments and predictions by proposed model for machining Al 6061/20%  $\text{Al}_2\text{O}_3$  with various particle diameters ( $v=30$  m/min, feed rate=0.1 mm/rev)**

## 5.5 Closing remarks

A novel force model for prediction of cutting force during machining MMCs was presented in this chapter. The force model was developed based on partition of power consumption in the MMC machining system. Various components of power dissipation

were calculated. Comparison with experimental results for machining various composites at different feed rates and cutting speeds confirms the ability of the proposed model to accurately predict the cutting forces during machining MMCs. Nevertheless, the developed model relied on a conventional constitutive equation that was proposed for traditional monolithic materials. As a result, the model predictions for MMCs with different particle sizes were not as accurate. In order to address this issue, in the next chapter a novel constitutive equation will be proposed that would describe the explicit relationship between MMC behavior and its features, namely particle fraction and size of reinforcements.

# **Chapter 6 Novel Constitutive Model for MMC Behavior during Machining**

## **6.1 Introduction**

The analytical models used by researchers for describing MMC behavior during machining have been relatively successful in defining the effects of some unique features of MMCs, such as volume fraction and size of reinforcements, on different process outputs. However, these models rely on constitutive equations that are usually utilized for modeling traditional monolithic materials. As a result, in these constitutive equations, the relationship between the process parameters and the unique MMC features is not explicitly described. Instead, the effect of MMC features is implicitly embedded in the model constants.

Mechanics of chip formation and cutting process are mainly affected by the behavior of workpiece material during machining. Constitutive models are used for

simulation of this behavior. These models are commonly in the form of relations between flow stress, strain, strain rate, and temperature. For the case of MMCs, the constitutive model should also incorporate the unique composite characteristics, namely volume fraction and size of reinforcements.

In this chapter, the models used by researchers for simulation of MMC behavior will be presented. Then, using the ideas offered in these models, a novel constitutive equation for simulation of the behavior of particulate MMCs during cutting will be developed. This equation will establish a meaningful connection between the MMC behavior and its unique features.

## 6.2 Models used for simulation of MMC behavior

**6.2.1 Johnson-Cook equation:** The model developed by Johnson and Cook [80] for monolithic materials has been used by some researchers for simulation of MMC behavior [12, 81]. This model is shown in equation (6-1).

$$\sigma = (A + B\epsilon^n) \left[ 1 + C \ln\left(\frac{\dot{\epsilon}}{\dot{\epsilon}_0}\right) \right] \left[ 1 - \left( \frac{T - T_{\text{transition}}}{T_{\text{melt}} - T_{\text{transition}}} \right)^m \right] \quad (6-1)$$

The empirical model shown in equation (6-1) combines the three terms that account for material's quasi-static behavior, strain rate dependence, and temperature dependence, respectively. It is clear that in this model, the effects of MMC's particle size and volume fraction are not explicitly described and are embedded in the material

constants,  $A, B, C, n$ , and  $m$ . Therefore, a new set of constants should be obtained using experiments for each MMC with different size and volume fraction of particles.

**6.2.2 Li and Ramesh equation:** Li and Ramesh [129] performed several experiments to understand the influence of volume fraction of reinforcements on the behavior of MMCs. Using these experimental results, they proposed the following empirical model:

$$\sigma = \sigma_0(\epsilon) \cdot g(V_f) \cdot \left[ 1 + \left( \frac{\dot{\epsilon}}{\dot{\epsilon}_{00}} \right)^r \right] \cdot \left[ 1 + V_f \cdot \left( \frac{\dot{\epsilon}}{\dot{\epsilon}_{00}} \right)^r \right] \quad (6-2)$$

In equation (6-2),  $\sigma_0(\epsilon)$  is the stress-strain response of the matrix material at quasi-static deformation.  $g(V_f)$  denotes a polynomial function of particle volume fraction,  $V_f$ , that demonstrates the effect of volume fraction on the quasi-static response.  $r$  and  $\dot{\epsilon}_{00}$  are rate sensitivity parameters for the matrix material.

Equation (6-2) ignores the effect of temperature on the material behavior. Moreover, in the model presented by Li and Ramesh, the effect of reinforcement size is not considered. Despite these shortcomings, this model provides a basic understanding of the effect of particle volume fraction on the MMCs' constitutive behavior.

**6.2.3 Particle-matrix interface model:** The interface constitutive equations were proposed by Needleman [110]. This model was used by researchers for investigation of

void formation around reinforcements in MMCs [130, 131]. A more general form of this model is proposed by Tvergaard [112, 132].

According to this interface model, the normal traction at the interface,  $T_n$ , is given by equation (6-3).

$$T_n = \frac{\delta_n}{\delta_n^c} F(\lambda) \quad (6-3)$$

where  $\delta_n$  is the separation at the interface and  $\delta_n^c$  is the characteristic interface length.  $\lambda$  is a non-dimensional parameter, defined as

$$\lambda = \sqrt{2} \left( \frac{\delta_n}{\delta_n^c} \right) \quad (6-4)$$

and the function  $F(\lambda)$  is chosen as

$$F(\lambda) = \frac{27}{4} \sigma_{\max, \text{int}} (1 - \lambda)^2 \quad (6-5)$$

where  $\sigma_{\max, \text{int}}$  is the interface strength. The characteristic interface length can be calculated using the work of separation,  $\phi_{\text{sep}}$ :

$$\delta_n^c = \frac{16\phi_{\text{sep}}}{9\sigma_{\max, \text{int}}} \quad (6-6)$$

The interface constitutive model presented here is a traction-separation law which can be used for analysis of degradation of the particle-matrix interface during MMC machining.

### 6.3 Development of a novel constitutive model

A novel constitutive equation for simulation of MMC behavior during machining will be developed in this section. The main part of plastic deformation during material removal occurs in the primary shear zone. Thus, a constitutive equation for the cutting process should provide an estimation of flow stress in this zone.

**6.3.1 Flow stress in primary shear zone:** As shown in Figure 6.1, an element in MMC shear zone can consist of three parts, namely undamaged material, debonded particles where the particle-matrix bond is degraded, and cracked particles. According to the rule of mixtures, the flow stress in this shear zone is assumed to be a linear combination of flow stress in each of these parts:

$$\sigma = H_1\sigma_{\text{undamaged}} + H_2\sigma_{\text{debonded}} + H_3\sigma_{\text{cracked}} \quad (6-7)$$

where  $H_1$ ,  $H_2$ , and  $H_3$  are empirical constants. The stress in each of the three parts of the shear zone will be calculated in the following sections.

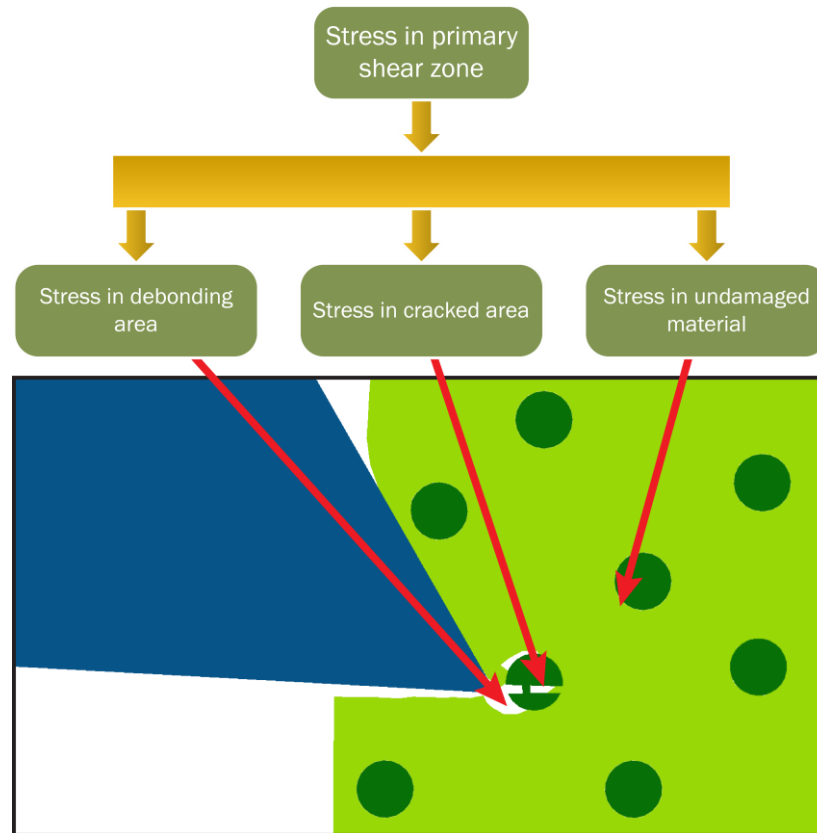


Figure 6.1 Schematic describing different deformation patterns in the primary shear zone during MMC cutting

**6.3.2 Stress in undamaged part of primary shear zone:** The stress in undamaged part of primary shear zone can be modeled using a modified form of Johnson-Cook equation. Modification of this equation can be performed using the analysis presented in the Li and Ramesh model. This model, which was presented in section 6.2.2, describes the effect of particle volume fraction on MMCs' quasi-static behavior. This effect was modeled using a polynomial function. Li and Ramesh model also showed that volume fraction can alter the influence of strain rate on the MMC behavior. Using these findings, equation (6-8) is proposed for calculation of von Mises flow stress,  $\sigma_{\text{undamaged}}$ .

$$\sigma_{\text{undamaged}} = (A + B\epsilon^n) \times g(V_f) \times \left[1 + C \ln\left(\frac{\dot{\epsilon}}{\dot{\epsilon}_0}\right)\right] \times \left[1 + CV_f \ln\left(\frac{\dot{\epsilon}}{\dot{\epsilon}_0}\right)\right] \times \left[1 - \left(\frac{T - T_{\text{transition}}}{T_{\text{melt}} - T_{\text{transition}}}\right)^m\right] \quad (6-8)$$

In equation (6-8), the quasi-static effect, the strain rate effect, and the temperature effect are modeled similar to the Johnson-Cook equation. Addition of the terms  $g(V_f)$  and  $\left[1 + CV_f \ln(\dot{\epsilon}/\dot{\epsilon}_0)\right]$  are to account for the volume fraction effects.

**6.3.3 Stress in debonded part of primary shear zone:** Debonding of particles in the MMC occurs as a result of degradation of the particle-matrix interface. Since initiation of fracture around the particle is a prerequisite for debonding, stress in the debonded area is assumed to be a function of probability of fracture and particle stress, as shown in equation (6-9).

$$\sigma_{\text{debonded}} = (V_f \cdot P_{fr}) \times \sigma_P \quad (6-9)$$

where  $\sigma_P$  is the particle stress and  $P_{fr}$  is the probability of fracture in the particles. In equation (6-9),  $(V_f \cdot P_{fr})$  denotes the volume fraction of particles involved in debonding. Probability of fracture can be modeled using Weibull's weakest link model, as shown in equation (6-10) [104].

$$P_{fr} = 1 - \exp\left[-\frac{d^3}{d_N^3} \left(\frac{\sigma_P}{\sigma_0}\right)^q\right] \quad (6-10)$$

In equation (6-10),  $q$  is the Weibull inhomogeneity factor and  $\sigma_0$  and  $d_N$  are normalizing constants.  $d$  denotes the particle diameter.

The stress in the particle depends on the level of degradation of the particle-matrix interface and stress in the matrix around the particle. Using the traction-separation law, presented in section 6.2.3, for this interface and Johnson-Cook equation for the matrix, the particle stress can be calculated using equation (6-11).

$$\sigma_P = \left( \frac{T_n}{\sigma_{\max, \text{int}}} \right) \times (A + B\epsilon^n) \times \left[ 1 + C \ln \left( \frac{\dot{\epsilon}}{\dot{\epsilon}_0} \right) \right] \times \left[ 1 - \left( \frac{T - T_{\text{transition}}}{T_{\text{melt}} - T_{\text{transition}}} \right)^m \right] \quad (6-11)$$

Equation (6-11) is developed based on the assumption that stress in the particle is equal to the stress in the matrix as long as the particle-matrix interface is not degraded. When damage is initiated in the interface, the particle stress decreases until the particle becomes stress free after full debonding.

**6.3.4 Stress in cracked part of primary shear zone:** Stress in the cracked part of shear zone will be affected by initiation and evolution of cracks in the particles. Therefore, it is assumed that in this area, stress is a function of stress in the surrounding undamaged area and probability of initiation and evolution of cracks in the particles. Based on this assumption, equation (6-12) can be developed for estimation of stress in the cracked area of shear zone.

$$\sigma_{\text{cracked}} = (V_f \cdot P_{fr}) \times (A + B\epsilon^n) \times g(V_f) \times \left[ 1 + C \ln \left( \frac{\dot{\epsilon}}{\dot{\epsilon}_0} \right) \right] \times \left[ 1 + CV_f \ln \left( \frac{\dot{\epsilon}}{\dot{\epsilon}_0} \right) \right] \times \left[ 1 - \left( \frac{T - T_{\text{transition}}}{T_{\text{melt}} - T_{\text{transition}}} \right)^m \right] \quad (6-12)$$

Having obtained the different terms of stress, equation (6-7) can now be used for calculation of total flow stress in the primary shear zone.

#### **6.4 Closing remarks**

The constitutive model presented in this chapter overcomes the shortcomings of previous models. One of the most significant achievements of the developed model is incorporation of the effects of MMC's unique features, i.e. MMC's parameters are explicitly included in the equations and are not embedded in equation constants. As a result, constants in this equation are independent of particle volume fraction and size. Therefore, the same constants can be used for all MMCs with similar matrix and particle materials even if volume fraction and size of reinforcements are different. This achievement makes this model unique in that it clarifies the relationships between MMC characteristics and the material behavior. In the next chapter, the developed constitutive equation will be incorporated in an analytical model for prediction of cutting force during MMC machining.

# **Chapter 7 Calculation of Cutting Force Using the Developed Constitutive Model**

## **7.1 Introduction**

In the previous chapter, a novel constitutive equation for simulation of MMC behavior during machining was proposed. This constitutive equation can be used in a model for prediction of cutting force. Development of a force model is required for validation of the constitutive equation through comparison with experimental data. This is because the direct output of the constitutive equation, which is the flow stress in the primary shear zone, is not a parameter which can be measured in the cutting tests. On the other hand, cutting force is a parameter which can be measured directly in the machining experiments and compared with model predictions. Therefore, in this chapter, a model for prediction of cutting force using the proposed constitutive equation will be developed and the model's applicability will be verified through comparison with experimental data.

## 7.2 Modeling cutting force based on energy partition

The cutting force model presented in this section is an energy-based model that is similar to the model developed in Chapter 5. This model is obtained by considering the power balance in the cutting system. Using this approach, the cutting force,  $F_c$ , can be calculated using the model of energy partition in metal cutting as described in equation (7-1) [74].

$$F_c = \frac{P_c}{v} = \frac{P_{pd} + P_{tc} + P_{tw} + P_{fns} + P_{mnc}}{v} \quad (7-1)$$

In equation (7-1),  $P_c$  is the total cutting power and  $v$  is the cutting speed.  $P_{pd}$  represents the power consumption for plastic deformation due to material layer removal, while  $P_{tc}$  denotes the power spent at the tool-chip interface and  $P_{tw}$  is the power spent at the tool-workpiece interface.  $P_{fns}$  and  $P_{mnc}$  are the power consumption for formation of new surfaces and the power spent due to the effect of minor cutting edge, respectively.

The constitutive equation developed in Chapter 6 previous chapter, will be used to calculate the power required for plastic deformation, which is the major part of power consumption in the machining system. Equations for obtaining the power spent at the tool-chip and tool-workpiece interfaces as well as the effect of the minor cutting edge are provided in Chapter 5.

### 7.3 Implementation of the developed constitutive equation

**7.3.1 Power for plastic deformation:** The developed constitutive equation provides the flow stress in the primary shear zone as a function of strain, strain rate, temperature, and MMC characteristics, namely volume fraction and size of particles. This equation can be used for calculation of the power required for plastic deformation during material removal. This plastic deformation occurs in the primary shear zone. Using the strain energy density in this zone:

$$P_{pd} = vA_c \int_0^{\epsilon} \sigma d\epsilon \quad (7-2)$$

where  $A_c$  is the cross-sectional area of the uncut chip. Flow stress,  $\sigma$ , can now be replaced using the developed constitutive model (equation (6-7)) to obtain the following equation.

$$P_{pd} = vA_c \int_0^{\epsilon} (H_1\sigma_{\text{undamaged}} + H_2\sigma_{\text{debonded}} + H_3\sigma_{\text{cracked}}) d\epsilon \quad (7-3)$$

$$\begin{aligned}
P_{pd} = & v \cdot A_c \cdot H_1 \cdot \left( A \cdot \epsilon + \frac{B}{n+1} \cdot \epsilon^{n+1} \right) \cdot g(V_f) \cdot \left[ 1 + C \cdot \ln \left( \frac{\dot{\epsilon}}{\dot{\epsilon}_0} \right) \right] \cdot \left[ 1 \right. \\
& + C \cdot V_f \cdot \ln \left( \frac{\dot{\epsilon}}{\dot{\epsilon}_0} \right) \left. \right] \cdot \left[ 1 - \left( \frac{T - T_{\text{transition}}}{T_{\text{melt}} - T_{\text{transition}}} \right)^m \right] \\
& + v \cdot A_c \cdot H_2 \cdot V_f \int_0^\epsilon P_{fr} \cdot \sigma_p \cdot d\epsilon \\
& + v \cdot A_c \cdot H_3 \cdot V_f \int_0^\epsilon \left\{ P_{fr} \cdot (A + B \cdot \epsilon^n) \cdot g(V_f) \cdot \left[ 1 \right. \right. \\
& + C \cdot \ln \left( \frac{\dot{\epsilon}}{\dot{\epsilon}_0} \right) \left. \right] \cdot \left[ 1 + C \cdot V_f \cdot \ln \left( \frac{\dot{\epsilon}}{\dot{\epsilon}_0} \right) \right] \cdot \left[ 1 \right. \\
& \left. \left. - \left( \frac{T - T_{\text{transition}}}{T_{\text{melt}} - T_{\text{transition}}} \right)^m \right] \right\} \cdot d\epsilon
\end{aligned} \tag{7-4}$$

In equation (7-4), the first term represents the power for deformation in the undamaged material while the second and third terms denote the power for deformation in the debonded and cracked parts of the primary shear zone, respectively:

$$P_{pd} = H_1 P_{pd\text{-undamaged}} + H_2 P_{pd\text{-debonded}} + H_3 P_{pd\text{-cracked}} \tag{7-5}$$

The second and third terms in equation (7-4) cannot be integrated analytically and numerical integration techniques should be used. In the following sections, calculation of the parameters required for using equation (7-4) will be detailed.

**7.3.2 Equivalent plastic strain:** Traditional methods for calculation of shear strain, such as the one proposed by Merchant [59], were obtained using pure geometrical assessment of chip formation. However, as pointed out by Astakhov and Shvets [121],

Merchant's method can lead to erroneous results as it ignores the changes in chip's internal energy, dislocation concentration, etc.

Using an analysis of the work of external force during plastic deformation in metal cutting, Astakhov and Shvets [121] proposed the following equation for calculation of the plastic strain,  $\epsilon$ .

$$\epsilon = 1.15 \ln \zeta \quad (7-6)$$

where  $\zeta$  is the chip compression ratio and is defined as the ratio of the chip thickness to the uncut chip thickness.

**7.3.3 Cutting zone temperature:** According to Oxley [68], the temperature in the primary shear zone,  $T_s$ , during metal cutting can be calculated using the following equation.

$$T_s = T_w + \eta \Delta T_s \quad (7-7)$$

where  $T_w$  is the initial workpiece temperature and  $\eta$  ( $0 < \eta \leq 1$ ) is the factor representing the amount of plastic work that occurs in primary shear zone. An approximate average value of  $\eta \approx 0.7$  can be used as an assumption [133].  $\Delta T_s$  is the rise in temperature in the primary shear zone and can be calculated by considering the plastic work:

$$\Delta T_s = \left( \frac{1 - \lambda_s}{\rho c d_c f} \right) \left[ \frac{F_s \cos \gamma}{\cos(\phi - \gamma)} \right] \quad (7-8)$$

Here,  $\rho$  is the density of workpiece material,  $c$  is the specific heat, and  $\phi$  denotes the shear angle and is given by

$$\phi = \tan^{-1} \left( \frac{\frac{1}{\zeta} \cos \gamma}{1 - \frac{1}{\zeta} \sin \gamma} \right) \quad (7-9)$$

$\lambda_s$  is the factor representing the amount of heat transformed into work and is given using the empirical relations presented by Oxley [67].

$$\lambda_s = \begin{cases} 0.5 - 0.35 \log(R_T \tan \phi) & \text{for } 0.04 \leq R_T \tan \phi \leq 10.0 \\ 0.3 - 0.15 \log(R_T \tan \phi) & \text{for } R_T \tan \phi > 10.0 \end{cases} \quad (7-10)$$

Here,  $R_T$  is the dimensionless thermal number:

$$R_T = \frac{\rho c v f}{k} \quad (7-11)$$

where  $k$  is the workpiece material thermal conductivity. In equation (7-8),  $F_s$  denotes the shear force and is calculated by

$$F_s = \sqrt{F_c^2 + F_t^2} \cos(\phi + \beta - \gamma) \quad (7-12)$$

In equation (7-12)  $F_t$  is the thrust force and  $\beta$  is the friction angle and is given by

$$\beta = \gamma + \tan^{-1} \left( \frac{F_t}{F_c} \right) \quad (7-13)$$

The equations presented in this section will be used for calculation of temperature during machining. Since cutting force is required in calculation of temperature, these equations will be used in an iterative solver for calculation of cutting force.

**7.3.4 Strain rate:** Calculation of strain rate can be performed using empirical equations. Using Oxley's investigation [68], strain rate in the primary shear zone is given by

$$\dot{\epsilon} = 5.9 \frac{v_s}{l} \quad (7-14)$$

where  $v_s$  and  $l$  are the shear velocity and shear length, respectively, and are calculated using the following equations.

$$v_s = \frac{v \cos \gamma}{\cos(\phi - \gamma)} \quad (7-15)$$

$$l = \frac{f}{\sin \phi} \quad (7-16)$$

## 7.4 Experimental verification of model results

Applicability of the force model, which is based on the developed constitutive equation, can be confirmed through comparison with experimental data. Cutting experiments were performed on Al 6061/Al<sub>2</sub>O<sub>3</sub> and Al 7075/Al<sub>2</sub>O<sub>3</sub> particle reinforced MMCs using tungsten carbide cutting tools. The cutting tools have rake angles of 0° and 6° and a flank angle of 11°. Parameters used in the cutting force model are listed in Table 7.1. Table 7.2 provides the machining process parameters.

**Table 7.1 Material parameters used in the cutting force model**

$d_N$ ( $\mu\text{m}$ ) [134]	1.0	
$\sigma_0$ (MPa) [118]	395	
$q$ [118]	11	
$g(V_f)$ [129]	$1 + 0.96V_f$	
$\phi_{sep}$ ( $\text{J}/\text{m}^2$ ) [56]	50	
	Al 6061/ $\text{Al}_2\text{O}_3$	Al 7075/ $\text{Al}_2\text{O}_3$
$\sigma_{\text{max,int}}$ (MPa) [127]	552	1006
$\sigma_R$ (MPa) [127]	310	572
$\tau_y$ (MPa) [127]	207	331
Particle volume fraction (%)	10, 20	10, 15
Average particle diameter ( $\mu\text{m}$ )	9.5, 17, 20, 23, 25	15, 17
Johnson-Cook model parameters [117, 128]		
$A$ (MPa)	324	496
$B$ (MPa)	114	310
$C$	0.002	0.0
$n$	0.42	0.3
$m$	1.34	1.2
$T_{\text{melt}}$ ( $^{\circ}\text{C}$ )	651	635
$T_{\text{transition}}$ ( $^{\circ}\text{C}$ )	20	20
$\dot{\epsilon}_0$	1.0	1.0

**Table 7.2 Parameters of the machining experiments**

Feed rate (mm/rev)	0.1, 0.15, 0.175, 0.2
Cutting speed (m/min)	30, 60, 100
Depth of cut (mm)	3

The first step in verification of the developed model is obtaining the empirical parameters,  $H_1$ ,  $H_2$ , and  $H_3$ , of the constitutive model (equation (6-7)). The cutting forces obtained in four cutting tests were used for tuning the model constants for each matrix material (Table 7.3). The least squares method was employed for this reverse calculation. The obtained model constants for each MMC are presented in Table 7.4.

**Table 7.3 Parameters of cutting tests used for obtaining the model constants**

	Volume fraction (%)	Particle diameter ( $\mu\text{m}$ )	Feed rate (mm/rev)	Cutting speed (m/min)	Tool rake angle
Al 6061/ $\text{Al}_2\text{O}_3$	10	17	1.5	60	6°
	20	23	1.75	60	6°
	20	23	1	30	0°
	10	20	1	30	0°
Al 7075/ $\text{Al}_2\text{O}_3$	15	17	1.5	60	6°
	15	17	1.75	60	6°
	10	15	1	60	6°
	10	15	2	60	6°

**Table 7.4 Constitutive model constants tuned using experimental data**

	$H_1$	$H_2$	$H_3$
Al 6061/ $\text{Al}_2\text{O}_3$	1.0123	-3426.9429	8969.6007
Al 7075/ $\text{Al}_2\text{O}_3$	1.5942	-645.3440	1307.4407

## 7.5 Results and discussion

**7.5.1 *Model verification:*** The cutting force values obtained from experiments are compared with the values calculated using the proposed model for various feed rates as depicted in Figure 7.1 and Figure 7.2. It is evident that model results are in very good agreement with the experimental data; maximum deviation between the model and experimental values is 5.73%, which is only seen in Figure 7.2 (a) with a feed rate of 0.1 mm/rev. The average difference in all cases is 2.47%. This verifies the ability of the proposed constitutive model to simulate the MMCs' behavior during cutting.

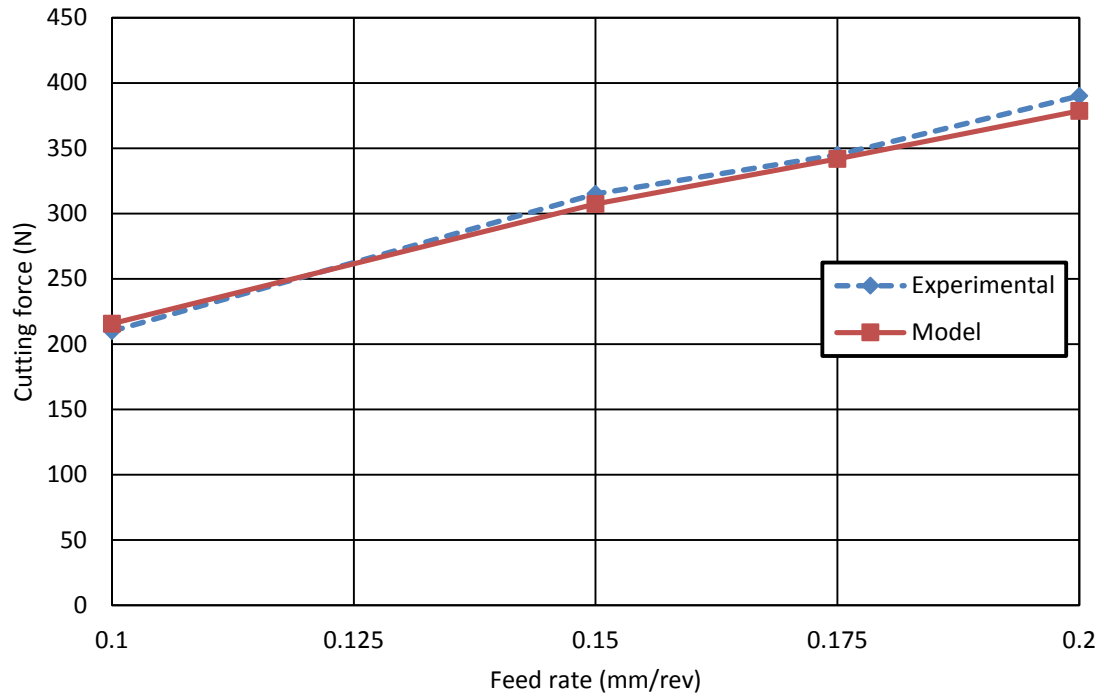
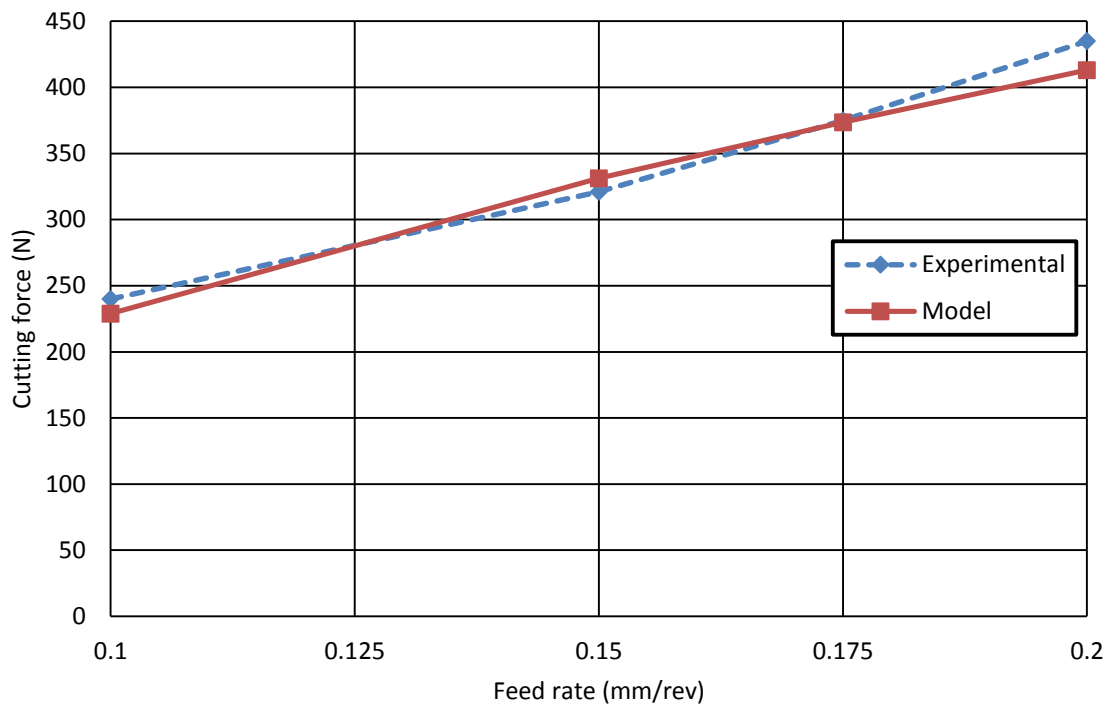
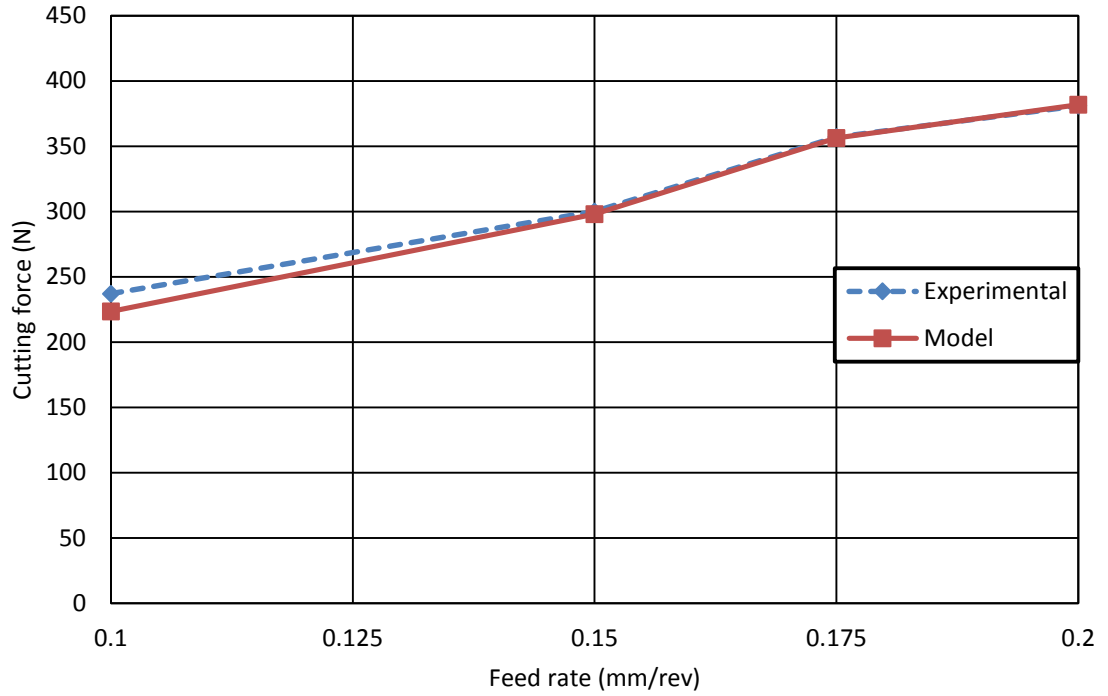
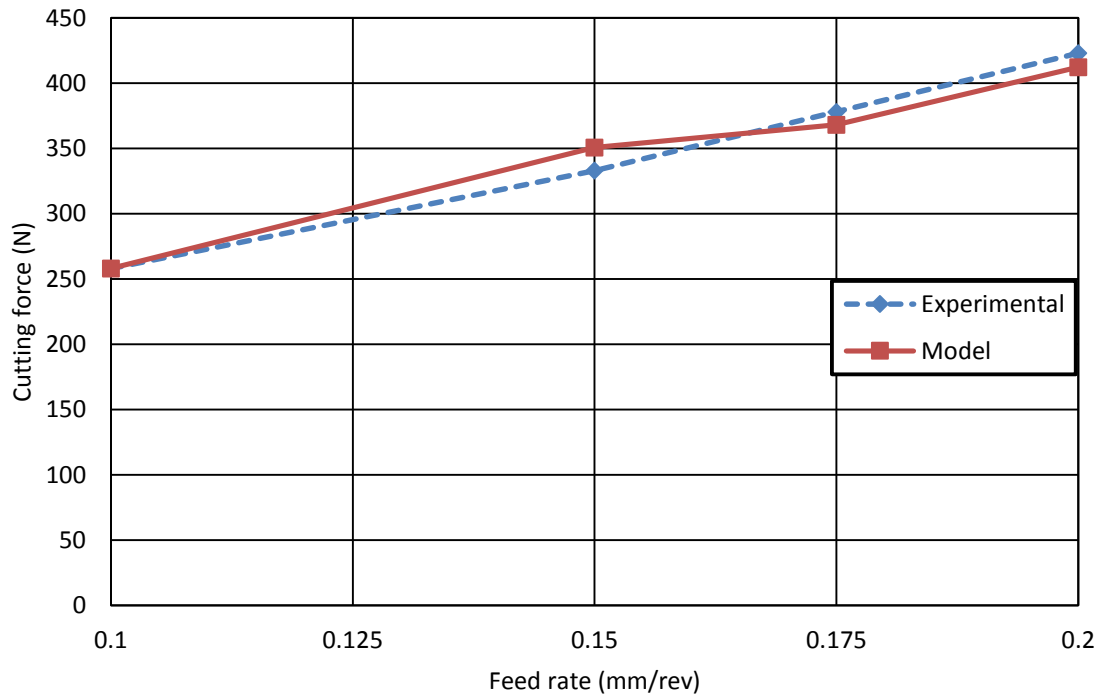
(a) Al 6061/10% 17  $\mu\text{m}$   $\text{Al}_2\text{O}_3$ (b) Al 6061/20% 23  $\mu\text{m}$   $\text{Al}_2\text{O}_3$ 

Figure 7.1 Comparison of cutting force from experiments and developed model at various feed rates for machining MMCs ( $v=60$  m/min, rake angle= $6^\circ$ )



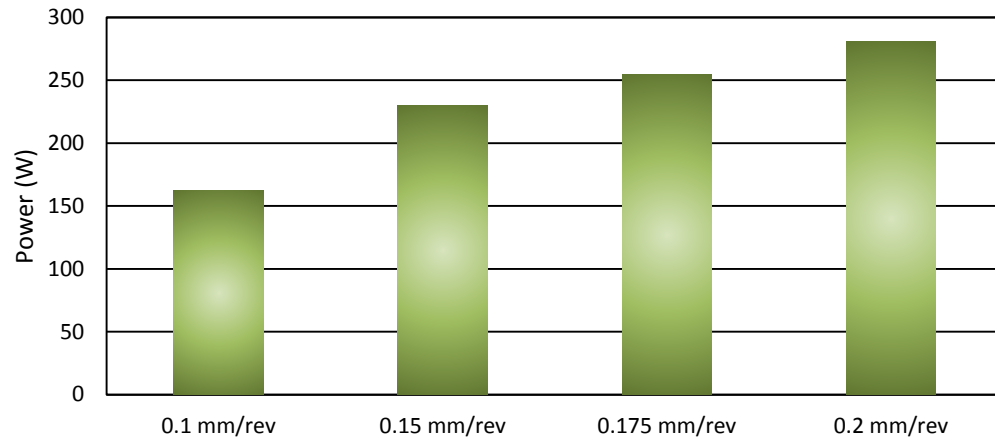
(a) Al 7075/10% 15  $\mu\text{m}$   $\text{Al}_2\text{O}_3$



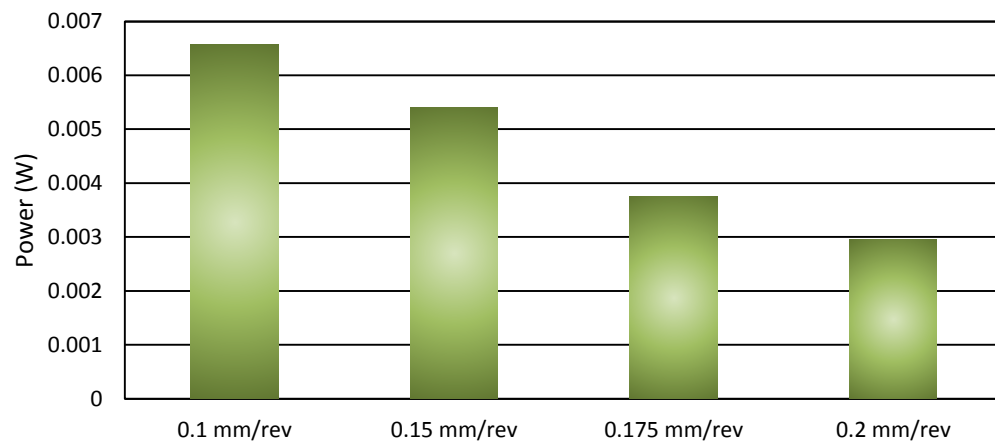
(b) Al 7075/15% 17  $\mu\text{m}$   $\text{Al}_2\text{O}_3$

Figure 7.2 Comparison of cutting force from experiments and developed model at various feed rates for machining MMCs ( $v=60$  m/min, rake angle= $6^\circ$ )

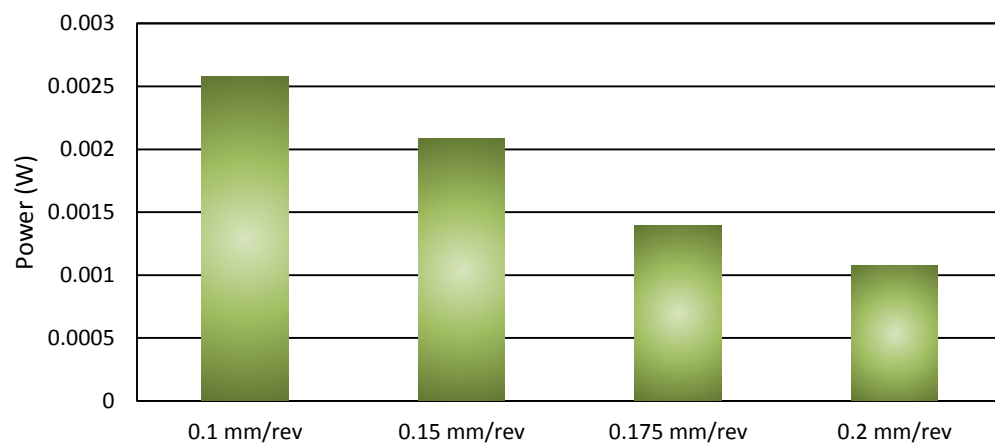
As discussed earlier, according to the developed constitutive equation, the power for plastic deformation consists of three terms, namely the power for deformation in the undamaged material, the power for deformation in the debonded part, and the power for deformation in the cracked part of the primary shear zone. These terms of power for plastic deformation are graphed in Figure 7.3. This graph shows that an increase in feed rate will result in increased power for deformation in the undamaged area. This is while increased feed rate leads to reduction in the other terms of power for deformation. This observation can be attributed to the strain in the deformation zone. Experiments show that cutting with a larger feed rate will lead to a smaller chip compression ratio, which is a sign of smaller plastic strain. In the first term of power for deformation, the effect of larger feed rate is greater than the effect of smaller strain. However, in the power for deformation in debonded and cracked areas, the effect of smaller plastic strain is more evident. In total, the power required for deformation grows with an increase in the feed rate (Figure 7.4).



(a) power for deformation in the undamaged material

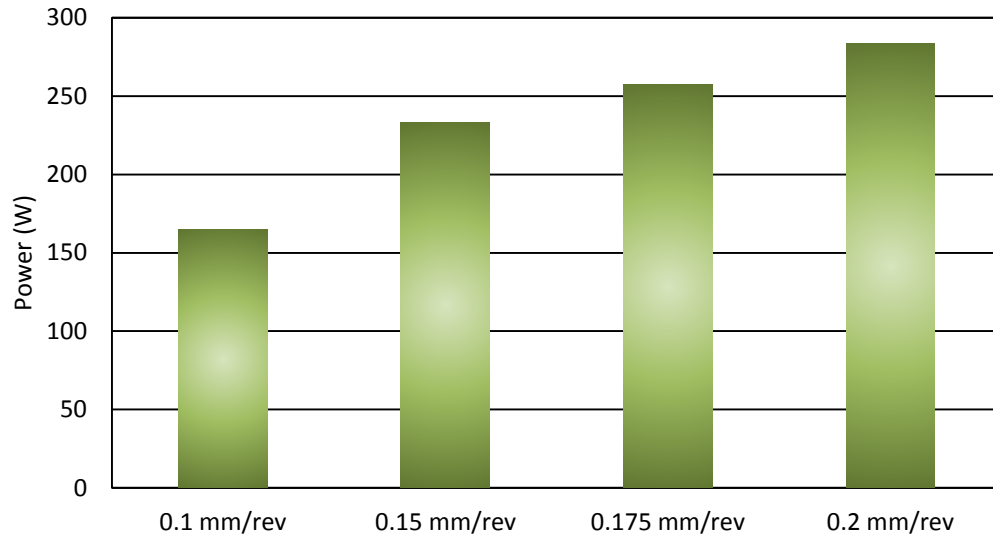


(b) power for deformation in the debonded part



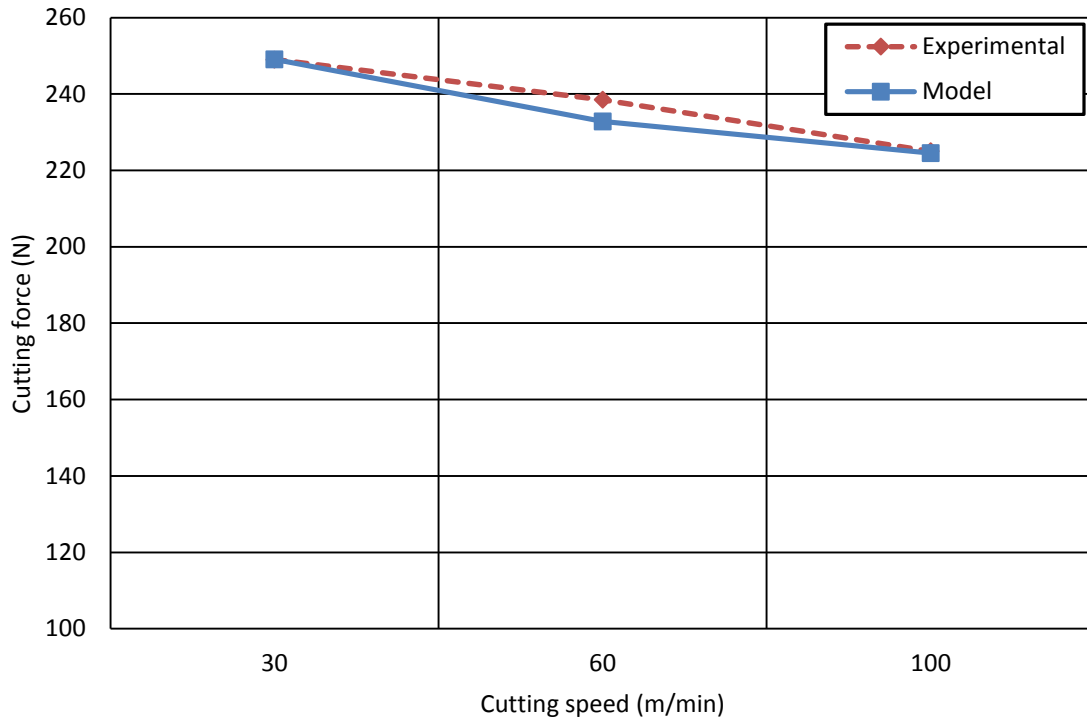
(c) power for deformation in the cracked part

Figure 7.3 Different terms of power for plastic deformation for various feed rates (Al 6061/10% 17  $\mu\text{m}$   $\text{Al}_2\text{O}_3$ ,  $v=60$  m/min, rake angle=6°)



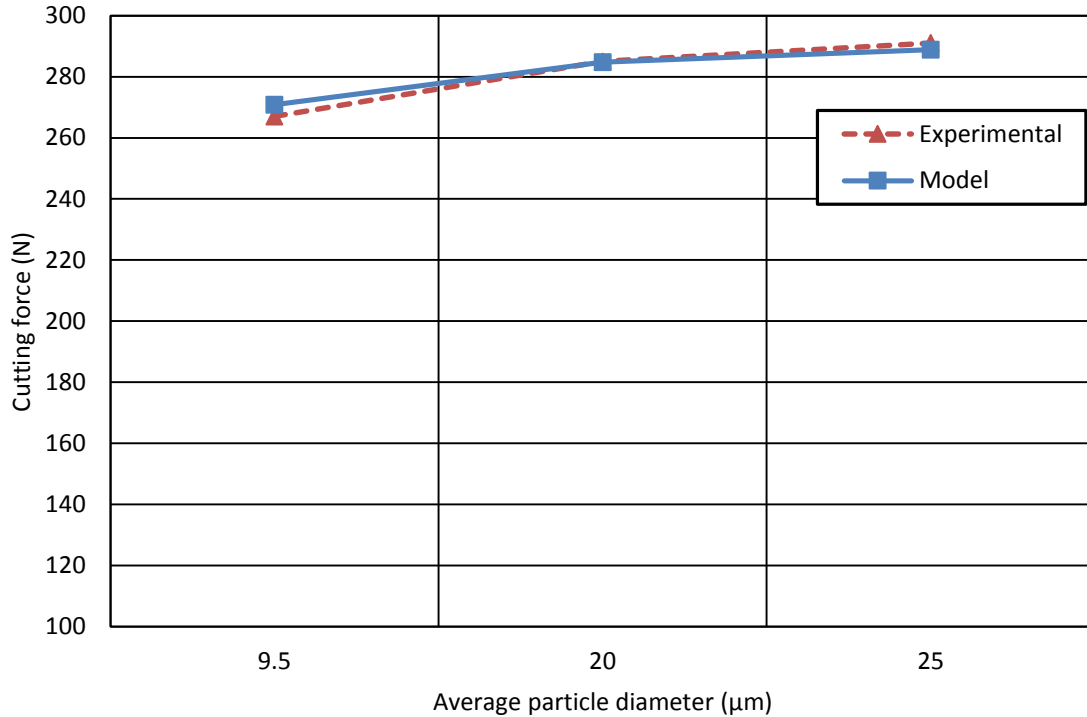
**Figure 7.4 Power required for deformation during cutting with various feed rates (Al 6061/10% 17  $\mu\text{m}$   $\text{Al}_2\text{O}_3$ ,  $v=60$  m/min, rake angle= $6^\circ$ )**

Figure 7.5 compares the experimental and model cutting force when cutting at different cutting speeds. The trend seen in this figure is expected as cutting force usually decreases with an increase in cutting speed. Results from the proposed model also follow a similar trend and are in good agreement with experimental results with a maximum deviation of 2.37%. The average difference between model and experimental values in all three cases is 0.87%. This comparison proves the applicability of the proposed model in a wide range of cutting speeds.



**Figure 7.5 Comparison of cutting force from experiments and proposed model at various cutting speeds for machining Al 6061/20% 23  $\mu\text{m}$   $\text{Al}_2\text{O}_3$  (feed=0.1 mm/rev, rake angle=0°)**

The comparison of cutting force values obtained from experiments and the developed model for a range of particle sizes is shown in Figure 7.6. The agreement between the results demonstrates the ability of the developed constitutive equation to simulate the MMC behavior over a wide range of particle diameters; the deviation between model and experimental results does not exceed 1.43% while the average difference in all cases is 0.74%.



**Figure 7.6 Comparison of cutting force from experiments and proposed model for machining Al 6061/20%  $\text{Al}_2\text{O}_3$  with various particle diameters ( $v=30$  m/min, feed=0.1 mm/rev, rake angle=0°)**

The model's ability to provide such close predictions of the cutting force during MMC machining is a result of using the developed constitutive equation. The constitutive equation presented in this research includes an explicit connection to MMC's unique features, and thus provides an accurate simulation of behavior of MMCs with various particle sizes. Results plotted in Figure 7.6 are clear indications of this capability.

**7.5.2 Parametric study:** In this section, the effect of variation of parameters on the cutting force during machining MMCs is studied. Figure 7.7 shows the effect of particle of diameter on the MMC cutting force. This graph is plotted for different chip compression ratios. This figure demonstrates an increase in cutting force as the MMC particle diameter increases. An explanation for this observation is that, as the particle size increases, the

power required for fracture and debonding of particles rises, which then leads to an increase in cutting force.

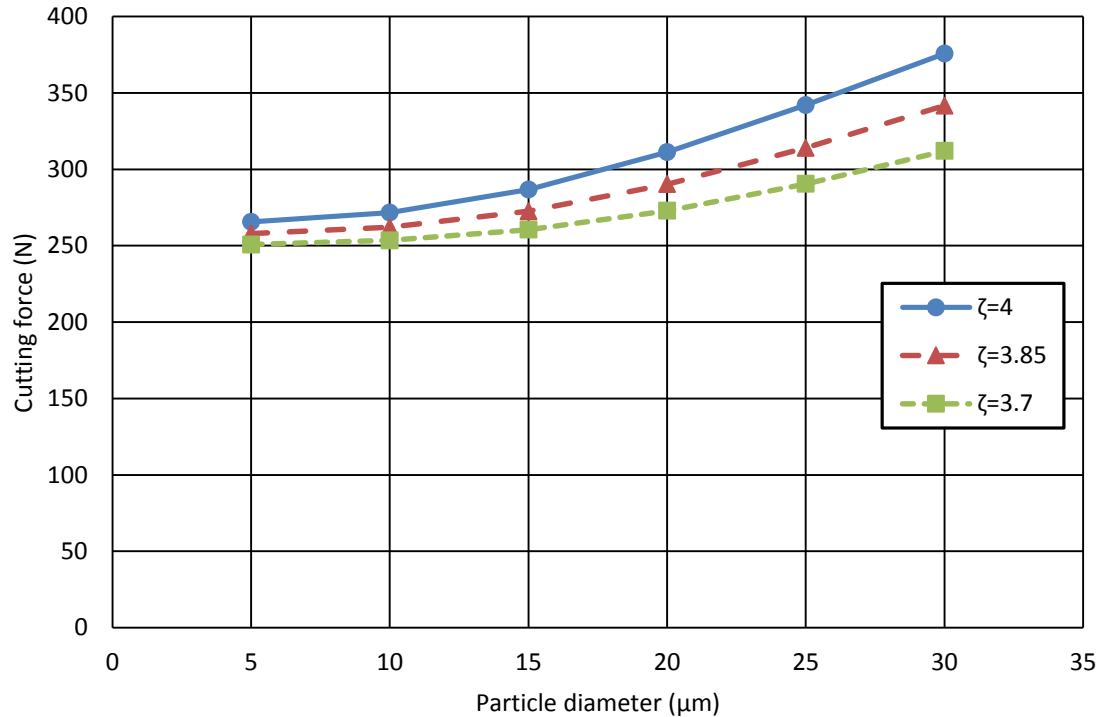


**Figure 7.7** Variation of cutting force versus particle diameter during MMC machining (Al 6061/10%  $\text{Al}_2\text{O}_3$  MMC,  $v=30$  m/min, feed=0.1 mm/rev, rake angle=0°)

In Figure 7.8, cutting force values are plotted against variation of cutting speed for different chip compression ratios. As expected, an increase in cutting speed results in lower cutting forces. This is because an increase in speed leads to increased temperature and strain rate during metal cutting which cause softening of MMC workpiece. Softened workpiece material will require lower cutting forces.

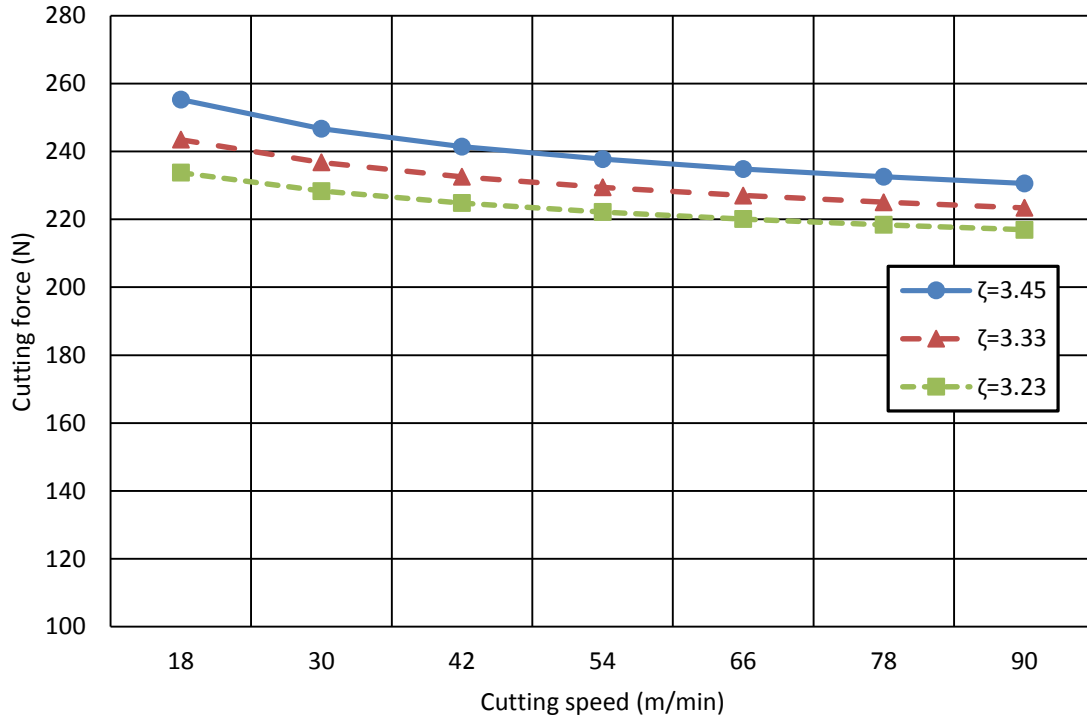


**Figure 7.8** Variation of cutting force versus cutting speed during MMC machining (Al 6061/10% 20  $\mu\text{m}$   $\text{Al}_2\text{O}_3$  MMC, feed=0.1 mm/rev, rake angle=0°)

Figure 7.9 shows the effect of particle volume fraction on the cutting force during MMC machining. According to this figure, increase in volume fraction initially results in higher cutting forces. However, as the volume fraction increases above 20%, it leads to a decrease in the cutting force. This observation can be attributed to the effect of particles on the MMC behavior. An increase in volume fraction leads to a larger number of particles in the MMC workpiece. When the number of particles increases up to a certain value, the power required for debonding and fracture of particles increases, which will result in increased cutting forces. However, a further increase in the number of particles will cause the distance between particles to become very small, which will lead to large stress concentrations and easier initiation and evolution of cracks in the matrix. A higher

number of cracks will decrease the power required for chip formation and, consequently, the cutting force.

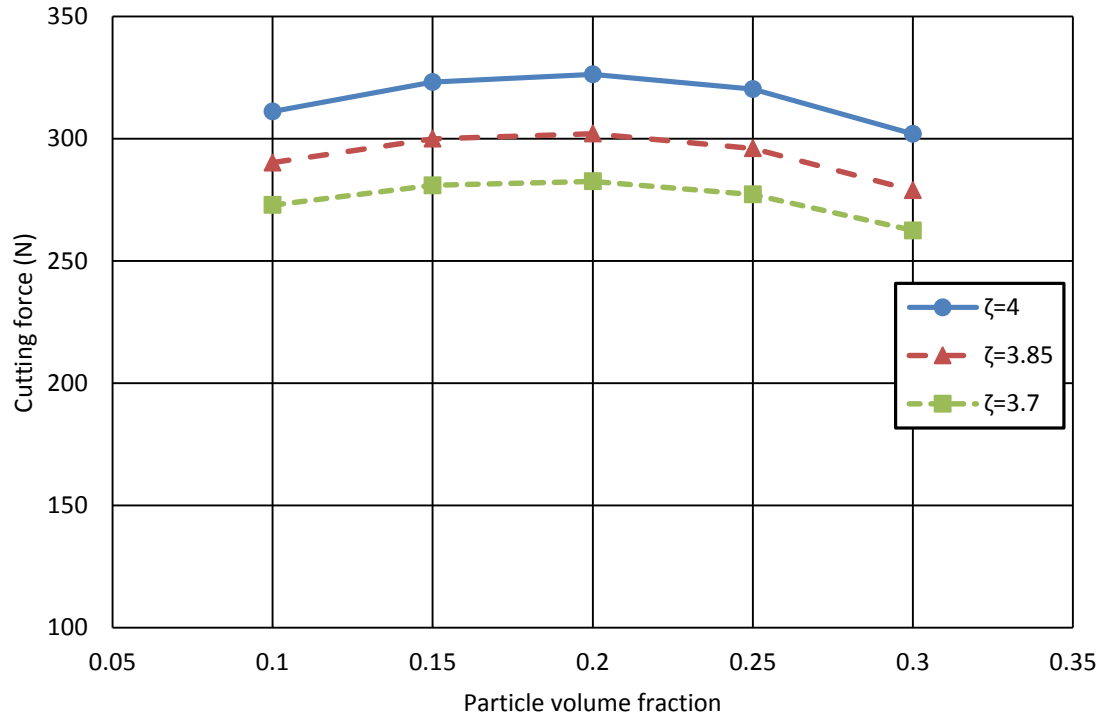


Figure 7.9 Variation of cutting force versus reinforcement volume fraction during MMC machining (Al 6061/20  $\mu\text{m}$   $\text{Al}_2\text{O}_3$  MMC,  $v=30$  m/min, feed=0.1 mm/rev, rake angle=0°)

## 7.6 Closing remarks

An analytical model for prediction of cutting forces during machining MMCs using the developed constitutive equation was presented in this chapter. Results provided in this chapter clearly demonstrated the ability of the developed model to predict the behavior of MMCs with various particle sizes and volume fractions during cutting with different process parameters. It should be noted that all model results were calculated

using one set of constants for each matrix material. Therefore, by obtaining the constants of the constitutive equation from tests on a specific matrix and particle combination, the developed model can be used to simulate the behavior of all MMCs made with the same materials, but with different volume fraction and size of particles. This is considered to be a major breakthrough in modeling MMC machining.

# Chapter 8 Conclusions and Future Work

## 8.1 Conclusions

This thesis presents analyses of machining metal matrix composites. The presented analyses succeeded in providing a comprehensive understanding of MMC cutting process. This understanding was achieved through modeling of the process using finite element and analytical methods.

The finite element analysis was performed for machining a particle-reinforced MMC using Abaqus commercial FEM software. In this analysis, the cutting process was modeled on a real MMC with its three main phases, namely the matrix, the particles, and the particle-matrix interface. As a result, the developed FE model was successful in offering an accurate description of MMC behavior during cutting as well as the interactions between the particles, the matrix, and the cutting tool.

The developed finite element was used in three different steps. In the first step, the model was utilized for investigating various scenarios of interactions between the cutting

tool and particulate reinforcements. These interactions can cause cutting force fluctuations, increased cutting tool wear rate, and lower machined surface quality. This investigation showed that initiation of particle fracture and debonding can lead to sudden drops in the cutting force. On the other hand, when the interaction between the tool and particle results in the particle squeeze, a rapid increase in the cutting force was observed.

Scenarios of tool-particle interactions for particles located on the cutting line, located above the cutting line, and located below the cutting line were investigated. For the particle located on the cutting line, the tool-particle interaction resulted in debonding and fracture of the particulate reinforcement, thus leaving cavities on the machined surface and consequently lowering the surface quality. When the particle was located above the cutting line, it was pushed against the matrix into the chip as a result of interaction with cutting tool.

For a particle located below the cutting line, the interaction with the tool caused particle fracture, though larger pieces of the particle remained attached to the matrix and, thus, the machined surface roughness was not increased significantly. This analysis also proved that large plastic deformations in the matrix around the particles can cause debonding of the particles from the matrix.

In the second step, the finite element model was utilized for investigating the effect of cutting speed on MMC machining. This model offered an accurate prediction of cutting forces for machining MMCs with different cutting speeds.

The developed model also provided valuable knowledge regarding the effect of cutting speed on tool-particle interactions. For a particle located on the cutting line, it was shown that particle debonding is accelerated with an increase in cutting speed. This is while fracture of particles occurs when machining using lower cutting speeds. For a particle located below the cutting line, particle fracture occurred at all cutting speeds. In this case, lower cutting speed resulted in more rapid debonding of particle pieces from the matrix while at higher speeds, particle pieces remained attached and pushed into the matrix. For a particle located above the cutting line, increase in cutting speed altered the nature of crack initiation during tool-particle interaction. For lower cutting speeds of  $v=30$  m/min and  $v=60$  m/min, cracks started ahead of the cutting tool at the particle-matrix interface and then progressed into the matrix. This means that crack initiation occurred before a direct contact between the cutting tool and particle, which had an adverse effect on the machined surface quality. However, for higher cutting speed of  $v=100$  m/min, crack started at the contact region between the cutting tool and matrix.

In the last step of using the finite element model, the model was utilized for investigating the plastic deformations during MMC machining. This model used ALE adaptive meshing to overcome the issues related to mesh distortion during metal cutting. The model showed that, due to existence of reinforcements, non-uniform plastic strains are observed in the chip during MMC machining. The FE simulation depicted zones of high deformation along the particles and zones of low deformation between the particles. Local areas of very high deformation were also observed adjacent to particles, which resulted in high stress concentration in the particles.

Analysis of plastic deformations beneath the machined surface showed high plastic deformation around the particles located on the cutting line. For particles located above the cutting line, plastic deformation beneath the surface was very low. For particles located below the cutting line, interaction with the tool did not affect the plastic deformation beneath the surface, i.e. plastic strains were similar to the areas where there were no tool-particle interactions.

An analytical model for prediction of MMC cutting forces was developed based on energy partition of the cutting system and relied on conventional constitutive equations, i.e. equations that were developed for monolithic materials. The developed model was successful in providing an accurate prediction of cutting force during MMC machining for various feed rates and cutting speeds. However, model's predictions were not as accurate for machining MMCs with different particle sizes. This was attributed to the model's reliance on conventional constitutive equations. Since these constitutive equations were proposed for capturing the behavior of traditional monolithic materials, their description of MMC behavior is not accurate.

In order to overcome the issues related to the conventional constitutive equations, a novel constitutive equation for description of MMC behavior was also proposed. This developed constitutive equation explicitly described the effect of MMC's unique features, namely particle size and volume fraction, on MMC behavior during cutting. In this equation, MMC's parameters were directly included and, unlike the conventional constitutive equations, they were not embedded in model constants.

The developed constitutive equation was utilized in an analytical model for prediction of cutting force. Accuracy of model predictions proved that the developed constitutive equation is capable of capturing the MMC behavior during machining. Using one set of constants for each matrix material, the developed model provided accurate prediction of cutting force for machining MMCs with different volume fractions and particle sizes with various feed rates and cutting speeds. This accomplishment is considered to be a major breakthrough in modeling MMC machining process.

The proposed model was used for studying the effect of various parameters on MMC cutting force. Increase in particle size was shown to result in an increase in cutting force. This was attributed to the effect of larger particles on increasing the power required for debonding and fracture of particles. This investigation also proved that an increase in particle volume fraction can initially lead to larger cutting forces, which is due to the larger power required for debonding and fracture of particles. However, as the volume fraction is further increased and the distance between particles becomes too small, large stress concentrations occur between the particles and matrix cracking becomes easier. This will consequently lower the required cutting force.

The numerical and analytical models developed in this thesis were successful in offering a detailed and accurate description of MMC behavior during the metal cutting process as well as explaining the unique characteristics of MMC machining, including the interactions between the cutting tool and various MMC phases. This achievement is the main contribution of this research.

## 8.2 Future work

Future research related to machining metal matrix composites can focus on the recommendations described in this section.

1. A more complex finite element modeling of MMC machining process can be developed. This model can incorporate the effect of cutting edge radius. A three-dimensional FE model may be developed for studying the oblique cutting process for MMCs. More complex material models for various MMC phases can be incorporated in the FE simulation to provide a more accurate description of MMC behavior during metal cutting.
2. Finite element modeling can be performed on whisker-reinforced and fiber-reinforced MMCs. A more comprehensive FE model can include various shapes for the reinforcements in the MMC. Random positions can be selected for the reinforcements in the model based on microstructural analysis of actual MMCs.
3. Improvement of the analytical models requires additional experiments with different types of matrix and reinforcement materials. More comprehensive models can be developed by utilizing more complex equations for describing the behavior of the matrix, the reinforcements, and the matrix-reinforcement interface phases of the MMC.

# References

- [1] Kannan, S. and H. Kishawy, *Tribological aspects of machining aluminium metal matrix composites*. Journal of Materials Processing Technology, 2008. **198**(1): p. 399-406.
- [2] Trent, E.M. and P.K. Wright, *Metal Cutting*. 2000, Woburn, MA, USA: Butterworth-Heinemann.
- [3] Dandekar, C.R. and Y.C. Shin, *Modeling of machining of composite materials: A review*. International Journal of Machine Tools and Manufacture, 2012. **57**: p. 102-121.
- [4] Tomac, N., K. Tannessen, and F.O. Rasch, *Machinability of Particulate Aluminium Matrix Composites*. CIRP Annals - Manufacturing Technology, 1992. **41**(1): p. 55-58.
- [5] Quigley, O., J. Monaghan, and P. O'Reilly, *Factors affecting the machinability of an Al/SiC metal-matrix composite*. Journal of Materials Processing Technology, 1994. **43**(1): p. 21-36.
- [6] Lin, J.T., D. Bhattacharyya, and C. Lane, *Machinability of a silicon carbide reinforced aluminium metal matrix composite*. Wear, 1995. **181–183**: p. 883-888.
- [7] El-Gallab, M. and M. Sklad, *Machining of Al/SiC particulate metal-matrix composites: Part I: Tool performance*. Journal of Materials Processing Technology, 1998. **83**(1–3): p. 151-158.
- [8] El-Gallab, M. and M. Sklad, *Machining of Al/SiC particulate metal matrix composites: Part II: Workpiece surface integrity*. Journal of Materials Processing Technology, 1998. **83**(1–3): p. 277-285.

- [9] Kannan, S. and H.A. Kishawy, *Surface characteristics of machined aluminium metal matrix composites*. International Journal of Machine Tools and Manufacture, 2006. **46**(15): p. 2017-2025.
- [10] Kishawy, H.A., S. Kannan, and M. Balazinski, *An energy based analytical force model for orthogonal cutting of metal matrix composites*. CIRP Annals - Manufacturing Technology, 2004. **53**(1): p. 91-94.
- [11] Pramanik, A., L.C. Zhang, and J.A. Arsecularatne, *Prediction of cutting forces in machining of metal matrix composites*. International Journal of Machine Tools and Manufacture, 2006. **46**(14): p. 1795-1803.
- [12] Sikder, S. and H.A. Kishawy, *Analytical model for force prediction when machining metal matrix composite*. International Journal of Mechanical Sciences, 2012. **59**(1): p. 95-103.
- [13] Chawla, N. and K.K. Chawla, *Metal matrix composites*. 2006, New York: Springer. xi, 401 p.
- [14] Varadarajan, Y.S., L. Vijayaraghavan, and R. Krishnamurthy, *The machinability characteristics of aluminosilicate fiber reinforced Al alloy composite*. Materials and Manufacturing Processes, 2002. **17**(6): p. 811-824.
- [15] Weinert, K. and M. Lange. *Machining of fibre reinforced magnesium*. in *Materials Science Forum*. 2003. Trans Tech Publ.
- [16] Dandekar, C.R. and Y.C. Shin, *Laser-assisted machining of a fiber reinforced metal matrix composite*. Journal of Manufacturing Science and Engineering, Transactions of the ASME, 2010. **132**(6).
- [17] El-Gallab, M. and M. Sklad, *Machining of Al/SiC particulate metal matrix composites part III: comprehensive tool wear models*. Journal of Materials Processing Technology, 2000. **101**(1-3): p. 10-20.
- [18] El-Gallab, M.S. and M.P. Sklad, *Machining of aluminum/silicon carbide particulate metal matrix composites: Part IV. Residual stresses in the machined workpiece*. Journal of Materials Processing Technology, 2004. **152**(1): p. 23-34.

- [19] Yanming, Q. and Z. Zehua, *Tool wear and its mechanism for cutting SiC particle-reinforced aluminium matrix composites*. Journal of Materials Processing Technology, 2000. **100**(1–3): p. 194-199.
- [20] Andrewes, C.J.E., H.-Y. Feng, and W.M. Lau, *Machining of an aluminum/SiC composite using diamond inserts*. Journal of Materials Processing Technology, 2000. **102**(1–3): p. 25-29.
- [21] Davim, J.P., *Diamond tool performance in machining metal–matrix composites*. Journal of Materials Processing Technology, 2002. **128**(1–3): p. 100-105.
- [22] Davim, J.P., *Design of optimisation of cutting parameters for turning metal matrix composites based on the orthogonal arrays*. Journal of Materials Processing Technology, 2003. **132**(1–3): p. 340-344.
- [23] Ding, X., W.Y.H. Liew, and X.D. Liu, *Evaluation of machining performance of MMC with PCBN and PCD tools*. Wear, 2005. **259**(7–12): p. 1225-1234.
- [24] Muthukrishnan, N., M. Murugan, and K. Prahlada Rao, *Machinability issues in turning of Al-SiC (10p) metal matrix composites*. The International Journal of Advanced Manufacturing Technology, 2008. **39**(3-4): p. 211-218.
- [25] Kannan, S., H.A. Kishawy, I.M. Deiab, and M.K. Surappa. *Modeling of tool flank wear progression during orthogonal machining of metal matrix composites*. in *Transactions of the North American Manufacturing Research Institute of SME*. 2005.
- [26] Kishawy, H.A., S. Kannan, and M. Balazinski, *Analytical Modeling of Tool Wear Progression During Turning Particulate Reinforced Metal Matrix Composites*. CIRP Annals - Manufacturing Technology, 2005. **54**(1): p. 55-58.
- [27] Kannan, S., H.A. Kishawy, and M. Balazinski, *Flank Wear Progression During Machining Metal Matrix Composites*. Journal of Manufacturing Science and Engineering, 2006. **128**(3): p. 787-791.
- [28] Mackerle, J., *Finite-element analysis and simulation of machining: a bibliography (1976–1996)*. Journal of Materials Processing Technology, 1998. **86**(1–3): p. 17-44.

- [29] Mackerle, J., *Finite element analysis and simulation of machining: an addendum: A bibliography (1996–2002)*. International Journal of Machine Tools and Manufacture, 2003. **43**(1): p. 103-114.
- [30] Iwata, K., K. Osakada, and Y. Terasaka, *Process modeling of orthogonal cutting by the rigid-plastic finite element method*. Journal of Engineering Materials and Technology, Transactions of the ASME, 1984. **106**(2): p. 132-138.
- [31] Tay, A.O., M.G. Stevenson, and G. de Vahl Davis, *Using the finite element method to determine temperature distributions in orthogonal machining*. Inst Mech Eng (Lond) Proc, 1974. **188**(55): p. 627-638.
- [32] Stevenson, M.G., P.K. Wright, and J.G. Chow, *Further developments in applying the finite element method to the calculation of temperature distributions in machining and comparisons with experiment*. Journal of engineering for industry, 1983. **104**(3): p. 149-154.
- [33] Lajczok, M., *A study of some aspects of metal machining using the finite-element method*, 1981: North Carolina State University. p. 242.
- [34] Ceretti, E., P. Fallböhmer, W.T. Wu, and T. Altan, *Application of 2D FEM to chip formation in orthogonal cutting*. Journal of Materials Processing Technology, 1996. **59**(1-2 SPEC. ISS.): p. 169-180.
- [35] Marusich, T.D. and M. Ortiz, *Modelling and simulation of high-speed machining*. International Journal for Numerical Methods in Engineering, 1995. **38**(21): p. 3675-3694.
- [36] Carroll Iii, J.T. and J.S. Strenkowski, *Finite element models of orthogonal cutting with application to single point diamond turning*. International Journal of Mechanical Sciences, 1988. **30**(12): p. 899-920.
- [37] Strenkowski, J.S. and K.-J. Moon, *Finite Element Prediction of Chip Geometry and Tool/Workpiece Temperature Distributions in Orthogonal Metal Cutting*. Journal of Manufacturing Science and Engineering, 1990. **112**(4): p. 313-318.
- [38] Strenkowski, J.S. and J. Carroll III. *An orthogonal metal cutting model based on an eulerian finite element method*. in *Manufacturing Processes, Machines and Systems, Proceedings of the 13th NSF Conference on Production Research and Technology*. 1986.

- [39] Wing Kam, L., C. Herman, C. Jiun-Shyan, and B. Ted, *Arbitrary lagrangian-eulerian petrov-galerkin finite elements for nonlinear continua*. Computer Methods in Applied Mechanics and Engineering, 1988. **68**(3): p. 259-310.
- [40] Rakotomalala, R., P. Joyot, and M. Touratier, *Arbitrary Lagrangian-Eulerian thermomechanical finite-element model of material cutting*. Communications in Numerical Methods in Engineering, 1993. **9**(12): p. 975-987.
- [41] Gadala, M.S. and J. Wang, *ALE formulation and its application in solid mechanics*. Computer Methods in Applied Mechanics and Engineering, 1998. **167**(1-2): p. 33-55.
- [42] Movahhedy, M., M.S. Gadala, and Y. Altintas, *Simulation of the orthogonal metal cutting process using an arbitrary Lagrangian-Eulerian finite-element method*. Journal of Materials Processing Technology, 2000. **103**(2): p. 267-275.
- [43] Movahhedy, M.R., M.S. Gadala, and Y. Altintas, *Simulation of chip formation in orthogonal metal cutting process: an ALE finite element approach*. Machining Science and Technology, 2000. **4**(1): p. 15-42.
- [44] Arola, D., M.B. Sultan, and M. Ramulu, *Finite Element Modeling of Edge Trimming Fiber Reinforced Plastics*. Journal of Manufacturing Science and Engineering, 2002. **124**(1): p. 32-41.
- [45] Nayak, D., I. Singh, N. Bhatnagar, P. Mahajan, S. Ghosh, J.C. Castro, and J.K. Lee, *An Analysis of Machining Induced Damages in FRP Composites — A Micromechanics Finite Element Approach*. AIP Conference Proceedings, 2004. **712**(1): p. 327-331.
- [46] Nayak, D., N. Bhatnagar, and P. Mahajan, *Machining Studies of Uni-Directional Glass Fiber Reinforced Plastic (UD-GFRP) Composites Part 1: Effect of Geometrical and Process Parameters*. Machining Science and Technology, 2005. **9**(4): p. 481-501.
- [47] Nayak, D., N. Bhatnagar, and P. Mahajan, *Machining Studies of UD-FRP Composites Part 2: Finite Element Analysis*. Machining Science and Technology, 2005. **9**(4): p. 503-528.
- [48] Venu Gopala Rao, G., P. Mahajan, and N. Bhatnagar, *Machining of UD-GFRP composites chip formation mechanism*. Composites Science and Technology, 2007. **67**(11-12): p. 2271-2281.

- [49] Dandekar, C.R. and Y.C. Shin, *Multiphase Finite Element Modeling of Machining Unidirectional Composites: Prediction of Debonding and Fiber Damage*. Journal of Manufacturing Science and Engineering, 2008. **130**(5): p. 051016-12.
- [50] Mkaddem, A., I. Demirci, and M.E. Mansori, *A micro–macro combined approach using FEM for modelling of machining of FRP composites: Cutting forces analysis*. Composites Science and Technology, 2008. **68**(15–16): p. 3123-3127.
- [51] Monaghan, J. and D. Brazil, *Modelling the flow processes of a particle reinforced metal matrix composite during machining*. Composites Part A: Applied Science and Manufacturing, 1998. **29**(1-2): p. 87-98.
- [52] Monaghan, J. and D. Brazil, *Modeling the sub-surface damage associated with the machining of a particle reinforced MMC*. Computational Materials Science, 1997. **9**(1-2): p. 99-107.
- [53] Zhu, Y. and H.A. Kishawy, *Influence of alumina particles on the mechanics of machining metal matrix composites*. International Journal of Machine Tools and Manufacture, 2005. **45**(4–5): p. 389-398.
- [54] Pramanik, A., L.C. Zhang, and J.A. Arsecularatne, *An FEM investigation into the behavior of metal matrix composites: Tool-particle interaction during orthogonal cutting*. International Journal of Machine Tools and Manufacture, 2007. **47**(10): p. 1497-1506.
- [55] Zhou, L., S.T. Huang, D. Wang, and X.L. Yu, *Finite element and experimental studies of the cutting process of SiCp/Al composites with PCD tools*. The International Journal of Advanced Manufacturing Technology, 2011. **52**(5-8): p. 619-626.
- [56] Dandekar, C.R. and Y.C. Shin, *Multi-step 3-D finite element modeling of subsurface damage in machining particulate reinforced metal matrix composites*. Composites Part A: Applied Science and Manufacturing, 2009. **40**(8): p. 1231-1239.
- [57] Ernst, H. and M.E. Merchant, *Chip formation, friction and high quality machined surfaces*. Surface Treatment of Metals, 1941. **29**: p. 299-378.
- [58] Merchant, M.E., *Basic mechanics of the metal cutting process*. Journal of Applied Mechanics, 1944. **11**(A): p. 168-175.

- [59] Merchant, M.E., *Mechanics of the metal cutting process. I. Orthogonal cutting and a type 2 chip*. Journal of Applied Physics, 1945. **16**(5): p. 267-275.
- [60] Merchant, M.E., *Mechanics of the metal cutting process. II. Plasticity conditions in orthogonal cutting*. Journal of Applied Physics, 1945. **16**(6): p. 318-324.
- [61] Astakhov, V.P., *Tribology of metal cutting*. 2006, London: Elsevier.
- [62] Altintas, Y., *Manufacturing Automation: Metal Cutting Mechanics, Machine Tool Vibrations, and CNC Design*. 2012: Cambridge University Press.
- [63] Lee, E. and B. Shaffer, *Theory of plasticity applied to the problem of machining*. Journal of Applied Mechanics, 1951. **18**: p. 405-413.
- [64] Kobayashi, S. and E.G. Thomsen, *The Role of Friction in Metal Cutting*. Journal of Manufacturing Science and Engineering, 1960. **82**(4): p. 324-332.
- [65] Oxley, P.L.B., *A strain-hardening solution for the "shear angle" in orthogonal metal cutting*. International Journal of Mechanical Sciences, 1961. **3**(1-2): p. 68-79.
- [66] Oxley, P.L.B. and W.F. Hastings, *Predicting the strain rate in the zone of intense shear in which the chip is formed in machining from the dynamic flow stress properties of the work material and the cutting conditions*. Proceedings of the Royal Society of London. A. Mathematical and Physical Sciences, 1977. **356**(1686): p. 395.
- [67] Oxley, P.L.B., *The mechanics of machining: an analytical approach to assessing machinability*. 1989, New York: E. Horwood.
- [68] Oxley, P.L.B., *Development and application of a predictive machining theory*. Machining Science and Technology, 1998. **2**(2): p. 165-189.
- [69] Arsecularatne, J.A., P. Mathew, and P.L.B. Oxley, *Prediction of chip flow direction and cutting forces in oblique machining with nose radius tools*. Proceedings of the Institution of Mechanical Engineers, Part B: Journal of Engineering Manufacture, 1995. **209**(B4): p. 305-315.
- [70] Arsecularatne, J.A., R.F. Fowle, P. Mathew, and P.L.B. Oxley, *Prediction of cutting forces and built-up edge formation conditions in machining with oblique nose radius tools*. Proceedings

- of the Institution of Mechanical Engineers, Part B: Journal of Engineering Manufacture, 1996. **210**(5): p. 457-469.
- [71] Arsecularatne, J.A., R.F. Fowle, and P. Mathew, *Prediction of Chip Flow Direction, Cutting Forces and Surface Roughness in Finish Turning*. Journal of Manufacturing Science and Engineering, 1998. **120**(1): p. 1-12.
- [72] Astakhov, V.P., *On the inadequacy of the single-shear plane model of chip formation*. International Journal of Mechanical Sciences, 2005. **47**(11): p. 1649-1672.
- [73] Colwell, L., *Predicting the angle of chip flow for single-point cutting tools*. Transactions of the ASME, 1954. **76**: p. 199-204.
- [74] Astakhov, V.P. and X. Xiao, *A methodology for practical cutting force evaluation based on the energy spent in the cutting system*. Machining Science and Technology, 2008. **12**(3): p. 325-347.
- [75] Kishawy, H.A., A. Hosseini, B. Moetakef-Imani, and V.P. Astakhov, *An energy based analysis of broaching operation: Cutting forces and resultant surface integrity*. CIRP Annals - Manufacturing Technology, 2012. **61**(1): p. 107-110.
- [76] Waldorf, D.J., R.E. Devor, and S.G. Kapoor, *A slip-line field for ploughing during orthogonal cutting*. Journal of Manufacturing Science and Engineering, Transactions of the ASME, 1998. **120**(4): p. 693-699.
- [77] Waldorf, D.J., R.E. DeVor, and S.G. Kapoor, *An evaluation of ploughing models for orthogonal machining*. Journal of Manufacturing Science and Engineering, Transactions of the ASME, 1999. **121**(4): p. 550-558.
- [78] Waldorf, D.J. *A simplified model for ploughing forces in turning*. in *Transactions of the North American Manufacturing Research Institute of SME*. 2004.
- [79] Waldorf, D.J., *A simplified model for ploughing forces in turning*. Journal of Manufacturing Processes, 2006. **8**(2): p. 76-82.

- [80] Johnson, G.R. and W.H. Cook. *A constitutive model and data for metals subjected to large strains, high strain rates and high temperatures*. in *International Ballistics Committee*. 1983. The Hague, Netherlands.
- [81] Dabade, U.A., D. Dapkekar, and S.S. Joshi, *Modeling of chip–tool interface friction to predict cutting forces in machining of Al/SiCp composites*. *International Journal of Machine Tools and Manufacture*, 2009. **49**(9): p. 690-700.
- [82] Pramanik, A., L.C. Zhang, and J.A. Arsecularatne, *Machining of metal matrix composites: Effect of ceramic particles on residual stress, surface roughness and chip formation*. *International Journal of Machine Tools and Manufacture*, 2008. **48**(15): p. 1613-1625.
- [83] Maekawa, K., T. Shirakashi, and E. Usui, *Flow stress of low carbon steel at high temperature and strain rate (part 2) - flow stress under variable temperature and variable strain rate*. *Bulletin of the Japan Society of Precision Engineering*, 1983. **17**(3): p. 167-172.
- [84] Shirakashi, T., K. Maekawa, and E. Usui, *Flow stress of low carbon steel at high temperature and strain rate (part 1) - propriety of incremental strain method in impact compression test with rapid heating and cooling systems*. *Bulletin of the Japan Society of Precision Engineering*, 1983. **17**(3): p. 161-166.
- [85] Bammann, D., M. Chiesa, and G. Johnson, *Modeling large deformation and failure in manufacturing processes*. *Theoretical and Applied Mechanics*, 1996: p. 359-376.
- [86] Nemat-Nasser, S. and J.B. Isaacs, *Direct measurement of isothermal flow stress of metals at elevated temperatures and high strain rates with application to Ta and TaW alloys*. *Acta Materialia*, 1997. **45**(3): p. 907-919.
- [87] Guo, Y.B., Q. Wen, and K.A. Woodbury, *Dynamic Material Behavior Modeling Using Internal State Variable Plasticity and Its Application in Hard Machining Simulations*. *Journal of Manufacturing Science and Engineering*, 2005. **128**(3): p. 749-759.
- [88] Johnson, G.R. *Materials characterization for computations involving severe dynamic loading*. in *Proc. Army Symp. on Solid Mechanics*. 1980. DTIC Document.

- [89] Johnson, G.R. and W.H. Cook, *Fracture characteristics of three metals subjected to various strains, strain rates, temperatures and pressures*. Engineering Fracture Mechanics, 1985. **21**(1): p. 31-48.
- [90] Sima, M. and T. Özel, *Modified material constitutive models for serrated chip formation simulations and experimental validation in machining of titanium alloy Ti-6Al-4V*. International Journal of Machine Tools and Manufacture, 2010. **50**(11): p. 943-960.
- [91] Andrade, U., M.A. Meyers, K.S. Vecchio, and A.H. Chokshi, *Dynamic recrystallization in high-strain, high-strain-rate plastic deformation of copper*. Acta Metallurgica et Materialia, 1994. **42**(9): p. 3183-3195.
- [92] Calamaz, M., D. Coupard, and F. Girod, *A new material model for 2D numerical simulation of serrated chip formation when machining titanium alloy Ti-6Al-4V*. International Journal of Machine Tools and Manufacture, 2008. **48**(3-4): p. 275-288.
- [93] Finot, M., Y.L. Shen, A. Needleman, and S. Suresh, *Micromechanical modeling of reinforcement fracture in particle-reinforced metal-matrix composites*. Metallurgical and Materials Transactions A, 1994. **25**(11): p. 2403-2420.
- [94] Finot, M., Y.L. Shen, S. Suresh, R. Jacquand, and A. Needleman. *Micromechanical modeling of damage in particle-reinforced composites*. in *American Society of Mechanical Engineers, Applied Mechanics Division, AMD*. 1994.
- [95] Kiser, M.T., F.W. Zok, and D.S. Wilkinson, *Plastic flow and fracture of a particulate metal matrix composite*. Acta Materialia, 1996. **44**(9): p. 3465-3476.
- [96] Ghosh, S. and S. Moorthy, *Particle fracture simulation in non-uniform microstructures of metal-matrix composites*. Acta Materialia, 1998. **46**(3): p. 965-982.
- [97] Eckschlager, A., W. Han, and H.J. Böhm, *A unit cell model for brittle fracture of particles embedded in a ductile matrix*. Computational Materials Science, 2002. **25**(1-2): p. 85-91.
- [98] Böhm, H.J., A. Eckschlager, and W. Han, *Multi-inclusion unit cell models for metal matrix composites with randomly oriented discontinuous reinforcements*. Computational Materials Science, 2002. **25**(1-2): p. 42-53.

- [99] Böhm, H.J., W. Han, and A. Eckschlager, *Multi-inclusion unit cell studies of reinforcement stresses and particle failure in discontinuously reinforced ductile matrix composites*. CMES - Computer Modeling in Engineering and Sciences, 2004. **5**(1): p. 5-20.
- [100] Bruzzi, M.S., P.E. McHugh, F. O'Rourke, and T. Linder, *Micromechanical modelling of the static and cyclic loading of an Al 2124-SiC MMC*. International Journal of Plasticity, 2001. **17**(4): p. 565-599.
- [101] Bruzzi, M.S. and P.E. McHugh, *Micromechanical investigation of the fatigue crack growth behaviour of Al-SiC MMCs*. International Journal of Fatigue, 2004. **26**(8): p. 795-804.
- [102] Bruzzi, M.S. and P.E. McHugh, *Micromechanical modeling of the static loading of an Al 359-SiC MMC*. Journal of Engineering Materials and Technology, Transactions of the ASME, 2005. **127**(1): p. 106-118.
- [103] Babout, L., Y. Brechet, E. Maire, and R. Fougères, *On the competition between particle fracture and particle decohesion in metal matrix composites*. Acta Materialia, 2004. **52**(15): p. 4517-4525.
- [104] Hauert, A., A. Rossoll, and A. Mortensen, *Particle fracture in high-volume-fraction ceramic-reinforced metals: Governing parameters and implications for composite failure*. Journal of the Mechanics and Physics of Solids, 2009. **57**(11): p. 1781-1800.
- [105] Griffith, A.A., *The Phenomena of Rupture and Flow in Solids*. Philosophical Transactions of the Royal Society of London. Series A, Containing Papers of a Mathematical or Physical Character, 1921. **221**: p. 163-198.
- [106] Gurland, J. and J. Plateau, *The mechanism of ductile rupture of metals containing inclusions*, 1963, Brown Univ., Providence. p. 27.
- [107] Tanaka, K., T. Mori, and T. Nakamura, *Cavity formation at the interface of a spherical inclusion in a plastically deformed matrix*. Philosophical Magazine, 1970. **21**(170): p. 267-279.
- [108] Argon, A.S., J. Im, and R. Safoglu, *Cavity formation from inclusions in ductile fracture*. Metallurgical Transactions A, 1975. **6**(4): p. 825-837.

- [109] Nicholson, D.W., *On the detachment of a rigid inclusion from an elastic matrix*. Journal of Adhesion, 1979. **10**(3): p. 255-260.
- [110] Needleman, A., *A Continuum Model for Void Nucleation by Inclusion Debonding*. Journal of Applied Mechanics, 1987. **54**(3): p. 525-531.
- [111] Tvergaard, V., *Fibre debonding and breakage in a whisker-reinforced metal*. Materials Science and Engineering: A, 1995. **190**(1–2): p. 215-222.
- [112] Tvergaard, V., *Debonding of short fibres among particulates in a metal matrix composite*. International Journal of Solids and Structures, 2003. **40**(25): p. 6957-6967.
- [113] Foulk, J.W., D.H. Allen, and K.L.E. Helms, *A model for predicting the damage and environmental degradation dependent life of SCS-6/Timetal®21S [0]4 metal matrix composite*. Mechanics of Materials, 1998. **29**(1): p. 53-68.
- [114] Foulk, J.W., D.H. Allen, and K.L.E. Helms, *Formulation of a three-dimensional cohesive zone model for application to a finite element algorithm*. Computer Methods in Applied Mechanics and Engineering, 2000. **183**(1–2): p. 51-66.
- [115] Özel, T., *The influence of friction models on finite element simulations of machining*. International Journal of Machine Tools and Manufacture, 2006. **46**(5): p. 518-530.
- [116] *Abaqus 6.14 Documentation*. 2014: SIMULIA.
- [117] Lesuer, D.R., G.J. Kay, and M.M. LeBlanc. *Modeling large-strain, high-rate deformation in metals*. in *Third Biennial Tri-Laboratory Engineering Conference on Modeling and Simulation*. 1999. Pleasanton, CA, United States of America.
- [118] Munro, R.G., *Evaluated material properties for a sintered  $\alpha$ -alumina*. Journal of the American Ceramic Society, 1997. **80**(8): p. 1919-1928.
- [119] Shaw, M.C., *Metal cutting principles*. 2nd ed. Oxford series on advanced manufacturing. 2005, New York: Oxford University Press. xix, 651 p.
- [120] Özel, T. and E. Zeren, *Determination of work material flow stress and friction for FEA of machining using orthogonal cutting tests*. Journal of Materials Processing Technology, 2004. **153–154**(0): p. 1019-1025.

- [121] Astakhov, V.P. and S. Shvets, *The assessment of plastic deformation in metal cutting*. Journal of Materials Processing Technology, 2004. **146**(2): p. 193-202.
- [122] Jiang, J., F. Sheng, and F. Ren, *Modelling of two-body abrasive wear under multiple contact conditions*. Wear, 1998. **217**(1): p. 35-45.
- [123] Goddard, J. and H. Wilman, *A theory of friction and wear during the abrasion of metals*. Wear, 1962. **5**(2): p. 114-135.
- [124] Sin, H., N. Saka, and N.P. Suh, *Abrasive wear mechanisms and the grit size effect*. Wear, 1979. **55**(1): p. 163-190.
- [125] Weibull, W., *A statistical distribution function of wide applicability*. Journal of applied mechanics, 1951. **18**(3): p. 293-297.
- [126] Shackelford, J.F. and W. Alexander, *CRC Materials Science and Engineering Handbook, Third Edition*. 2000: Taylor & Francis.
- [127] Holt, J.M., C. Gibson, and C.Y. Ho, *Structural alloys handbook*. 1999, West Lafayette: CINDAS/Purdue University.
- [128] Fang, N., *A New Quantitative Sensitivity Analysis of the Flow Stress of 18 Engineering Materials in Machining*. Journal of Engineering Materials and Technology, 2005. **127**(2): p. 192-196.
- [129] Li, Y. and K.T. Ramesh, *Influence of particle volume fraction, shape, and aspect ratio on the behavior of particle-reinforced metal–matrix composites at high rates of strain*. Acta Materialia, 1998. **46**(16): p. 5633-5646.
- [130] Christman, T., A. Needleman, S. Nutt, and S. Suresh, *On microstructural evolution and micromechanical modelling of deformation of a whisker-reinforced metal-matrix composite*. Materials Science and Engineering: A, 1989. **107**(0): p. 49-61.
- [131] Nutt, S.R. and A. Needleman, *Void nucleation at fiber ends in Al-SiC composites*. Scripta Metallurgica, 1987. **21**(5): p. 705-710.
- [132] Tvergaard, V., *Effect of fibre debonding in a whisker-reinforced metal*. Materials Science and Engineering: A, 1990. **125**(2): p. 203-213.

- [133] Tay, A.O., M.G. Stevenson, G. de Vahl Davis, and P.L.B. Oxley, *A numerical method for calculating temperature distributions in machining, from force and shear angle measurements*. International Journal of Machine Tool Design and Research, 1976. **16**(4): p. 335-349.
- [134] Wallin, K., T. Saario, and K. Törrönen, *Fracture of brittle particles in a ductile matrix*. International Journal of Fracture, 1986. **32**(3): p. 201-209.